

Initial-state showering based on colour dipoles connected to incoming parton lines

Jan-Christopher Winter *

Fermi National Accelerator Laboratory, Batavia, IL, USA

Frank Krauss †

Institute for Particle Physics Phenomenology, Durham University, UK

November 1, 2018

Abstract

A parton-shower model for hadronic collisions based on the emission properties of QCD dipoles is proposed. This proposal therefore extends the well-known radiation pattern of pure final-state colour dipoles to QCD initial-state radiation, both of which are treated perturbatively. Corresponding dipole splitting functions are derived and the kinematics of all dipole splittings is discussed. Application to hadron production in electron-positron annihilation, to Drell-Yan lepton-pair and QCD jet production yields encouraging results.

*jwinter@fnal.gov

†frank.krauss@durham.ac.uk

Contents

1	Introduction	3
2	The Colour Dipole Model	5
2.1	Physical background of the CDM	5
2.2	Initial-state radiation in the original CDM	7
3	New approach to initial-state radiation using colour dipoles	8
3.1	Kinematic framework	9
3.2	Towards generalized evolution variables	11
3.3	Dipole splitting cross sections and functions for QCD radiation	12
4	Final-state colour dipoles	15
4.1	Final–final dipole single-emission phase space and kinematics	15
4.2	Splitting functions for final-state QCD radiation	17
5	Initial-state colour dipoles	19
5.1	Single-emission kinematics	19
5.1.1	Gluon emission phase space of initial–initial dipoles	20
5.1.2	Quark emission phase space of initial–initial dipoles	21
5.1.3	Construction of the splitting kinematics	22
5.2	Initial–initial dipole splitting functions	24
6	Dipoles from final–initial colour flows	26
6.1	Single-emission kinematics	26
6.1.1	Gluon emission phase space of final–initial dipoles	27
6.1.2	Antiquark emission phase space of final–initial dipoles	28
6.1.3	Construction of the emission momenta	29
6.2	Final–initial dipole splitting functions	30
7	The complete shower algorithm	31
7.1	The Sudakov form factor	32
7.2	Generation of the emission’s Sudakov variables	33
7.3	Scale choices, starting conditions and iteration principles	34
8	First results	35
8.1	Hadron production in electron–positron collisions	36
8.2	Inclusive production of Drell–Yan lepton pairs at hadron colliders	39
8.3	Inclusive jet production at hadron colliders	46
9	Conclusions	52
	Acknowledgements	53

1 Introduction

In the past decades, Monte Carlo event generators including QCD parton-shower routines, such as PYTHIA [1–5], HERWIG [6, 7], or ARIADNE [8] have been very successful in correctly describing, both qualitatively and quantitatively, a large range of QCD-related phenomena at different colliders, at different energies, and with different initial states. The success of these programs is based on good approximations in their treatment of logarithmically enhanced emission of QCD particles in soft and/or collinear regions of phase space.

In conventional parton showers such as the ones in PYTHIA [9–11] and HERWIG [12], this is achieved by an expansion around the collinear limit. This manifests itself in the ordering of subsequent emissions by virtual masses supplemented with an explicit veto on increasing emission angles or by an ordering by emission angles, respectively.¹ Alternatively, perturbative QCD cascades can be formulated in terms of splitting colour dipoles rather than partons. This has been realized in the shower algorithm in ARIADNE [8], which is based on the Colour Dipole Model (CDM) [15–17]. Splitting the dipoles and ordering the emissions in relative transverse momenta of subsequent splittings is equivalent to an expansion around the soft limits of the radiation process. In [15] it has been argued that such a dipole shower quite naturally fulfils the requirements of quantum coherence, which, for the parton showers, lead to angular ordering of subsequent emission, see e.g. [18]. It is interesting to note that the ARIADNE shower yields results, which show a similar or even better agreement with data from electron–positron annihilation into hadrons [19–23]. However, in the CDM initial-state radiation (ISR), i.e. parton emission off incoming partons, is not treated explicitly but taken into account by redefining ISR as final-state radiation (FSR) off hadron remnants [24]. To correctly model ISR in this picture, non-perturbative corrections have to be applied, cf. sec. 2. Equipped with such non-perturbative components in its modelling of initial-state associated radiation, ARIADNE also succeeded in describing a wealth of DIS data in a very reassuring way, see for instance [25]. To some extent, the reason for this excellent performance in describing e^+e^- and DIS data is not entirely understood. The cause could be better treatment of small- x effects in the DIS case, which are assumed to be an issue also for the forthcoming LHC. Equally well, it could be just the effect of a careful tuning of the additional non-perturbative parameters in the case of DIS. Another idea is related to a supposedly improved simulation of single, potentially non-global, potentially large logarithms stemming from soft corners of emission phase space. This appears as a consequence of the fact that the leading $1/N_C$ terms of such contributions are better accounted for if the description of the radiation is based on the dipole structure in both matrix element and phase space [26]. This blurred picture of, on the one hand, delivering overwhelming agreement with data of various measurements and, on the other hand, lacking clear determination of the reason for this success provides a fair, but not the only motivation for trying out an alternative path in modelling ISR arising from colour dipoles.

In view of the upcoming LHC era, Monte Carlo event generators are undergoing an intensive overhaul, leading essentially to complete rewrites of the codes [27–30] or to the construction of entirely new programs such as SHERPA [13] in the modern, object-oriented programming language C++. Apart from issues related to maintenance, a number of improvements concerning physics simulation motivated the construction of new event generators. First of all, the shower algorithms themselves, forming an essential part of the event generators, have been improved: in PYTHIA, a k_\perp ordered parton shower has been introduced [4, 31] in order to better account for coherence effects. There is also a dramatically extended model of multiple parton interactions.

¹ The current parton shower implementation of SHERPA [13], APACIC++ [14], is very similar to the well-established virtuality-ordered PYTHIA shower.

In HERWIG, a new formulation of angular ordering [32] better embeds Lorentz invariance and provides an improved treatment of those regions, where the original HERWIG shower over- or undercounted parton emissions. In addition, a new parton-shower formulation has been developed based on Catani–Seymour dipole factorization [33–36], and steps have been undertaken in the development of yet another QCD shower formulation, which uses antenna functions [37]. For all these recent developments, a common denominator has been to put more emphasis on the notion of a colour-connected partner of the splitting parton and thus a reduction of the difference between parton and dipole showers. Especially, the showers based on either Catani–Seymour [38,39] or antenna subtraction kernels [40,41], aim at an improved matching with exact higher-order QCD matrix elements. In fact, considering the need for increased precision, this systematic inclusion of higher orders in the perturbative expansion of QCD has been a dramatic and recent improvement of the paradigm underlying building and using multipurpose Monte Carlo event generators.

In the matching approach, the exact next-to-leading order matrix-element result is consistently combined with the resummation of the parton shower [42–45] such that the overall result correctly reproduces the corresponding NLO total cross section and the first additional hard QCD emission. This has been first implemented for specific processes in MC@NLO [46] on the basis of the Frixione–Kunszt–Signer subtraction [47]. This method depends to some extent on the details of the parton shower and also has some residual dependence on the process in question. With the POWHEG-approach a shower-independent matching solution [44, 45] extends the original MC@NLO proposal and the appearance of negative weights, which are present in the former method, can be circumvented.

In alternative approaches, sequences of tree-level multileg matrix elements with increasing final-state multiplicity are merged with the parton shower to yield fully inclusive samples correct at leading logarithmic accuracy by avoiding double-counting and missing phase-space regions. A first approach, known as the CKKW merging approach, has been presented for the case of electron–positron annihilations into jets in [48]; later it has been extended to hadronic collisions [49] and it has been reformulated to a merging procedure – called LCKKW – in conjunction with a dipole shower [50]. A further method, the MLM method, has been developed also aiming at a merging of matrix elements and parton showers. It uses a different way in generating the inclusive samples based on a geometric interpretation of the full radiation pattern in terms of cone jets [51, 52]. These different algorithms have been implemented in different variations on different levels of sophistication in conjunction with various matrix-element generators or already in full-fledged event generators, see e.g. [13, 53–62]. Despite their differences they exhibit an assuring level of agreement [63].

In all these new approaches, parton emissions from matrix elements at a given perturbative order have to be balanced with corresponding emissions from a shower algorithm. Intuitively one may anticipate that dipole-like kinematics, leaving all particles of the splitting on their mass shells, may facilitate simpler procedures for this balancing. Furthermore, concerning matching, the CDM seems to be the more natural partner to the matrix-element part of calculations based on a subtraction method using antenna factorization [40].

In this publication, therefore, an extension of the “perturbative” dipole shower [16] as implemented in ARIADNE [8] to truly perturbative initial-state radiation is proposed, in contrast to the original ISR Lund CDM. Hence, the goal is to formulate the QCD evolution of a hard process initiated through a hadronic collision entirely perturbatively as a sequence of colour-dipole emissions. In particular, emissions associated to the initial state are treated as to directly emerge from colour dipoles spanned by the external parton lines. The beam remnants are kept completely outside the perturbative evolution, their connection to the evolved cascade is left to the

hadronization to deal with. As a direct consequence, three types of dipoles and, hence, of associated radiation contribute to the full development of the final cascade, namely emissions from initial–initial (II), final–initial (FI), and final–final (FF) dipoles. Consequently, the emissions are denoted as initial–initial, final–initial- and final-state radiation (ISR, FISR, FSR), respectively. In order to model ISR and FISR in the fully perturbative version of the CDM proposed here, a backward evolution of the initial-state related radiation pattern of the shower is mandatory and automatically necessitates the inclusion of parton distribution functions (PDFs).

The outline of the paper is as follows: in sec. 2 the basics of the dipole-shower model as implemented in ARIADNE will briefly be introduced. In addition, the treatment of ISR through final-state dipole splittings involving the beam remnants will be discussed. In the next section, sec. 3, the basic ideas of the newly proposed dipole shower are highlighted, especially its different ansatz for ISR simulation. This includes the generalization of the kinematical framework and of the evolution variables. In the following three sections, the kinematics and single-emission cross sections of all dipole splittings in various configurations of initial- and final-state partons will be detailed, recapitulating the case of dipoles consisting of final-state partons, the case implemented in ARIADNE, in sec. 4. The kinematics and splitting functions of the new dipole types present in this model are discussed in secs. 5 and 6. The complete shower algorithm will be presented in sec. 7 and its performance for various physics processes will be highlighted in sec. 8.

2 The Colour Dipole Model

2.1 Physical background of the CDM

The Lund colour dipole model (CDM) has strong connections to the semiclassical method of virtual quanta [64–66], which equates the electromagnetic energy flux associated with the fields emitted by fast moving charges with an energy flux of equivalent photons. Owing to the large Lorentz boosts of the charged emitter, the corresponding electric and magnetic fields are orthogonal to each other and they populate a plane orthogonal to the direction of motion of the emitter only. This amounts to a pulse of electromagnetic energy, given by

$$dI(\omega, b) \simeq \hbar \alpha d\omega \frac{2\pi b db}{\pi^2}, \quad (1)$$

where b denotes the impact parameter, i.e. the distance w.r.t. the emitter; ω is the frequency of the field component. It is bound from above by $\omega < p/mb$, where p and m are the momentum and mass of the emitter, respectively. Equating this energy pulse I with a number of equivalent quanta n ,

$$dI = \hbar \omega d\omega, \quad (2)$$

and replacing the impact parameter with transverse momentum yields

$$dn \simeq \frac{\alpha}{\pi} \frac{dk_{\perp}^2}{k_{\perp}^2} \frac{d\omega}{\omega}. \quad (3)$$

A similar result emerges when considering bremsstrahlung off a charged particle, changing its otherwise straight direction of motion through a sudden “kick”, or connected with the pair production of charged particles. Then, in the Breit-frame of the former process, or in the centre-of-mass frame of the latter, a rapidity y can be defined w.r.t. the axis of motion of the

charged particle(s). A short calculation based on a full quantum-mechanical treatment shows that, neglecting spin effects, the number of bremsstrahlung-photons is well approximated by

$$dn = \frac{2\alpha}{\pi} \frac{d\omega}{\omega} dy, \quad (4)$$

cf. [67]. Here, the rapidity must satisfy

$$|y| < |y_0|, \quad (5)$$

and y_0 is the rapidity of the emitter(s). Rewriting energy through transverse momentum,

$$k_{\perp} = \frac{\omega}{\cosh y}, \quad (6)$$

then leads to

$$dn = \frac{\alpha}{\pi} \frac{dk_{\perp}^2}{k_{\perp}^2} dy. \quad (7)$$

Because of its equivalence to eq. (4), this equation exhibits the dominance of soft radiation in the semi-classical limit. In this context it is worth to note that the same limit is used in eikonal-type factorization of matrix elements employed, e.g. , in antenna subtraction methods [40,68] for the calculation of perturbative higher-order corrections to scattering cross sections in QCD.

The simple formula for the semi-classical limit of photon radiation off a charged dipole, eq. (7), can be refined through a full quantum-mechanical treatment, including spin effects, see also later sections. However, the dominant features of the radiation pattern are already fixed by the simple formula, which in turn denotes the starting point for a shower simulation based on individual dipole emissions. The differential probability for such an emission to occur in an interval dp_{\perp}^2 and dy is related to $d\mathcal{P} = d\sigma/d\sigma_0$ given by

$$d\mathcal{P} \simeq \frac{\alpha_s}{\pi} \frac{dp_{\perp}^2}{p_{\perp}^2} dy. \quad (8)$$

Here p_{\perp} denotes a transverse momentum, which in the CDM is constructed out of Lorentz invariant quantities. Numbering the momenta of the particles after emission such that the newly emitted particle is labelled with “2”, and, denoting the momenta before and after the emission with \tilde{p}_i and p_i , respectively, the emission can be symbolized as

$$\tilde{p}_1 + \tilde{p}_3 = p_1 + p_2 + p_3. \quad (9)$$

The squared invariant masses of sets of momenta are denoted as

$$s_{ij\dots} = (p_i + p_j + \dots)^2 \quad \text{and} \quad \tilde{s}_{ij\dots} = (\tilde{p}_i + \tilde{p}_j + \dots)^2. \quad (10)$$

A Lorentz invariant transverse momentum can be defined as

$$p_{\perp}^2 = \frac{s_{12} s_{23}}{s_{123}} = \frac{s_{12} s_{23}}{\tilde{s}_{13}}, \quad (11)$$

in agreement with [16,67] and the ARIADNE implementation. Moreover, a rapidity can then be computed through

$$y = \frac{1}{2} \ln \frac{s_{12}}{s_{23}}. \quad (12)$$

The Lorentz invariant choice guarantees a frame-independent description of the dipole splitting process. Using p_\perp as the ordering parameter for subsequent emissions, a Sudakov form factor encodes the non-emission probability between two scales $p_{\perp,\text{high}}^2$ and $p_{\perp,\text{low}}^2$ in analogy to conventional parton showers:

$$\Delta(p_{\perp,\text{high}}^2, p_{\perp,\text{low}}^2) = \exp \left\{ - \int_{p_{\perp,\text{low}}^2}^{p_{\perp,\text{high}}^2} dp_\perp^2 \int_{y_-(p_\perp)}^{y_+(p_\perp)} dy \frac{d\mathcal{P}}{dp_\perp^2 dy} \right\}. \quad (13)$$

In this form, the leading logarithms are resummed to all orders.

The Sudakov form factor constitutes the basis of the simulation of parton emission also in the framework of the CDM. In contrast to ordinary parton showers, however, here the relevant objects are colour dipoles, which emerge naturally when considering the large N_C limit. In this limit, colour charges in the fundamental representation (quarks and antiquarks) have one colour partner, and colour charges in the adjoint representation (gluons) have two colour partners. The dipoles are built from pairs of such colour partners, and the emission of a gluon off a dipole effectively amounts to splitting the dipole into two.

This self-similar process of dipole splitting, which is described in a probabilistic fashion, is easily encoded as a Markovian process in form of a computer program. Adding in the leading logarithmic behaviour and colour coherence as a dominant feature of QCD emissions results in a strict ordering of subsequent emissions such that the actual p_\perp of a dipole splitting sets the maximal p_\perp for the splittings of the two resulting dipoles.

2.2 Initial-state radiation in the original CDM

In ARIADNE, the only complete CDM implementation so far, initial-state radiation off incoming partons is not explicitly taken into account. Instead, ISR is *redefined* as FSR, where dipoles are spanned between potential final-state partons and the outgoing hadron remnants [24, 69–71]. Considering DIS of leptons on hadrons, it can be argued that, as the hadron is in a bound state, all radiation originates from the colour dipole between the struck point-like quark and the hadron remnant – being an extended object composed of individual valence quarks and sea partons. Thus, an extended “antenna” is formed and from the electro-magnetic (semi-classical) analogy it follows that radiation of wavelengths smaller than the extension of the antenna is suppressed. Therefore, the original CDM was modified such that only a p_\perp -dependent fraction $a(p_\perp)$ of the remnant enters the splitting process [24]:

$$a(p_\perp) = \left(\frac{\mu}{p_\perp} \right)^\alpha, \quad (14)$$

where μ parametrizes the inverse size of the remnant and α refers to the dimensionality of the emitter, both being parameters to be tuned to data. In e^+e^- annihilation the (“triangle”) phase-space boundaries are approximated by $|y| < \ln(M/p_\perp)$, which now are supplemented by the extra condition $y < \ln(M\mu/p_\perp^2)$. This obviously limits the range of accessible p_\perp values in the splitting of the dipole of mass M . The strategy of sharing the recoil in such cases was inspired by the Lund string model, where an extra kink on the string (hadron) is interpreted as an extra gluon. This led to the introduction of recoil gluons to compensate for the recoil momentum associated with the part of the hadron, which participates in the emission.² Moreover, in cases where a sea quark is hit, the picture experiences further minor modifications. Taken together,

²For the ARIADNE rewrite in C++, the possibility of discarding recoil gluons completely is under consideration.

a good fraction of phenomenological, non-perturbative modelling enters the Lund CDM for ISR through all these assumptions.

Next, consider Drell–Yan-like processes; there, a quark–antiquark pair annihilates to produce a lepton pair. In conventional parton showers, the two incoming quarks would emit secondary partons, typically simulated in a backward evolution algorithm [9, 12]. The recoil of these emissions is transferred to colour partners and the final-state leptons. In contrast, in ARIADNE the incoming quarks do not radiate but rather the two beam remnants, which are the only two coloured final-state objects before radiation (cf. left panel in fig. 1). Then, the recoil of the first emission is compensated for by the final-state leptons [55, 71], for all further dipole emissions, additional recoil gluons are added, if the emission occurred in phase space significantly away from the vector boson [71]. A further obvious refinement is the correction of the first emission to the corresponding matrix-element expression. The sharp phase-space cut-off is then replaced by a softer suppression function, in order to describe the high transverse-momentum spectrum of the vector boson.

3 New approach to initial-state radiation using colour dipoles

The principles underlying the proposal of this paper for the construction of a purely perturbative colour-dipole model are:

- the maintenance of the probabilistic interpretation of emissions as encoded in the Sudakov form factor, which will be obtained from exponentiating single-emission differential cross sections;
- the large N_C limit of the radiation pattern, and the restriction to account for the leading terms only, i.e. the leading dipoles, of this expansion;
- the generalization of the kinematics and the evolution variables used in the original CDM and in ARIADNE to the case of ISR and FISR;
- the factorization of the emission phase space and matrix elements around the soft limit (the radiation pattern has to be factorized in terms of $2 \rightarrow 3$ splittings, to be derived for II and FI dipoles);
- the utilization of crossing symmetries for the determination of dipole splitting functions;
- the construction of on-shell kinematics for each splitting on an emission-by-emission basis, allowing stop and restart the cascading after any individual emission;
- the backward evolution description of radiation related to incoming partons, and, consequently, the emergence of PDFs in the shower algorithm in a way similar to conventional parton showers.

A number of issues are not at all covered here, which are, however, straightforward to include in some future work, namely

- the comparison of different forms of splitting cross sections;
- the approach’s extension to account for finite, non-zero quark masses (here, all partons are treated as massless);
- an extension to Supersymmetry;

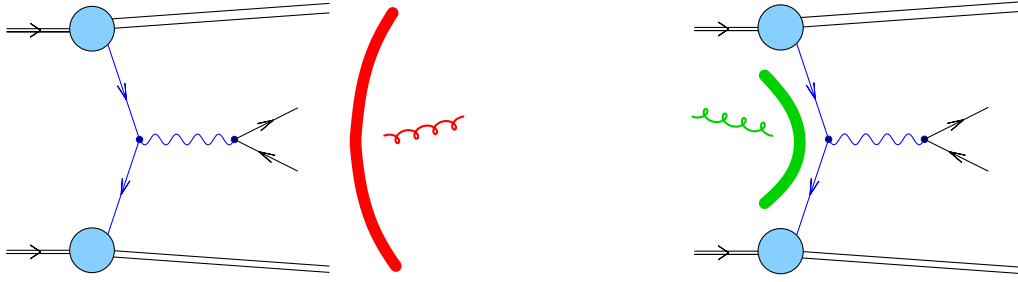


Figure 1: The Lund CDM approach to initial-state radiation in Drell–Yan processes (left panel) vs. the direct, perturbative approach as suggested by the new dipole-shower model (right panel). The treatment in modelling a first gluon emission is illustrated.

- the QED radiation off the dipoles.

To exemplify the impact of the principle outlined above, consider Drell–Yan processes; in contrast to the Lund approach, see sec. 2.2, in the new dipole picture the primary dipole $\bar{q}_i q'_i$ is directly formed by the two incoming quarks, and the emission will be calculated from the competition between gluon (see fig. 1), quark and antiquark bremsstrahlung. The real-emission matrix-element information will directly enter, through the corresponding dipole splitting functions, as in the FF counterpart of emitting a first gluon off the $q\bar{q}'$ dipole. The boson’s transverse momentum will be naturally generated, because the new initial-state momenta will be oriented along the beam direction. In case of an actual gluon emission, a system of two colour-connected successor FI dipoles emerges, namely a $\bar{q}_i g_f$ and a $g_f q'_i$ dipole. A further gluon radiated into the final state will then create a first FF dipole. If a quark is produced first, an FI dipole $q_f g_i$ and a successor II dipole $g_i q'_i$ will be generated with again a dual rôle played by the gluon, here g_i . Hence, the QCD evolution of the leading-order Drell–Yan pair production process eventually will involve all possible dipole types.

3.1 Kinematic framework

The occurrence of new dipoles and corresponding splittings is an immediate consequence of the suggested new CDM approach. A list summarizing the principal dipoles of QCD is shown in tab. 1. Dipoles are labelled by $\tilde{k}\tilde{\ell}$, thus, in the most general way a splitting triggered by the emission of a (new) gluon g is expressed as

$$\tilde{k}\tilde{\ell} \rightarrow k g \ell. \quad (15)$$

The notation is chosen such that the flavour and colour flow of all particles is outgoing. Three types of gluon emission emerge, related by crossing symmetry; any such splitting will leave the number of initial-state partons constant:

$$\tilde{k}\tilde{\ell} \rightarrow \begin{cases} \tilde{k} g_f \tilde{\ell} & : \text{ gluon emission,} \\ q g_i \tilde{\ell} & : \text{ quark emission, provided that } \tilde{k} = \bar{q}_i, \\ \tilde{k} g_i \bar{q} & : \text{ antiquark emission, provided that } \tilde{\ell} = q_i. \end{cases} \quad (16)$$

Here, the subscripts indicate whether the gluon emerges in the initial or final state. In the former case, this requires to replace the initial (anti)quark of the original dipole by the initial gluon and emit the corresponding antiquark (quark) in the final state.

QCD dipoles, $\tilde{k} \tilde{\ell}$		
II dipoles, $\bar{v}' i$	FI dipoles, $f i$	FF dipoles, $f \bar{f}'$
$\bar{q}'_i q_i$	$q_f q'_i$	$q_f \bar{q}'_f$
$g_i q_i$	$q_f g_i$	$q_f g_f$
$g_i g_i$	$g_f g_i$	$g_f g_f$

Table 1: All dipole types appearing in QCD (the supplemental indices i or f label whether the parton is in the initial or final state, respectively; if clear from the context, the index f will be left out). The primes indicate that different quark flavours may constitute the dipole.

Having clarified the notations used for the dipoles and their splittings, the kinematic objects will be introduced. First of all, the momenta are defined as incoming/outgoing if they are associated with the physical initial/final state. Those before and after the emission are denoted by $\tilde{p}_{\tilde{m}}$ and p_m , respectively, such that, expressed through the momenta alone the dipole splitting process can be written as

$$\tilde{\zeta}_{\tilde{k}} \tilde{p}_{\tilde{k}} + \tilde{\zeta}_{\tilde{\ell}} \tilde{p}_{\tilde{\ell}} \longrightarrow \varsigma_k p_k + \varsigma_g p_g + \varsigma_{\ell} p_{\ell}. \quad (17)$$

Here and in the following the signature factors $\tilde{\zeta}_{\tilde{m}} = \pm 1$ and $\varsigma_m = \pm 1$ for partons in the final (+) and initial (−) state. The before- and after-emission total momenta \tilde{p}_0 and p_0 then read

$$-\varsigma_0 \tilde{p}_0 = \tilde{\zeta}_{\tilde{k}} \tilde{p}_{\tilde{k}} + \tilde{\zeta}_{\tilde{\ell}} \tilde{p}_{\tilde{\ell}}, \quad (18)$$

$$-\varsigma_0 p_0 = \varsigma_k p_k + \varsigma_g p_g + \varsigma_{\ell} p_{\ell}, \quad (19)$$

with the requirement that $\tilde{p}_0^2 = p_0^2$. Furthermore $\tilde{\zeta}_0 \equiv \varsigma_0$, and the signature factor ς_0 , i.e. the association of the total momenta with the initial or final state is chosen such that the after-emission configuration refers to a production ($\varsigma_0 = -1$, FF dipoles), scattering ($\varsigma_0 = -1$, FI dipoles), or annihilation ($\varsigma_0 = 1$, II dipoles) process. Consequently, the four-vector \tilde{p}_0 then corresponds to the four-momentum of the decaying parent dipole having mass $|M|$ such that

$$\tilde{p}_0^2 = M^2 \equiv -Q^2 = p_0^2, \quad (20)$$

with Q^2 arranged to be positive definite for FI dipole emissions. Accordingly, Lorentz-invariant energy fractions w.r.t. p_0 are defined through³

$$x_m = \frac{2 p_m p_0}{p_0^2}. \quad (21)$$

The squared invariant masses of two- and three-parton systems are denoted by

$$s_{mn} = (\varsigma_m p_m + \varsigma_n p_n)^2 \quad \text{and} \quad s_{mnr} = (\varsigma_m p_m + \varsigma_n p_n + \varsigma_r p_r)^2 \quad (22)$$

where the inclusion of p_0 and the expressions related to the momenta before the emission are understood. Concerning all gluon emissions considered here, the identity

$$M^2 = s_{kg} + s_{gl} + s_{k\ell} = s_{kg\ell} = -Q^2, \quad (23)$$

holds true in general, since all partons are consistently treated as massless.

³The notion “energy fraction” is clear in the centre-of-mass frame of a parent FF dipole, where $x_m = 2E_m/M$.

3.2 Towards generalized evolution variables

Next, the dipole evolution variables have to be generalized such that all emissions of all dipole types can be treated on equal footing and embedded in a consistent CDM-like evolution. The generalized variables should have the property of leaving the well-established FSR treatment unchanged and they should satisfy the constraint that all splitting cross sections, i.e. those involving initial-state partons as well, will follow the approximate form given in eq. (8). This would just manifest the universal features of QCD radiation in the soft limit, reproduced by eikonal distributions factorizing off the squared matrix elements in emissions off initial and final states alike,

$$-\frac{1}{2} \left(\frac{p_k}{p_k p_g} - \frac{p_\ell}{p_g p_\ell} \right)^2 = \frac{2 s_{k\ell}}{s_{kg} s_{g\ell}}. \quad (24)$$

Note that the right-hand side of this equation explicitly assumes massless partons. Following eq. (11), the factor $2/p_\perp^2$ becomes identical to the eikonal factor in the soft limit, and the collinear limits manifest themselves in the two-parton squared masses appearing in this p_\perp^2 definition. Then, the generalized kinematic variables should exhibit the same singular behaviour in the soft/collinear limits for all dipole types, reflecting the crossing symmetry. Therefore, in this paper a generalized transverse momentum and rapidity are proposed in the form

$$p_\perp^2 = \left| \frac{s_{kg} s_{g\ell}}{s_{kg\ell}} \right|, \quad (25)$$

and

$$y = \frac{1}{2} \ln \left| \frac{s_{g\ell}}{s_{kg}} \right|. \quad (26)$$

Here, the invariant masses $s_{mn(r)}$ are calculated including the signature factors $\varsigma_{m,n,r}$, i.e. through eqs. (22). Clearly, for FF dipole cascading, all invariant masses are positive and hence the original CDM evolution variables of eqs. (11) and (12) are trivially recovered. For the other cases, the generalized form suggested here is a minimal Lorentz-invariant extension, guaranteeing a frame-independent evolution of the colour dipole. Moreover, these shower variables allow a global simultaneous ordering of all emissions. Given these generalized definitions, the identities

$$|s_{kg}| = |M| p_\perp e^{-y} \quad \text{and} \quad |s_{g\ell}| = |M| p_\perp e^{+y} \quad (27)$$

are found, indeed showing the similarity to the original Lund CDM.

So, having introduced the kinematic framework, in the following sections, secs. 4, 5 and 6, the derivation of the splitting kinematics for each dipole type (FF, II, and FI/IF) will be always pursued in four steps:

- First, the evolution variables p_\perp and y are identified.
- Then, the limits of the emission phase space are deduced, which for the rapidity typically read $y_- \leq y \leq y_+$. They guarantee that the evolution takes place within the physical region of phase space. These limitations are imposed through constraints on the evolution variables and, thus, determine the Sudakov form factor, see eq. (13) and sec. 7.
- Together with the strict limits, approximate ones are stated, denoted e.g. for the rapidity by $Y_- \leq y \leq Y_+$, which allow an analytical evaluation of approximate Sudakov form factors. They are used in a Monte Carlo procedure, which finally corrects for the true form of the exact Sudakov form factors by means of a veto algorithm, see e.g. [3].

- The on-shell three-parton kinematics of the splittings characterized by the central variables p_\perp and y are constructed from the original two-parton configurations. Remaining degrees of freedom are fixed with a few additional assumptions, i.e. through four-momentum conservation and a splitting-specific recoil strategy. The Lorentz invariant definition of the evolution variables guarantees the frame-independence of the actual construction.

3.3 Dipole splitting cross sections and functions for QCD radiation

In order to construct a parton shower as a Markovian process, the emission of any additional parton has to be factorized from the radiation of partons produced so far, such that the full radiation pattern can be built as a sequence of individual, mostly independent emissions. For the actual construction of a dipole shower, the individual parton emission should be modelled as being coherently shared between the two partons forming the dipole. The asymptotic form of these $2 \rightarrow 3$ dipole splitting cross sections has been presented in sec. 2, cf. eq. (8), which constitutes the limiting case of soft emissions. In order to extrapolate to harder regions of emission phase space and to include spin effects, the differential cross section for a $\tilde{k}\tilde{\ell}$ dipole developing into a $kg\ell$ colour-connected state is more conveniently written as

$$d\mathcal{P}_{\tilde{k}\tilde{\ell} \rightarrow kg\ell} \equiv \frac{d\sigma_{0 \rightarrow kg\ell}}{d\sigma_{0 \rightarrow \tilde{k}\tilde{\ell}}} = \frac{\alpha_s}{2\pi} D_{\tilde{k}\tilde{\ell} \rightarrow kg\ell}(p_\perp, y) \frac{dp_\perp^2}{p_\perp^2} dy. \quad (28)$$

This defines the *dipole splitting function* $D_{\tilde{k}\tilde{\ell} \rightarrow kg\ell}$ in analogy to the splitting kernels employed in conventional parton showers. In both cases, the splitting kernels of dipole or parton showers incorporate refinements, which go beyond the corresponding eikonal or collinear approximation, respectively. Here, the $D_{\tilde{k}\tilde{\ell} \rightarrow kg\ell}$ may be deduced by analyzing differential cross sections for additional real emission of partons in comparison to the corresponding Born level processes. This then yields the single-dipole phase-space and matrix-element factorization, which has to work at least in the singular domains of the real-emission phase space. Accordingly, first-order real corrections are fully or partially encoded in the splitting kernels automatically.

For the timelike case, the reasoning outlined above is realized by starting from the three-body decay rate of an object with mass M ,

$$d\Gamma_{0 \rightarrow fg\bar{f}'} = \frac{(2\pi)^4}{2M} |\mathcal{M}_{0 \rightarrow fg\bar{f}'}|^2 d\Phi_{0 \rightarrow fg\bar{f}'}(p_0; p_f, p_g, p_{\bar{f}'}), \quad (29)$$

where, in the massless limit, the dipole phase space and matrix element factorize according to

$$d\Phi_{0 \rightarrow fg\bar{f}'}(p_0; p_f, p_g, p_{\bar{f}'}) = d\Phi_{0 \rightarrow f\bar{f}'}(\tilde{p}_0 = p_0; \tilde{p}_f, \tilde{p}_{\bar{f}'}) \frac{ds_{fg} ds_{g\bar{f}'}}{16\pi^2 M^2} \frac{d\varphi}{2\pi} \quad (30)$$

and

$$|\mathcal{M}_{0 \rightarrow fg\bar{f}'}|^2 \simeq 8\pi\alpha_s C \hat{D}_{f\bar{f}' \rightarrow fg\bar{f}'} |\mathcal{M}_{0 \rightarrow f\bar{f}'}|^2, \quad (31)$$

respectively. Here, taking $N_C = 3$ for the number of colours, the colour factor labelled C has been introduced explicitly. It typically takes one of the following values, $C = C_F = \frac{N_C^2 - 1}{2N_C} = \frac{4}{3}$ for gluons emitted off quarks, $C = C_A = N_C = 3$ for gluons emitted off gluons, or $C = T_R = \frac{1}{2}$ for gluon splittings into quarks. \hat{D} denotes the dipole matrix element, which by definition correctly reproduces the singular terms of the parton emission process with potential differences in finite terms. Therefore, $d\Gamma_{0 \rightarrow fg\bar{f}'}$ can be expressed as

$$d\Gamma_{0 \rightarrow fg\bar{f}'} \simeq d\Gamma_{0 \rightarrow f\bar{f}'} \frac{C\alpha_s}{2\pi} \hat{D}_{f\bar{f}' \rightarrow fg\bar{f}'}(p_\perp, y, \varphi) dp_\perp^2 dy \frac{d\varphi}{2\pi} \quad (32)$$

with p_\perp and y taken from eqs. (25) and (26). In most cases, the dependence of \hat{D} on the azimuthal angle φ is neglected, thus, integrated out, such that the connection of the dipole splitting functions to the dipole matrix elements in the FF case reads

$$D_{f\bar{f}' \rightarrow fg\bar{f}'}(p_\perp, y) = \xi C p_\perp^2 \hat{D}_{f\bar{f}' \rightarrow fg\bar{f}'}(p_\perp, y). \quad (33)$$

Note that here a gluon-sharing factor ξ has been introduced because each gluon is contained by two dipoles.

For the class of II dipoles, i.e. those consisting of colour-connected incoming partons, the extraction of dipole splitting cross sections has to be accomplished on the level of hadronic cross sections to correctly account for PDF effects and possible phase-space (suppression) factors. In this case, a $2 \rightarrow 2$ scattering process rather than an $1 \rightarrow 3$ decay has to be considered. The differential cross section (using massless partons and having already integrated out the φ dependence) reads

$$d\sigma_{\bar{v}'i(gi) \rightarrow 0g(0q)} = f_{\bar{v}'(g)}(x_\pm, \mu_F) f_i(x_\mp, \mu_F) \frac{1}{S} \frac{|\mathcal{M}_{\bar{v}'i(gi) \rightarrow 0g(0q)}|^2}{16\pi\hat{s}^2} d\hat{s} d\hat{t} dy_{\text{cm}}, \quad (34)$$

where the usual $2 \rightarrow 2$ process Mandelstam variables, $\hat{s} = s_{\bar{v}'i(gi)}$ and $\hat{t} = s_{\bar{v}'g(qgi)}$ have been employed. Note that the quark emission case is signified by the parentheses. The $f_k(x_\pm, \mu_F)$ are the PDFs. At leading order they can be interpreted as the probability of resolving a parton k inside the nucleon with light-cone momentum fraction x taken w.r.t. the nucleon's momentum; μ_F names the factorization scale (defined in energy units), at which, pictorially speaking, the partonic substructure is probed. S and y_{cm} denote the centre-of-mass energy and rapidity of the collider system, respectively. The $2 \rightarrow 1$ hadronic differential Born cross section for creating a particle of mass M through the matrix element $\mathcal{M}_{\bar{v}'i(\bar{q}i) \rightarrow 0}$ characterizes the $\bar{v}'i$ dipole's situation before the emission. Then, similarly to the FF case, the $2 \rightarrow 2$ matrix element squared can be cast into a factorized form, reading

$$|\mathcal{M}_{\bar{v}'i(gi) \rightarrow 0g(0q)}|^2 \simeq 8\pi\alpha_s C \hat{D}_{\bar{v}'i(\bar{q}i) \rightarrow \bar{v}'gi(qgi)} |\mathcal{M}_{\bar{v}'i(\bar{q}i) \rightarrow 0}|^2. \quad (35)$$

This hence allows to write the $2 \rightarrow 2$ differential scattering cross section in terms of the $2 \rightarrow 1$ Born term $d\sigma_{\bar{v}'i(\bar{q}i) \rightarrow 0}$ where the tilde variables refer to the Born configuration:

$$\begin{aligned} d\sigma_{\bar{v}'i(gi) \rightarrow 0g(0q)} &\simeq d\sigma_{\bar{v}'i(\bar{q}i) \rightarrow 0} \left(\frac{dy_{\text{cm}}}{d\tilde{y}_{\text{cm}}} \right) \frac{f_{\bar{v}'(g)}(x_\pm, \mu_F) f_i(x_\mp, \mu_F)}{f_{\bar{v}'(\bar{q})}(\tilde{x}_\pm, \tilde{\mu}_F) f_i(\tilde{x}_\mp, \tilde{\mu}_F)} \frac{M^4}{\hat{s}^2(p_\perp, y)} \\ &\times \frac{C\alpha_s}{2\pi} \hat{D}_{\bar{v}'i(\bar{q}i) \rightarrow \bar{v}'gi(qgi)}(p_\perp, y) dp_\perp^2 dy. \end{aligned} \quad (36)$$

In contrast to the FF case, there is some additional freedom in arranging the actual recoils, since in principle the total energy of the splitting parton system will increase with each emission – additional momentum can be taken off the incoming nucleons. However, fixing the new centre-of-mass rapidity y_{cm} removes this ambiguity. The choice in this paper is to ensure constant rapidity derivatives, thus, set up a recoil handling, which eventually shifts the original \tilde{y}_{cm} through some function \hat{y} that exclusively depends on the variables associated to the emission,

$$y_{\text{cm}} = \tilde{y}_{\text{cm}} + \hat{y}(M^2, \hat{s}, \hat{t}). \quad (37)$$

Provided that these requirements can be satisfied, the II dipole splitting functions finally read

$$D_{\bar{v}'i(\bar{q}i) \rightarrow \bar{v}'gi(qgi)}(p_\perp, y) = \frac{f_{\bar{v}'(g)}(x_\pm, \mu_F) f_i(x_\mp, \mu_F)}{f_{\bar{v}'(\bar{q})}(\tilde{x}_\pm, \tilde{\mu}_F) f_i(\tilde{x}_\mp, \tilde{\mu}_F)} \frac{M^4 \xi C p_\perp^2}{\hat{s}^2(p_\perp, y)} \hat{D}_{\bar{v}'i(\bar{q}i) \rightarrow \bar{v}'gi(qgi)}(p_\perp, y) \quad (38)$$

and can be used to specify the associated differential splitting cross sections. In comparison to the gluon emission processes of FF dipoles, cf. eq. (33), additional terms arise in each of the II dipole functions, namely a PDF weight, \mathcal{W}_{PDF} , which contains a ratio of PDFs taken at the respective momentum fractions and factorization scales before and after the emission, and a phase-space weight, $\mathcal{W}_{\text{PSP}} = M^4/\hat{s}^2$, which accounts for the altered incoming flux of the parton-level differential cross section.

Similarly, the generic structure of final–initial dipole splitting cross sections $d\mathcal{P}_{fi(fq_i)\rightarrow fgi(fg_i\bar{q})}$ for gluon (antiquark) emissions into the final state is fixed through

$$D_{fi(fq_i)\rightarrow fgi(fg_i\bar{q})}(p_\perp, y) = \frac{f_{i(g)}(x_\pm, \mu_F)}{f_{i(q)}(\tilde{x}_\pm, \tilde{\mu}_F)} \frac{Q^4 \xi C p_\perp^2}{[\hat{s}(p_\perp, y) + Q^2]^2} \hat{D}_{fi(fq_i)\rightarrow fgi(fg_i\bar{q})}(p_\perp, y), \quad (39)$$

where the Mandelstam variable \hat{s} is related to the two-parton squared masses via $\hat{s} = s_{fg(f\bar{q})}$. Note that the right-hand side of eq. (39) exhibits, as for emissions off II dipoles, the additional PDF and phase-space weights. The formula has been derived along the lines already employed for the II case, again in the limit of zero quark masses. As before, by comparing the differential hadronic cross sections before and after the emission, the emission part can be factored out when relying on dipole matrix-element factorization,

$$|\mathcal{M}_{0i(0g)\rightarrow fg(f\bar{q})}|^2 \simeq 8\pi\alpha_s C \hat{D}_{fi(fq_i)\rightarrow fgi(fg_i\bar{q})} |\mathcal{M}_{0i(0q)\rightarrow f}|^2. \quad (40)$$

Like invariant squared amplitudes the dipole matrix elements \hat{D} obey crossing symmetry. Therefore, as an alternative to the direct calculation of II/FI dipole matrix elements, cf. eqs. (35) and (40), these \hat{D} expressions can be easily derived using crossing relations given that the FF dipole matrix elements have been worked out, see eq. (31). In cases where there are different particles in the final state, there is more than one possible crossing and, therefore, more than one corresponding dipole matrix element. The only remaining issues are the determination of the associated gluon-sharing and colour factors, ξ and C , respectively. The latter are assigned according to the generic, large N_C , colour structure of the emission.

Concerning dipole matrix-element factorization, there are two possible approaches to specify the dipole shower presented in this work. These approaches are:

- Extract the \hat{D} terms from the splitting cross sections employed in the Lund colour-dipole model [8, 15–17] for remnant-free dipole cascading. Results for II/FI dipoles are then derived from the corresponding FF dipole ones exploiting the crossing symmetry. In [16, 72] the Lund differential cross sections have been shown to obey the correct QCD behaviour in the soft and/or collinear (Altarelli–Parisi) limit.⁴ This reasoning therefore applies to the new cases as well.
- Use the tree-level antenna functions presented in [41]. Their crossing symmetry has been exploited already while considering antenna subtraction with hadronic initial states, see [73]. Thus, the utilization of antenna functions, instead of the Lund kinematic functions, has the clear advantage of constructing a dipole shower out of subtraction terms that form the basis of the antenna subtraction method [40, 41]; it therefore constitutes a very attractive alternative to the first approach.

In the subsequent sections of this publication the first approach is being followed in order to allow for direct comparison with ARIADNE in the FF case. All relevant gluon emission types of

⁴Strictly speaking, this matching in the singular domains of QCD has been demonstrated omitting the influence of colour factors, i.e. it has been actually shown for the FF dipole matrix elements \hat{D} .

$2 \rightarrow 3$ dipole splitting functions will be listed and their parton-radiation characteristics in the various cases will be discussed. Finally, the performance of the full model is tested focussing on comparisons with experimental data. It is worth stressing, however, that the implementation of the second approach is straightforward and will be subject of a forthcoming study.

4 Final-state colour dipoles

In this section emissions emerging from FF dipoles are discussed. This is the traditional case already present within the original version of the CDM, implemented in ARIADNE. The dipole splitting process can be specified by

$$f(\tilde{k}) \bar{f}'(\tilde{\ell}) \rightarrow f(k) g \bar{f}'(\ell). \quad (41)$$

4.1 Final-final dipole single-emission phase space and kinematics

Since the recoil of the emission will be completely shared between the three new partons, momentum conservation,

$$\tilde{p}_0 = \tilde{p}_f + \tilde{p}_{\bar{f}'} = p_f + p_g + p_{\bar{f}'} = p_0, \quad (42)$$

is realized between the momenta present before and after the emission. Note that apart from $\varsigma_0 = -1$, all other signature factors equal one. Neglecting parton masses, the relations

$$0 \leq s_{mn} = s_{0r} = M^2(1 - x_r) \leq M^2, \quad m \neq n \neq r \in \{f, g, \bar{f}'\}, \quad (43)$$

and the identity

$$M^2 = s_{fg} + s_{g\bar{f}'} + s_{f\bar{f}'}, \quad \text{also expressed by} \quad 2 = x_f + x_g + x_{\bar{f}'} \quad (44)$$

hold true. All energy fractions fall into the range $0 \leq x_r \leq 1$, and, hence, the physics constraints imposed on the kinematic invariants s_{mn} are satisfied. Following the steps outlined in sec. 3.2, the (p_\perp^2, y) phase-space parametrization can be characterized:

- The two Lorentz invariant dipole evolution variables are

$$p_\perp^2 = \frac{s_{fg} s_{g\bar{f}'}}{M^2} = M^2(1 - x_{\bar{f}'})(1 - x_f), \quad (45)$$

cf. eqs. (11) and (25), and the associated rapidity y ,

$$y = \frac{1}{2} \ln \frac{s_{g\bar{f}'}}{s_{fg}} = \frac{1}{2} \ln \frac{1 - x_f}{1 - x_{\bar{f}'}} \quad (46)$$

cf. eqs. (12) and (26). Therefore, the invariant masses can be re-expressed as,

$$\begin{aligned} s_{g\bar{f}'} &= Mp_\perp e^{+y}, \\ s_{fg} &= Mp_\perp e^{-y}, \\ s_{f\bar{f}'} &= M^2 - 2Mp_\perp \cosh y, \end{aligned} \quad (47)$$

cf. eqs. (27). As expected, the dominant phase-space regions are characterized by $p_\perp \rightarrow 0$, which points at p_\perp 's utilization as the ordering variable.

- The kinematic phase-space boundaries given through the relations in eqs. (43) determine the (maximal) integration limits $p_{\perp, \text{high}}^2$ and y_{\pm} stated in eq. (13). The determination of the precise boundaries is determined by the constraint

$$s_{fg} + s_{g\bar{f}'} = M^2 - s_{f\bar{f}'} \leq M^2, \quad (48)$$

leading to the following symmetric rapidity limits

$$|y| \leq \text{arccosh} \frac{M}{2p_{\perp}} = \ln \left(\frac{M}{2p_{\perp}} + \sqrt{\frac{M^2}{4p_{\perp}^2} - 1} \right). \quad (49)$$

The largest possible value for p_{\perp}^2 can also be read off these bounds,

$$p_{\perp, \text{max}}^2 = \frac{M^2}{4}. \quad (50)$$

- Simple rapidity bounds overestimating the more exact interval are obtained, for example, from $s_{fg}, s_{g\bar{f}'} \leq M^2$; this yields

$$Y_- = -\ln \frac{M}{p_{\perp}} \leq y \leq \ln \frac{M}{p_{\perp}} = Y_+, \quad (51)$$

which is nothing but the $(y, z = \ln \frac{p_{\perp}}{M})$ “triangle” commonly used to illustrate a dipole emission phase space. The effect of the sharper bounds now becomes apparent: they sizeably reduce the “triangle” area particularly in the central rapidity region, see fig. 2.

- Splitting kinematics: here the ideal frame to set up the new momenta is the centre-of-mass system of the parent FF dipole. Light-cone momenta⁵ w.r.t. the axis of the two original partons can conveniently be used. They yield

$$\begin{aligned} \tilde{p}_0 &= (M, M, \vec{0}) \quad \rightarrow \quad p_0 = (M, M, \vec{0}), \\ \tilde{p}_f &= (M, 0, \vec{0}) \quad \rightarrow \quad p_f = (f_{\perp} e^{y_f}, f_{\perp} e^{-y_f}, \vec{f}_{\perp}), \\ \tilde{p}_{\bar{f}'} &= (0, M, \vec{0}) \quad \rightarrow \quad p_{\bar{f}'} = (f'_{\perp} e^{y'_{f'}}, f'_{\perp} e^{-y'_{f'}}, \vec{f}'_{\perp}), \\ p_g &= p_0 - p_f - p_{\bar{f}'}. \end{aligned} \quad (52)$$

The $\vec{f}_{\perp}^{(')}$ and $y_f^{(')}$ are specified by the particular recoil strategies that are used for the different types of FF dipoles. The choices taken here closely follow the approach presented within the Lund CDM, see e.g. [8]. Thus, for gluon emissions off $q\bar{q}$ dipoles, the Kleiss trick [74] has been implemented to treat the recoils: the (anti)quark will retain its direction after the emission with a probability $x_{q(\bar{q})}^2 / (x_q^2 + x_{\bar{q}}^2)$. For qg dipoles, the recoil of the emitted gluon will be compensated by the quark only. Specifying the kinematics of these cases (assuming, for example to preserve the direction of the \vec{f}') leads to

$$f_{\perp} = \frac{x_f M}{2} \sin \vartheta, \quad \vec{f}_{\perp} = (f_{\perp} \cos \varphi, f_{\perp} \sin \varphi) \quad (53)$$

⁵ In this work, light-cone momenta are defined as follows: $q = (q_+, q_-, \vec{q}_{\perp})$ where $q_{\pm} = E_q \pm q_{\parallel}$; on-shell conditions can be intrinsically satisfied, if $q = (m_{\perp} e^z, m_{\perp} e^{-z}, \vec{q}_{\perp})$ is chosen, using $m_{\perp}^2 = q^2 + q_{\perp}^2$ and $z = \ln(q_+/q_-)/2$ such that $E_q = m_{\perp} \cosh z$ and $q_{\parallel} = m_{\perp} \sinh z$.

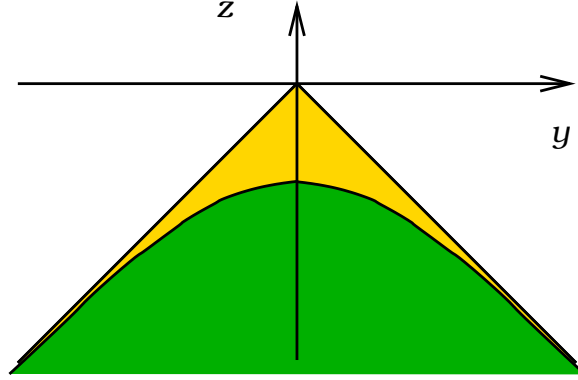


Figure 2: The phase space for gluon emission off FF dipoles; the dark-coloured region visualizes the available phase space. The bright colour is used to show the overestimation as given by the approximate limits w.r.t. the strict ones. Note that $z = \ln \frac{p_\perp}{M}$.

and

$$y_f = \frac{1}{2} \ln \frac{1 + \cos \vartheta}{1 - \cos \vartheta} = \ln \left(\cot \frac{\vartheta}{2} \right), \quad (54)$$

where the polar angle ϑ is given through $\cos \vartheta = (x_g^2 - x_f^2 - x_{\bar{f}'}^2) / (2 x_f x_{\bar{f}'})$ and the azimuthal angle φ is taken to be uniformly distributed between 0 and 2π . Moreover,

$$\vec{f}_\perp' \equiv \vec{0}, \quad y_f' \equiv \infty, \quad \text{preserving the product} \quad f_\perp' e^{y_f'} = x_{\bar{f}'} M. \quad (55)$$

For the distribution of recoils arising from gg dipole splittings, the simple specification will be corrected by rotating around the \hat{y} axis in a way that the $\sum p_T^2$ of the parent gluons will be minimized, however, small perturbations introduced by an additional rotation around the \hat{x} axis are allowed.

4.2 Splitting functions for final-state QCD radiation

In this section the refinements introduced by the Lund CDM [8, 15–17] to the simple eikonal splitting cross sections are briefly reviewed, in particular those for gluons arising from a $q_f \bar{q}_f$ dipole. Following the reasoning of sec. 3.3, the dipole splitting function for the $2 \rightarrow 3$ splitting $q\bar{q}' \rightarrow qg\bar{q}'$ is worked out from the comparison of the real-emission process $V \rightarrow q\bar{q}'g$ to the Born contribution for the vector boson decay $V \rightarrow q\bar{q}'$.⁶ For massless partons, the respective squared matrix elements averaged (summed) over colour and spin initial (final) states are

$$\begin{aligned} \overline{|\mathcal{M}_{\gamma^* \rightarrow q\bar{q}}|^2} &= 8 N_C e^2 e_q^2 \tilde{p}_q \tilde{p}_{\bar{q}} = 8 N_C e^2 e_q^2 \frac{M^2}{2}, \\ \overline{|\mathcal{M}_{\gamma^* \rightarrow q\bar{q}g}|^2} &= 8 \frac{N_C^2 - 1}{2} e^2 e_q^2 4\pi\alpha_s \frac{x_q^2 + x_{\bar{q}}^2}{(1 - x_q)(1 - x_{\bar{q}})}. \end{aligned} \quad (56)$$

⁶ The inclusion of various correlations depends on exactly which processes are selected. For example, also the correlation of the leptons, producing the vector boson V , with the quarks could be accounted for by taking the processes $\ell\bar{\ell}' \rightarrow q\bar{q}'(g)$ instead [74, 75].

The Lorentz invariant energy fractions of the emission are defined in eq. (21), and, for simplicity, $V = \gamma^*$ has been chosen, see e.g. [76]. Therefore,

$$\frac{d\Gamma_{\gamma^* \rightarrow qg\bar{q}}}{dx_q dx_{\bar{q}}} = d\Gamma_{\gamma^* \rightarrow q\bar{q}} \frac{C_F \alpha_s}{2\pi} \frac{x_q^2 + x_{\bar{q}}^2}{(1-x_q)(1-x_{\bar{q}})}, \quad (57)$$

where $C_F = (N_C^2 - 1)/(2N_C)$ is the colour factor of this emission. Obviously, in this case the matrix-element factorization is *exact* allowing to read off the corresponding differential dipole splitting cross section according to eq. (28),

$$\frac{d\mathcal{P}_{q\bar{q} \rightarrow qg\bar{q}}}{dp_{\perp}^2 dy} = \frac{C_F \alpha_s}{2\pi} \frac{(1 - \frac{p_{\perp}}{M} e^{+y})^2 + (1 - \frac{p_{\perp}}{M} e^{-y})^2}{p_{\perp}^2} = \frac{C_F \alpha_s}{2\pi} \frac{x_q^2(p_{\perp}, y) + x_{\bar{q}}^2(p_{\perp}, y)}{p_{\perp}^2}. \quad (58)$$

The obvious overestimation of the exact result,

$$\frac{d\mathcal{P}_{q\bar{q} \rightarrow qg\bar{q}}^{\text{approx}}}{dp_{\perp}^2 dy} = \frac{C_F \alpha_s}{2\pi} \frac{2}{p_{\perp}^2}, \quad (59)$$

in fact corresponds to a soft-gluon approximation neglecting quark spins, and allows for a direct implementation in a veto algorithm. Moreover, the dipole matrix element identified for the exact splitting can be cast into the following form:

$$\hat{D}_{q\bar{q} \rightarrow qg\bar{q}} = \frac{x_q^2 + x_{\bar{q}}^2}{p_{\perp}^2} = \frac{1}{s_{qg\bar{q}}} \left(\frac{s_{qg}}{s_{g\bar{q}}} + \frac{s_{g\bar{q}}}{s_{qg}} + \frac{2s_{q\bar{q}}s_{qg\bar{q}}}{s_{qg}s_{g\bar{q}}} \right), \quad (60)$$

where the rightmost expression exactly reproduces the three-parton tree-level antenna function $A_3^0(1_q, 3_g, 2_{\bar{q}})$ as stated in [41]. This case constitutes the easiest example for the compatibility of the two matrix-element factorization approaches.

Similar reasoning can be applied to yield the splitting functions for gluon emission off quark–gluon and gluon–gluon FF dipoles [72]. It should be stressed, however, that in these cases the dipole matrix-element factorization is correctly achieved only in the singular limits of the emission. Taken together, the dipole splitting functions for gluon emission off final-state dipoles in the Lund CDM [15–17] read

$$\begin{aligned} D_{f\bar{f}' \rightarrow fg\bar{f}'}(p_{\perp}, y) &= \xi_{\{F\}_A} C_{\{F\}_A} \left[x_f^{n_f}(p_{\perp}, y) + x_{\bar{f}'}^{n_{\bar{f}'}}(p_{\perp}, y) \right] \\ &\leq 2 \xi_{\{F\}_A} C_{\{F\}_A} \equiv D_{f\bar{f}' \rightarrow fg\bar{f}'}^{\text{approx}}(p_{\perp}, y). \end{aligned} \quad (61)$$

They are all implemented in ARIADNE and will be used in the model presented here as well. The invariant energy fractions are given by

$$x_{f,\bar{f}'} = 1 - \frac{p_{\perp}}{M} e^{\pm y}. \quad (62)$$

Here and in the following, the parton-dependent exponents are defined as $n_{q,g} = 2, 3$ and the curly-brackets notation is understood as $\left\{ \begin{array}{l} \dots \text{ for quark dipoles} \\ \dots \text{ else} \end{array} \right\}$. Note that $\xi_F = 1$; in the splitting functions for dipoles consisting of at least one gluon the factor of $\xi_A = \frac{1}{2}$ enters, since gluons are shared among two dipoles. The $D_{f\bar{f}' \rightarrow fg\bar{f}'}^{\text{approx}}$ not only give upper bounds to the exact splitting functions, they also imply eikonal approximations to the splitting cross sections of eq. (28).

A subtle issue in the formulation of a dipole shower is the assignment of colour factors. Obviously, for quark–quark and purely gluonic dipoles there are no problems, and, unambiguously, $C = C_F$

and $C = C_A$, respectively. For dipoles consisting of a(n) (anti)quark and a gluon, it is known that the colour factor cannot be pinpointed as straightforwardly as in the other cases, since e.g. for collinear radiation, the considered gluon emission can be traced back to either the (parent) quark or the (parent) gluon, such that in this limit the emission is therefore governed by C_F or C_A , respectively. Literally taken, these different colour-factor regimes have to be taken into account. This will lead to modifications of the corresponding dipole splitting functions and, possibly, to a decomposition (partitioning) of them into sub-contributions (subantennæ) addressing these different regimes unambiguously. However, in the large N_C limit, underlying the construction of shower codes, this issue triggers subleading effects only, since $2C_F, C_A \rightarrow N_C$ keeping in mind that the gluon-sharing factor is $\xi_A = \frac{1}{2}$.

5 Initial-state colour dipoles

The first case, which goes beyond the original CDM, is radiation off an initial-state dipole $\bar{v}i$ of mass M . Two generic splittings based on gluon emission are available, namely

$$\bar{v}'(\tilde{k}) i(\tilde{\ell}) \rightarrow \bar{v}'(k) g i(\ell) \quad \text{and} \quad \bar{q}_i(\tilde{k}) i(\tilde{\ell}) \rightarrow q(k) g_i i(\ell). \quad (63)$$

5.1 Single-emission kinematics

Restating eqs. (18) and (19) for the II dipole scenario, i.e. setting $\varsigma_0 = \varsigma_{g/q} = 1$ and all other signature factors equal to -1 , yields

$$\tilde{p}_{\bar{v}'/\bar{q}_i} + \tilde{p}_i = \tilde{p}_0 \quad \text{and} \quad p_{\bar{v}'/g_i} + p_i = p_0 + p_{g/q}, \quad \text{with} \quad p_0^2 = \tilde{p}_0^2 = M^2. \quad (64)$$

As already noted, the kinematics of the emission process here corresponds to that of a $2 \rightarrow 2$ scattering process rather than to that of a $1 \rightarrow 3$ decay. The recoil of the emitted parton $p_{g/q}$ cannot be absorbed by $p_{\bar{v}'/g_i}$ and p_i , since they are fixed to the beam axis. Thus, in contrast to the previously presented case, $\tilde{p}_0 \neq p_0$.⁷ For the scattering process, Mandelstam variables are defined as

$$\begin{aligned} \hat{s} &= (p_0 + p_{g/q})^2 = (p_{\bar{v}'/g_i} + p_i)^2 = M^2(1 + x_{g/q}) \geq M^2 \equiv \hat{s}_0, \\ \hat{t} &= (p_0 - p_i)^2 = (p_{\bar{v}'/g_i} - p_{g/q})^2 = M^2(1 - x_i) \leq 0, \\ \hat{u} &= (p_0 - p_{\bar{v}'/g_i})^2 = (p_i - p_{g/q})^2 = M^2(1 - x_{\bar{v}'/g_i}) \leq 0, \end{aligned} \quad (65)$$

where, again for massless partons, the bounds on \hat{s} , \hat{t} and \hat{u} together with their parametrizations in terms of energy fractions are simple, and, furthermore,

$$\hat{s} + \hat{t} + \hat{u} = M^2 \quad \text{as well as} \quad x_{\bar{v}'/g_i} + x_i = 2 + x_{g/q}. \quad (66)$$

As already indicated, the emission of a parton here requires an increase in \hat{s} w.r.t. \hat{s}_0 , related to an increase of the “Björken- x ”. This is in contrast to the FF case, where the system’s centre-of-mass energy remains constant. To deal with this issue, a generic parametrization is introduced, which relates the maximal partonic centre-of-mass squared energy to the squared mass of the parent dipole,

$$\hat{s}_{\max} = a M^2 \geq \hat{s}, \quad \text{such that} \quad 1 \leq \hat{s}/M^2 \leq a \leq S/M^2, \quad (67)$$

⁷Unless the converse is enforced by a recoil handling in the $\bar{v}i$ dipole’s rest frame.

where \sqrt{S} is the centre-of-mass energy of the colliding hadrons. The limits on the invariants, detailed in eqs. (65) and (67), clearly differ from the ones of the FF scenario, cf. sec. 4.1. This implies that the II dipole splittings arise in phase-space regions being distinct from the FF case and thus with a different kinematics. Consequently, the energy fractions populate new ranges compared to the FF splittings, viz.

$$\begin{aligned} 0 &\leq x_{g/q} \leq a-1, \\ 1 &\leq x_{\bar{i}'/g_i}, x_i \leq 1+x_{g/q}, \\ 2 &\leq x_{\bar{i}'/g_i} + x_i \leq 1+a. \end{aligned} \quad (68)$$

The phase-space parametrization is better worked out separately for both relevant II dipole splitting channels.

5.1.1 Gluon emission phase space of initial–initial dipoles

First, the case of final-state gluon (g_f) emission, i.e. $\bar{i}'i \rightarrow \bar{i}'gi$, is discussed:

- The evolution variables are taken as suggested by eqs. (25) and (26). The Lorentz invariant p_\perp^2 thus reads

$$p_\perp^2 = \left| \frac{s_{\bar{i}'g} s_{gi}}{s_{\bar{i}'gi}} \right| = \frac{\hat{t} \hat{u}}{M^2} = M^2(1-x_i)(1-x_{\bar{i}'}), \quad (69)$$

and the Lorentz invariant y is given by

$$y = \frac{1}{2} \ln \left| \frac{s_{gi}}{s_{\bar{i}'g}} \right| = \frac{1}{2} \ln \frac{\hat{u}}{\hat{t}} = \frac{1}{2} \ln \frac{1-x_{\bar{i}'}}{1-x_i}, \quad (70)$$

such that the kinematic invariants can be re-written as

$$\begin{aligned} \hat{s} &= s_{0g} = s_{\bar{i}'i} = M^2 + 2M p_\perp \cosh y \geq M^2, \\ \hat{t} &= s_{0i} = s_{\bar{i}'g} = -M p_\perp e^{-y} \leq 0, \\ \hat{u} &= s_{0\bar{i}'} = s_{gi} = -M p_\perp e^{+y} \leq 0. \end{aligned} \quad (71)$$

- The bounds on the Mandelstam variables – or equally well – on the invariant energy fractions translate, of course, into bounds on the evolution variables. As for FF dipoles emitting gluons, the more restrictive requirement is obtained from

$$(a-1)M^2 = \hat{s}_{\max} - M^2 \geq \hat{s} - M^2 = -\hat{u} - \hat{t} = 2M p_\perp \cosh y. \quad (72)$$

Hence, the allowed phase space, which is depicted in the left part of fig. 3, is described quantitatively through

$$|y| \leq \operatorname{arcosh} \frac{(a-1)M}{2p_\perp}, \quad (73)$$

and⁸

$$p_{\perp, \max}^2 = \frac{(\hat{s}_{\max} - M^2)^2}{4M^2} = \frac{(a-1)^2 M^2}{4}. \quad (74)$$

⁸The maximal rapidity range is determined by the overall cut-off on p_\perp : $\hat{s}_{\max} - M^2 = 2M p_{\perp, \text{cut}} \cosh |y|_{\max}$.

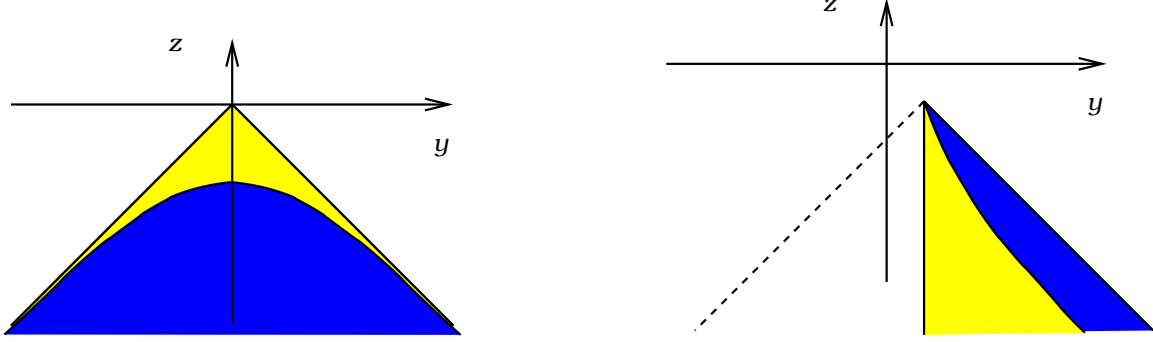


Figure 3: The accessible phase space for final-state (left panel) and initial-state (right panel) gluon emission off II dipoles. Bright colours indicate the phase-space fractions, which overestimate the respective allowed phase-space regions, which are shown in dark colours. The definitions of z are, $z = \ln \frac{p_{\perp}}{(a-1)M}$ and $z = \ln \frac{p_{\perp}}{aM}$ for g_f and g_i emissions, respectively. Notice that the visualization of the g_i emission phase space is for $a = 2$.

- Weaker constraints are obtained from

$$\hat{s}_{\max} - M^2 \geq \hat{s} - M^2 \geq -\hat{u}, -\hat{t} \quad (75)$$

and, as in the FF case, they result in symmetric rapidity limits,

$$|y| \leq \ln \frac{\hat{s}_{\max} - M^2}{M p_{\perp}} = \ln \frac{(a-1)M}{p_{\perp}}. \quad (76)$$

These estimates again can be visualized by a “triangle” in the $(y, z = \ln \frac{p_{\perp}}{(a-1)M})$ plane.

- The splitting kinematics will be detailed in sec. 5.1.3 together with that of the quark-emission process.

Compared to the FF case, a new issue emerges: the maximal partonic centre-of-mass scale \hat{s}_{\max} is not fixed and can be chosen. The actual choice then regulates the maximal size of the allowed emission phase space. This will be discussed together with the shower algorithm in sec. 7.

5.1.2 Quark emission phase space of initial–initial dipoles

Along the lines of the previous section, the phase-space parametrization and its consequences are now discussed for gluon emission into the initial state (g_i), i.e. (massless) quark emission into the final state: $\bar{q}_i i \rightarrow q g_i i$. The details of the kinematics as outlined in sec. 3.2 are as follows.

- The Lorentz invariant shower variables expressed through the Mandelstam variables read

$$p_{\perp}^2 = \left| \frac{s_{qg_i} s_{g_i i}}{s_{qg_i i}} \right| = -\frac{\hat{t} \hat{s}}{M^2} = M^2(x_i - 1)(1 + x_q), \quad (77)$$

$$y = \frac{1}{2} \ln \left| \frac{s_{g_i i}}{s_{qg_i}} \right| = \frac{1}{2} \ln \frac{\hat{s}}{-\hat{t}} = \frac{1}{2} \ln \frac{1 + x_q}{x_i - 1}. \quad (78)$$

This allows to rewrite the kinematic invariants as

$$\begin{aligned} \hat{s} &= s_{0q} = s_{g_i i} = +M p_{\perp} e^{+y} \geq M^2, \\ \hat{t} &= s_{0i} = s_{qg_i} = -M p_{\perp} e^{-y} \leq 0, \\ \hat{u} &= s_{0g_i} = s_{qi} = M^2 - 2M p_{\perp} \sinh y \leq 0, \end{aligned} \quad (79)$$

implying, compared to the case of g_f emission, a different shape of the valid (p_\perp, y) phase space covered by this type of emission.

- The accessible rapidity range is (cf. right panel of fig. 3)

$$\ln \left(\frac{M}{2p_\perp} + \sqrt{\frac{M^2}{4p_\perp^2} + 1} \right) = \operatorname{arsinh} \frac{M}{2p_\perp} \leq y \leq \ln \frac{aM}{p_\perp}, \quad (80)$$

where the left and right bounds result from $\hat{u} \leq 0$ and $\hat{s} \leq \hat{s}_{\max}$, cf. eq. (67), respectively. This can be visualized in the $(y, z = \ln \frac{p_\perp}{aM})$ plane as a “strip” that emerges in the point $(y_{\min}, z_{\max} = -y_{\min})$ and is confined between $z = -y - \ln a$ and $z = -y$. The equations $y_{\min} = \operatorname{arsinh} \frac{M}{2p_{\perp, \max}}$ and $\hat{s}_{\max} = M p_{\perp, \max} e^{y_{\min}}$ yield

$$y_{\min} = \frac{1}{2} \ln \frac{\hat{s}_{\max}}{\hat{s}_{\max} - M^2} = \frac{1}{2} \ln \frac{a}{a-1}, \quad (81)$$

and

$$p_{\perp, \max}^2 = (\hat{s}_{\max} - M^2) \frac{\hat{s}_{\max}}{M^2} = a(a-1) M^2. \quad (82)$$

- The allowed phase-space region is safely covered by a “half-triangle” described through $y_{\min} \leq y \leq -z$. Accordingly, $\Delta y = -z - y_{\min} = \ln(p_{\perp, \max}^2/p_\perp^2)/2$.
- The splitting kinematics is presented in the next subsection.

Finally, notice that, as for g_f emissions, the single-emission phase-space maximally available is determined by the actual value given to \hat{s}_{\max} .

5.1.3 Construction of the splitting kinematics

In the model proposed here the initial–initial dipole kinematics is directly constructed in the lab-frame. Particularly, to handle the recoils for the case of $\vec{q}_i' q_i$ dipoles, the strategy according to Kleiss [74, 75] has been implemented.

Lab-frame kinematics: the fixed orientation of incoming partons implies that the emitted parton’s recoil will directly be transferred to the entire final-state system, i.e. to all QCD and non-QCD final-state particles that are present before the emission takes place. As an example, consider the first emission in a Drell–Yan process, where the corresponding recoil is compensated for by the lepton pair. This recoil transfer results in $\tilde{p}_0 \neq p_0$, and, therefore, a Lorentz transformation \mathcal{T} defined through $p_0 = \mathcal{T} \tilde{p}_0$ is necessary and will be applied on all particles (whose vectors are summed up in \tilde{p}_0). For the construction of the momenta, a light-cone decomposition w.r.t. the beam axis is well suited, such that, for massless partons, the situation before and after the emission is summarized as

$$\begin{aligned} \tilde{p}_i &= (\tilde{x}_+ \sqrt{S}, 0, \vec{0}) \quad \rightarrow \quad p_i = (x_+ \sqrt{S}, 0, \vec{0}), \\ \tilde{p}_{\vec{v}'/\vec{q}_i} &= (0, \tilde{x}_- \sqrt{S}, \vec{0}) \quad \rightarrow \quad p_{\vec{v}'/\vec{q}_i} = (0, x_- \sqrt{S}, \vec{0}), \\ \tilde{p}_0 &= (M e^{\tilde{y}_0}, M e^{-\tilde{y}_0}, \vec{0}) \quad \rightarrow \quad p_0 = (M_\perp e^{y_0}, M_\perp e^{-y_0}, -\vec{\ell}_\perp), \\ &\quad p_{g/q} = (\ell_\perp e^{y_e}, \ell_\perp e^{-y_e}, \vec{\ell}_\perp). \end{aligned} \quad (83)$$

Furthermore, $\hat{s}_0 = \tilde{x}_+ \tilde{x}_- S = M^2$ and $\tilde{y}_0 = \tilde{y}_{\text{cm}} = \ln(\tilde{x}_+/\tilde{x}_-)/2$ with \tilde{y}_{cm} denoting the centre-of-mass rapidity of the parton system. The \tilde{x}_\pm , here functions of M , S and \tilde{y}_{cm} , parametrize the momentum fractions of the partons w.r.t their respective hadron. Employing $M_\perp^2 = M^2 + \ell_\perp^2$, after the emission they read

$$x_\pm = \frac{\ell_\perp e^{\pm y_e} + M_\perp e^{\pm y_0}}{\sqrt{S}} \geq \tilde{x}_\pm. \quad (84)$$

Clearly, emissions leading to $x_\pm > 1$ must be rejected. The vector $\vec{\ell}_\perp = (\ell_\perp \cos \varphi, \ell_\perp \sin \varphi)$ and the quantity y_e denote the transverse momentum and the rapidity of the emitted parton w.r.t. the beam axis, respectively. In terms of the Mandelstam variables, cf. eqs. (65), they are:

$$\ell_\perp^2 = \frac{\hat{t} \hat{u}}{\hat{s}} \quad \text{and} \quad e^{y_e} = \frac{e^{y_0}}{M_\perp \ell_\perp} (-\hat{t} - \ell_\perp^2). \quad (85)$$

The azimuthal angle φ can in first approximation be assumed to be uniformly distributed, and \hat{s} , \hat{t} , \hat{u} are determined by the evolution parameters p_\perp^2 and y through eqs. (71) and eqs. (79) for g_f and g_i emissions, respectively. The squared lab-frame transverse momenta are exemplified below as functions of p_\perp and y . For gluon emission into the final state,

$$\ell_\perp^2 = \frac{M^2 p_\perp^2}{\hat{s}} = \frac{p_\perp^2}{2 p_\perp M^{-1} \cosh y + 1}, \quad (86)$$

whereas for quark emission,

$$\ell_\perp^2 = \frac{M^2 p_\perp^2}{\hat{s}} - \frac{(M^2 + |\hat{t}|) |\hat{t}|}{\hat{s}} = (M e^{-y})^2 (2 p_\perp M^{-1} \sinh y - 1). \quad (87)$$

When comparing both equations for the same ratio p_\perp^2/\hat{s} , it becomes apparent that the emissions of quarks yield smaller lab-frame transverse momenta than those of gluons.

To fix the last degree of freedom, an additional assumption is necessary, which is to preserve the rapidity of the system of outgoing particles, $y_0 = \tilde{y}_0 = \tilde{y}_{\text{cm}}$.⁹ Having the complete emission at hand, $\hat{s} = x_+ x_- S$ and $y_{\text{cm}} = \ln(x_+/x_-)/2 = \ln(\hat{u}/\hat{t})/2 + y_e$.¹⁰ In more detail,

$$y_{\text{cm}} = \tilde{y}_{\text{cm}} + \frac{1}{2} \ln \frac{\hat{u}}{\hat{t}} + \ln \left(\frac{-\hat{t}(\hat{s} + \hat{u})}{\sqrt{M^2 \hat{s} \hat{t} \hat{u} + (\hat{t} \hat{u})^2}} \right) = \tilde{y}_{\text{cm}} + \frac{1}{2} \ln \frac{M^2 - \hat{t}}{\hat{s} + \hat{t}}, \quad (88)$$

which exposes the impact of the $y_0 = \tilde{y}_{\text{cm}}$ choice and shows that the system undergoes a rapidity shift during splitting. In addition, the new momentum fractions x_\pm can be written down,

$$x_\pm = e^{\pm y_0} \sqrt{\frac{\hat{s}}{S} \left(\frac{M^2 - \hat{t}}{\hat{s} + \hat{t}} \right)^{\pm 1}}. \quad (89)$$

Finally the momenta, $\tilde{p}_0^{(j)}$, of all final-state particles, numbered by j , have to be transformed in order to account for the non-trivial change of $\tilde{p}_0 \rightarrow p_0$. Here, the Lorentz transformation \mathcal{T} is specified as follows: the particles are boosted into the original dipole's centre-of-mass frame, afterwards the boost that forms p_0 out of $(M, \vec{0})$ is applied on them likewise. Altogether $p_0^{(j)} = \mathcal{B}(-\vec{p}_0/p_0^0) \mathcal{B}(\vec{p}_0/\tilde{p}_0^0) \tilde{p}_0^{(j)} = \mathcal{T} \tilde{p}_0^{(j)}$ is computed. This finalizes the construction of the on-shell kinematics of an individual emission.

⁹ If $y_{\text{cm}} = \tilde{y}_{\text{cm}}$ was naively exploited, the ratio of momentum fractions would remain constant, $x_+/x_- = \tilde{x}_+/\tilde{x}_-$, which constitutes a rather strange behaviour, since, for instance, very asymmetric starting configurations would persist to the end of the shower evolution.

¹⁰ Particularly, for gluon emissions into the final state, $y_{\text{cm}} - y_e = y$. This simply expresses that rapidity differences are invariant under boosts along the beam axis.

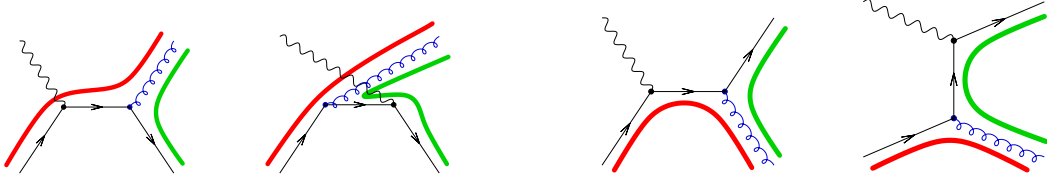


Figure 4: Relevant Feynman diagrams contributing to vector boson production in association with a gluon (left panel, showing the \hat{t} and \hat{u} channel graphs) or with a quark (right panel, visualizing the \hat{t} and \hat{s} channel graphs). The modified colour flows due to the emission are illustrated by the thick lines.

Improved description of lepton–hadron correlations (Kleiss trick): when analyzing eqs. (83) again, it is noticed that, apart from the azimuthal angle φ , which eventually fixes the vector $\vec{\ell}_\perp$, all unknown variables are determined by Lorentz invariants plus the additional assumption $y_0 = y_{\text{cm}}$.¹¹ In a first approximation, the choice is to uniformly distribute in azimuth w.r.t. the lab-frame, but more sophisticated schemes can be introduced correcting this simple ansatz. One such scheme can be derived from the work presented in [74] where it has been shown how to exactly factorize the first order tree-level corrections to the electroweak production of quarks. The corresponding Monte Carlo algorithm in fact is employed within the Lund CDM to arrange the splitting kinematics of $q_i \bar{q}'_i$ dipoles. In [75] this factorization was proven for scattering and annihilation processes involving initial states and corresponding algorithms were developed. Accordingly, for the $\bar{q}'_i q_i$ dipoles of this model, the suggestion of [75] has been employed to improve the splitting kinematics: the new momenta are constructed in the original dipole’s rest frame in a distinct way, then they are transformed to the lab-frame such that the 0-particle’s rapidity is preserved. The essence is that the primitive φ choice is substituted by a prescription, which e.g. in Drell–Yan processes correctly accounts for correlations between the radiated parton and the leptons. As before, the particles associated to the parent II dipole have to be transformed, however they now undergo a more complicated series of transformations out of the (before-emission) lab-frame, i.e. more accurately

$$p_0^{(j)} = \mathcal{B}_\parallel \left(\beta_3 = \frac{p_{0,+} - e^{2y_0} p_{0,-}}{p_{0,+} + e^{2y_0} p_{0,-}} \Big|_{\hat{z}\text{-align.f.}} \right) \mathcal{R}_{\hat{z}} \mathcal{B}_{\text{align}} \left(\frac{\vec{p}_{i'}/g_i + \vec{p}_i}{p_{i'}/g_i^0 + p_i^0} \Big|_{\text{dip.rf.}} \right) \mathcal{B}_\parallel \left(\frac{\vec{p}_0}{\tilde{p}_0^0} \right) \tilde{p}_0^{(j)}, \quad (90)$$

where starting from the right, one applies to a momentum: the longitudinal boost into the dipole’s rest frame, the alignment boost followed by the rotation that brings the newly incoming partons onto the light-cone axis maintaining the initial \pm assignments, and the final longitudinal boost to satisfy that y_0 stays the same as it was before the emission, i.e. $y_0 = \tilde{y}_0$.

5.2 Initial–initial dipole splitting functions

The first QCD-type emission in vector boson production (real-gluon bremsstrahlung or QCD Compton scattering) can be described as a coherent emission of a gluon or a(n) (anti)quark off the primary $\bar{q}_i q'_i$ dipole, cf. fig. 1. For gluon bremsstrahlung $\bar{q} q' \rightarrow V g$ (g_f emission) and QCD Compton scattering $g q' \rightarrow V q$ (g_i emission), the amplitudes can be worked out from the

¹¹Therefore, when neglecting the angle φ , it makes no difference whether the kinematics is arranged in the parent dipole’s rest frame or in the lab-frame.

Feynman diagrams depicted in fig. 4. The partonic squared matrix elements, with colour and spin indices averaged (summed) over initial (final) states, can then be expressed in terms of the Born amplitude squared as

$$\overline{|\mathcal{M}_{\bar{q}q' \rightarrow Vg}^{g_f}|^2} = \frac{N_C^2 - 1}{2N_C} 4\pi\alpha_s \frac{\overline{|\mathcal{M}_{\bar{q}q' \rightarrow V}|^2}}{M^2/2} \frac{M^4 + \hat{s}^2 - 2\hat{u}\hat{t}}{\hat{u}\hat{t}}, \quad (91)$$

and

$$\overline{|\mathcal{M}_{gq' \rightarrow Vq}^{g_i}|^2} = \frac{1}{2} 4\pi\alpha_s \frac{\overline{|\mathcal{M}_{\bar{q}q' \rightarrow V}|^2}}{M^2/2} \frac{M^4 + \hat{u}^2 - 2\hat{s}\hat{t}}{-\hat{s}\hat{t}}, \quad (92)$$

respectively, whereas the Mandelstam variables have been defined in eqs. (65). Again, in this particular case the factorization is exact and the equations above fix the dipole matrix elements $\hat{D}_{\bar{q}_i q'_i \rightarrow \bar{q}_i g q'_i(qg; q'_i)}$, which are in fact related to $D_{q\bar{q}' \rightarrow qg\bar{q}'}$ by crossing symmetry. The colour factor for the g_f emission is C_F . However, if the radiated gluon is assigned to the initial state, it actually is incoming and splits into a $q\bar{q}$ pair with one of the quarks entering the hard process. So, the colour averaging changes relative to the g_f case by $N_C/(N_C^2 - 1)$; therefore, the colour factor amounts to $T_R = \frac{1}{2}$.

For all initial–initial dipoles containing gluons, the dipole matrix elements may be obtained either directly in a similar way, or they are inferred from their final–final counterparts of the Lund CDM using crossing relations, $\hat{D}^{\text{II}} = \text{cross } \hat{D}^{\text{FF}}$, cf. secs. 3.3 and 4.2. The recoil strategies presented in sec. 5.1.3 lead to trivial rapidity Jacobians, $\frac{dy_{\text{cm}}}{dy_{\text{cm}}} = 1$. The initial–initial dipole splitting functions of eq. (38) are then fully specified: for gluons g_f emitted into the final state,

$$\begin{aligned} D_{\bar{i}'i \rightarrow \bar{i}'g_i}(p_\perp, y) &= \frac{f_{\bar{i}'}(x_\pm, \mu_F) f_i(x_\mp, \mu_F)}{f_{\bar{i}'}(\tilde{x}_\pm, \tilde{\mu}_F) f_i(\tilde{x}_\mp, \tilde{\mu}_F)} \xi_{\{F\}} C_{\{F\}} \frac{x_{\bar{i}'}^{n_{i'}}(p_\perp, y) + x_i^{n_i}(p_\perp, y)}{[x_{\bar{i}'}(p_\perp, y) + x_i(p_\perp, y) - 1]^2} \\ &\leq \mathcal{N}_{\text{PDF}} \xi_{\{F\}} C_{\{F\}} \left\{ \frac{2}{a+1} \right\} \equiv D_{\bar{i}'i \rightarrow \bar{i}'g_i}^{\text{approx}}(p_\perp, y), \end{aligned} \quad (93)$$

where the energy fractions are given as

$$x_{\bar{i}',i}(p_\perp, y) = 1 + \frac{p_\perp}{M} e^{\pm y}, \quad (94)$$

and, for gluons g_i radiated into the initial state,

$$\begin{aligned} D_{\bar{q}_i i \rightarrow qg_i}(p_\perp, y) &= \frac{f_g(x_\pm, \mu_F) f_i(x_\mp, \mu_F)}{f_{\bar{q}}(\tilde{x}_\pm, \tilde{\mu}_F) f_i(\tilde{x}_\mp, \tilde{\mu}_F)} T_R \frac{x_q^2(p_\perp, y) + x_i^{n_i}(p_\perp, y)}{[1 + x_q(p_\perp, y)]^2} \\ &\leq \mathcal{N}_{\text{PDF}} T_R \left\{ \frac{2}{a+1} \right\} \equiv D_{\bar{q}_i i \rightarrow qg_i}^{\text{approx}}(p_\perp, y), \end{aligned} \quad (95)$$

where the energy fractions are characterized by

$$x_{q,i}(p_\perp, y) = \mp 1 + \frac{p_\perp}{M} e^{\pm y}. \quad (96)$$

In both cases the overestimations $D_{\dots}^{\text{approx}}$ finally determine eikonal approximations to the improved splitting cross sections. The \mathcal{N}_{PDF} factors denote estimates for the respective upper bounds of the PDF ratios. The tilde variables refer to the before-emission state.

All splitting functions discussed here are finite, i.e. the (soft and collinear) singularities of the various differential splitting cross sections defined through eq. (28) are entirely contained in the

$1/p_\perp^2$ term of eq. (28). This nicely confirms that each eikonal cross section encodes the full singularity structure of the exact result. For g_f emissions, the invariant transverse momentum will tend to zero in either of the collinear limits that the gluon can have with the parent partons, i.e. the \hat{t} or \hat{u} variables turn independently to zero, or in the soft limit where $x_g \rightarrow 0$ and therefore \hat{t} and \hat{u} collectively approach the limit at zero. For g_i emissions, the divergence pattern is not as rich as for g_f emissions off II dipoles, since \hat{s} is bounded to stay well above zero owing to the mass of the parent dipole. So, it only is critical if the emitted quark becomes soft or collinear with the incoming splitting gluon g_i . No other radiating dipole contributes to this singularity, therefore $\xi \equiv 1$, consequently being omitted in the corresponding formulæ above.

The colour-factor assignment is unproblematic for quark dipoles $\bar{q}_i q'_i$ (see above) and also for gluon dipoles $g_i g_i$, where $C = C_A$ and $\xi = \xi_A = 0.5$. For II dipoles with a single gluon leg, the ambiguities beyond the large N_C limit appear in the same way as in the FF case. The following choices are currently made: final-state gluons are emitted adopting the Lund CDM choice of $C = C_A$ (and $\xi = \xi_A = 0.5$); for initial-state ones, $C = T_R$ (and $\xi = 1$) is selected adopting the result from the calculation for $\bar{q}_i q'_i$ dipoles. Since $\hat{s} \geq M^2 > 0$, the selection $C = T_R$ at least ensures the correct behaviour in the singular limit $\hat{t} \rightarrow 0$ of g_i emissions.

6 Dipoles from final-initial colour flows

The branching of an FI dipole, fi , caused by a gluon may occur again in two ways by either radiating it to the final state, or to the initial state, releasing an antiquark instead:

$$f(\tilde{k}) i(\tilde{\ell}) \rightarrow f(k) g i(\ell) \quad \text{and} \quad f(\tilde{k}) q_i(\tilde{\ell}) \rightarrow f(k) g_i \bar{q}(\ell). \quad (97)$$

6.1 Single-emission kinematics

Factorization implies that in deep inelastic scattering the evolution of the QCD particles proceeds completely independently of the evolution of the leptonic part. Therefore, not only the squared momentum transfer $q^2 = -Q^2$ from the lepton to the parton, probed by the scattering of the virtual photon, is a constant, but also $q^\mu = k_e^\mu - k_e'^\mu$ remains unaltered, when emitting QCD secondaries. This is used as the paradigm for the construction of the FI dipole kinematics in this model. Hence, similar to FF and in contrast to II dipoles, here the subsystem kinematically fully decouples from the rest of the cascade. Thus, in the FI case the partons directly participating in the splitting are affected only. Therefore,

$$\tilde{p}_0 \equiv p_0 \quad (98)$$

and

$$\tilde{p}_0 + \tilde{p}_{i/q_i} = \tilde{p}_f, \quad p_0 + p_{i/g_i} = p_f + p_{g/\bar{q}}, \quad \text{with} \quad \tilde{p}_0^2 = M^2 \equiv -Q^2 < 0, \quad (99)$$

such that Q may be interpreted as the “mass” of the parent dipole. Taking eqs. (18) and (19), the signature factors are $\tilde{\zeta}_f = \zeta_f = \zeta_{g/\bar{q}} = 1$, all other ones equal -1 . The underlying $2 \rightarrow 2$ process implies to define the kinematic invariants for radiating FI dipoles as

$$\begin{aligned} \hat{s} &= (p_0 + p_{i/g_i})^2 = (p_f + p_{g/\bar{q}})^2 = -Q^2(1 + x_{i/g_i}) \geq 0 \equiv \hat{s}_0, \\ \hat{t} &= (p_0 - p_f)^2 = (p_{g/\bar{q}} - p_{i/g_i})^2 = -Q^2(1 - x_f) \leq 0, \\ \hat{u} &= (p_0 - p_{g/\bar{q}})^2 = (p_f - p_{i/g_i})^2 = -Q^2(1 - x_{g/\bar{q}}) \leq 0, \end{aligned} \quad (100)$$

where the identification of the energy fractions and the bounds are again given for massless partons. The Mandelstam variables then satisfy

$$\hat{s} + \hat{t} + \hat{u} + Q^2 = 0 \quad \text{such that} \quad 2 + x_{i/g_i} = x_f + x_{g/\bar{q}}. \quad (101)$$

In analogy to the case of II dipoles, the maximal \hat{s} is parametrized in terms of Q^2 as

$$\hat{s}_{\max} = a Q^2 \quad \text{implying that} \quad 0 \leq \hat{s} \leq \hat{s}_{\max} \leq \mathcal{S}. \quad (102)$$

Here, the quantity $\mathcal{S} = (p_0 + P)^2$ plays the rôle, which the squared collider energy S does for II dipoles, namely representing the maximal upper bound. The use of $p_0 = \tilde{p}_0$ and the rigorous definition of the Björken- x variable,

$$x_B = \frac{Q^2}{2\tilde{p}_0 P}, \quad (103)$$

where P labels the momentum of the incoming hadron, lead to

$$\mathcal{S} = Q^2 \left(\frac{1}{x_B} - 1 \right). \quad (104)$$

This signifies that the Björken- x determines the maximal range for the parameter a , namely $0 \leq a \leq 1/x_B - 1$. Since parton masses are neglected, $\hat{s}_0 = (\tilde{p}_0 + \tilde{p}_{i/q_i})^2 = 0$ and the Björken- x is the momentum fraction \tilde{x} of the original incoming parton, $\tilde{p}_{i/q_i} = x_B P$. Employing $p_{i/g_i} = xP$, it is found that $x_B \leq x = -x_{i/g_i} x_B \leq (a+1)x_B \leq 1$ and the limits on x_{i/g_i} are clear:

$$\begin{aligned} -1 - a &\leq x_{i/g_i} \leq -1, \\ 1 + x_{i/g_i} &\leq x_f, x_{g/\bar{q}} \leq 1, \\ 1 - a &\leq x_f + x_{g/\bar{q}} \leq 1. \end{aligned} \quad (105)$$

The various other bounds then follow from eqs. (100) and (101).

6.1.1 Gluon emission phase space of final–initial dipoles

First, FI dipole gluon emissions emerging into the final state, $fi \rightarrow fgi$, are discussed according to the steps outlined in sec. 3.2:

- The evolution variables are identified as before by specifying eqs. (25) and (26) for the case at hand. They read

$$p_{\perp}^2 = \left| \frac{s_{fg} s_{gi}}{s_{fgi}} \right| = \frac{\hat{s} \hat{t}}{-Q^2} = Q^2 (|x_i| - 1)(1 - x_f), \quad (106)$$

and

$$y = \frac{1}{2} \ln \left| \frac{s_{gi}}{s_{fg}} \right| = \frac{1}{2} \ln \frac{-\hat{t}}{\hat{s}} = \frac{1}{2} \ln \frac{1 - x_f}{|x_i| - 1}, \quad (107)$$

whereas, using eqs. (100), the Mandelstam variables can be rewritten as

$$\begin{aligned} \hat{s} &= s_{0i} = s_{fg} = +Q p_{\perp} e^{-y} \geq 0, \\ \hat{t} &= s_{0f} = s_{gi} = -Q p_{\perp} e^{+y} \leq 0, \\ \hat{u} &= s_{0g} = s_{fi} = -Q^2 + 2Q p_{\perp} \sinh y \leq 0. \end{aligned} \quad (108)$$

Obviously, the rightmost relations for \hat{s} and \hat{t} are trivially fulfilled.

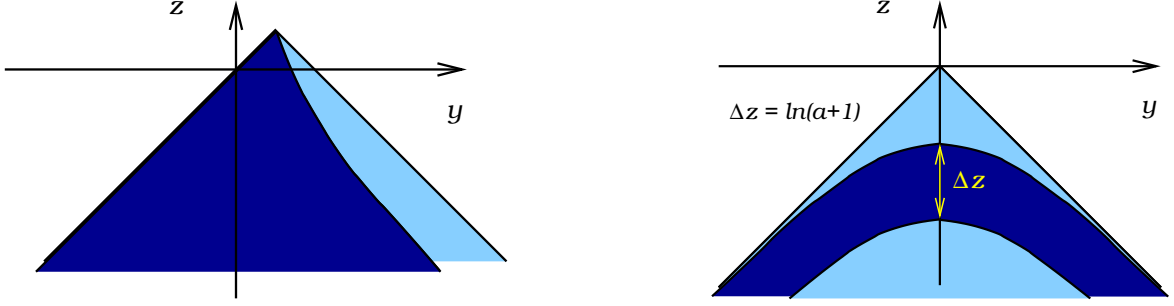


Figure 5: Phase-space visualization of the final-state (left panel) and initial-state (right panel) gluon emissions off FI dipoles. Again, dark colours indicate the available phase space for the emissions, whereas the fractions of phase space stemming from the overestimations are shown in bright colours. The definitions are, $z = \ln \frac{p_{\perp}}{aQ}$ and $z = \ln \frac{p_{\perp}}{(a+1)Q}$ for g_f and g_i emissions, respectively. Note that, for the visualization here, $a = 1$ has been assumed.

- The largest phase space available is found from $\hat{s} \leq \hat{s}_{\max}$, cf. eq. (102), and $\hat{u} \leq 0$, hence

$$-\ln \frac{aQ}{p_{\perp}} \leq y \leq \operatorname{arsinh} \frac{Q}{2p_{\perp}}. \quad (109)$$

In the $(y, z = \ln \frac{p_{\perp}}{aQ})$ plane, see left part of fig. 5, these bounds manifest themselves in a deformed “triangle”, whose right side is curved to the inside diverging for $y \rightarrow 0$ while approaching $z = -y - \ln a$ for $y \rightarrow \infty$. The left side of the “triangle” is described by $z \leq y$ and the intersection is at $(y = z_{\max}, z_{\max} = \ln \sqrt{1 + 1/a})$, suggesting that

$$p_{\perp, \max}^2 = a(a+1)Q^2 = (\hat{s}_{\max} + Q^2) \frac{\hat{s}_{\max}}{Q^2}. \quad (110)$$

Similar to II dipole splittings, the maximum size of the emission phase space is dictated by the choice of \hat{s}_{\max} , see eq. (102). This can easily be understood, since the emission implies a new initial state with a larger momentum fraction taken off the corresponding hadron.

- The exact rapidity interval is overestimated through the “triangle” bounds, which read $z \leq y \leq -z + 2z_{\max}$, resulting in $\Delta y = \ln(p_{\perp, \max}^2/p_{\perp}^2)$.
- Again, the construction of the momenta is separately detailed, see sec. 6.1.3.

6.1.2 Antiquark emission phase space of final-initial dipoles

In this subsection, the phase-space parametrization for gluon emission into the initial state, i.e. antiquark emission into the final state, is discussed for massless (anti)quarks, $f q_i \rightarrow f g_i \bar{q}$:

- According to eqs. (25), (26) and (100) the evolution variables read

$$p_{\perp}^2 = \left| \frac{s_{f g_i} s_{g_i \bar{q}}}{s_{f g_i \bar{q}}} \right| = \frac{\hat{u} \hat{t}}{Q^2} = Q^2(1 - x_{\bar{q}})(1 - x_f), \quad (111)$$

and

$$y = \frac{1}{2} \ln \left| \frac{s_{g_i \bar{q}}}{s_{f g_i}} \right| = \frac{1}{2} \ln \frac{\hat{t}}{\hat{u}} = \frac{1}{2} \ln \frac{1 - x_f}{1 - x_{\bar{q}}}. \quad (112)$$

The Mandelstam variables are then cast into the form

$$\begin{aligned}\hat{s} &= s_{0g_i} = s_{f\bar{q}} = 2Q p_\perp \cosh y - Q^2 \geq 0, \\ \hat{t} &= s_{0f} = s_{g_i\bar{q}} = -Q p_\perp e^{+y} \leq 0, \\ \hat{u} &= s_{0\bar{q}} = s_{fg_i} = -Q p_\perp e^{-y} \leq 0,\end{aligned}\tag{113}$$

where the inequalities for \hat{t} and \hat{u} are satisfied by construction.

- The requirement $0 \leq \hat{s} \leq \hat{s}_{\max} = a Q^2$ in conjunction with eqs. (113) leads to

$$\operatorname{arcosh} \frac{Q}{2p_\perp} \leq |y| \leq \operatorname{arcosh} \frac{\hat{s}_{\max} + Q^2}{2Q p_\perp} = \operatorname{arcosh} \frac{(a+1)Q}{2p_\perp},\tag{114}$$

where the inner and outer bounds follow from the lower and upper limits of the accessible \hat{s} interval, respectively. Concerning the former the central rapidity region becomes unaccessible for emissions of $p_\perp < Q/2$ (cf. right part of fig. 5). In the latter case the similarities to g_f emissions off II dipoles, cf. sec. 5.1.1, are fairly obvious. If the available squared energy \hat{s}_{\max} is fully used to generate the transverse momentum then $\cosh y \equiv 1$ and the maximal p_\perp is achieved, given by

$$p_{\perp,\max}^2 = \frac{(\hat{s}_{\max} + Q^2)^2}{4Q^2} = \frac{1}{4}(a+1)^2 Q^2.\tag{115}$$

As in all cases involving initial-state partons, the adjustment of the size of the phase space is triggered by the choice of \hat{s}_{\max} , which will be discussed in sec. 7.

- Loose constraints stem from $\hat{s}_{\max} + Q^2 \geq -\hat{t}, -\hat{u}$ and yield an increased phase space w.r.t. the precise one discussed above:

$$|y| \leq \ln \frac{\hat{s}_{\max} + Q^2}{Q p_\perp} = \ln \frac{(a+1)Q}{p_\perp}.\tag{116}$$

This invokes the usual “triangle” interpretation in the $(y, z = \ln \frac{p_\perp}{(a+1)Q})$ plane.

- The splitting kinematics will be discussed in the next subsection.

6.1.3 Construction of the emission momenta

The basic construction principles mentioned throughout secs. 3 and 5.1.3 are, of course, taken over when explicitly establishing the FI splitting kinematics. The kinematic decoupling, encoded as $p_0 \equiv \tilde{p}_0$, alleviates the task, since Lorentz transformations will only affect the local splitting. Thus, including the fact that the squared dipole momentum $\tilde{p}_0^2 = (\tilde{p}_f - \tilde{p}_{i/q_i})^2 = -Q^2$, the original dipole’s Breit-frame constitutes a suitable frame to set up the three new four-momenta. Using light-cone notation again, in this frame the momenta read

$$\begin{aligned}\tilde{p}_0 &= (-Q, Q, \vec{0}) \quad \rightarrow \quad p_0 = (-Q, Q, \vec{0}), \\ \tilde{p}_{i/q_i} &= (Q, 0, \vec{0}) \quad \rightarrow \quad p_{i/g_i} = (-x_{i/g_i} Q, 0, \vec{0}), \\ \tilde{p}_f &= (0, Q, \vec{0}) \quad \rightarrow \quad p_f = \left(\frac{(1-x_f)(-x_{i/g_i}-1)}{|x_{i/g_i}|} Q, \frac{x_f - x_{i/g_i} - 1}{|x_{i/g_i}|} Q, \vec{b}_\perp \right), \\ p_{g/\bar{q}} &= p_0 + p_{i/g_i} - p_f.\end{aligned}\tag{117}$$

The Breit-frame transverse momentum is given through $\vec{b}_\perp = (b_\perp \cos \varphi, b_\perp \sin \varphi)$, where

$$b_\perp = \frac{\sqrt{\hat{s}\hat{t}\hat{u}}}{\hat{s} + Q^2} = \sqrt{(1-x_f)(-x_{i/g_i}-1)(x_f-x_{i/g_i}-1)} \frac{Q}{|x_{i/g_i}|}. \quad (118)$$

Note that, for g_f emissions, it becomes zero for $\hat{u} \rightarrow 0$ (in this limit the rapidity value associated to this emission coincides with the y_+ bound, cf. sec. 6.1.1). This just happens independently of the actual value for the evolution variable p_\perp , therefore, ordering the emissions in p_\perp does not impose any ordering in b_\perp . Finally, the new Breit-frame momenta are transformed into the lab-frame.¹²

Using eqs. (117) the recoil strategy can directly be read off: before and after the splitting the initial-state parton is fixed to the $+$ direction of the light-cone decomposition, therefore to the beam axis¹³, leaving the recoil to be completely compensated for by the final-state particle. Of course, more sophisticated recoil strategies following the ones of the Lund model and/or the Kleiss idea are possible, but not yet implemented. Especially the prescription for quark scattering processes given in [75] seems very attractive, since it includes the correlations between leptons and partons associated to the lowest-order DIS process and the first emission.

6.2 Final-initial dipole splitting functions

For qq'_i dipoles emitting gluons, the two respective matrix-element factorizations of eq. (40) can directly be specified utilizing the results¹⁴ for the two typical real-correction processes to leading order DIS, namely the QCD Compton and the boson-gluon fusion processes. These are compared to the sole scattering of a quark caused by a space-like vector boson; hence, the dipole's gluon emission will again be treated coherently and, moreover, exact factorization is achieved as in all other quark-quark dipole cases. This yields the corresponding dipole matrix elements, both of which in fact reflecting the crossing symmetry of the $\hat{D}_{qq' \rightarrow qq'}$ term:

$$\hat{D}_{qq'_i \rightarrow qq'_i} = \frac{1}{Q^2} \frac{\hat{s}^2 + \hat{t}^2 - 2\hat{u}Q^2}{-\hat{s}\hat{t}} = -\frac{x_{q'_i}^2 + x_q^2}{Q^2(1+x_{q'_i})(1-x_q)} = \frac{x_{q'_i}^2 + x_q^2}{p_\perp^2}, \quad (119)$$

for g_f radiation off the qq'_i dipole where $C = C_F$, and

$$\hat{D}_{qq'_i \rightarrow qg_i q'} = \frac{1}{Q^2} \frac{\hat{u}^2 + \hat{t}^2 - 2\hat{s}Q^2}{\hat{u}\hat{t}} = \frac{x_{q'}^2 + x_q^2}{Q^2(1-x_{q'})(1-x_q)} = \frac{x_{q'}^2 + x_q^2}{p_\perp^2}, \quad (120)$$

for g_i radiation off the qq'_i dipole with $C = T_R$. For the definitions of the Mandelstam variables etc., see eqs. (100) and the previous section.

The dipole matrix elements of the FI dipoles containing gluon(s) are calculated either following the above procedure, or, alternatively, exploiting the crossing symmetry of the respective FF dipole matrix element taken from the Lund CDM. This completely determines the final-initial dipole splitting functions as introduced in eq. (39): for g_f emissions,

$$\begin{aligned} D_{fi \rightarrow fgi}(p_\perp, y) &= \frac{f_i(-x_i x_B, \mu_F)}{f_i(x_B, \tilde{\mu}_F)} \xi_{\{F\}} C_{\{F\}} \frac{|x_f(p_\perp, y)|^{n_f} + |x_i(p_\perp, y)|^{n_i}}{x_i^2(p_\perp, y)} \\ &\leq \mathcal{N}_{\text{PDF}} \xi_{\{F\}} C_{\{F\}} \left\{ \frac{2}{2(a+1)} \right\} \equiv D_{fi \rightarrow fgi}^{\text{approx}}(p_\perp, y), \end{aligned} \quad (121)$$

¹²This is done by inverting the transformations that (1) align the lab-frame momenta \tilde{p}_{i/q_i} and \tilde{p}_f and (2) rotate them afterwards onto the \hat{z} axis.

¹³Note that the choice $p_{i/g_i} = -x_{i/g_i} \tilde{p}_{i/q_i} = (-x_{i/g_i} x_B \sqrt{S}, 0, \vec{0})|_{\text{lab-f.}}$ is Lorentz invariant.

¹⁴Colour and spin final-state summed plus initial-state averaged squared matrix elements are e.g. given in [76].

with the energy fractions as functions of p_\perp and y reading

$$x_{f,i}(p_\perp, y) = \pm 1 - \frac{p_\perp}{Q} e^{\pm y}, \quad (122)$$

and, for g_i emissions (for antiquarks emitted into the final state),

$$\begin{aligned} D_{f q_i \rightarrow f g_i \bar{q}}(p_\perp, y) &= \frac{f_{g_i}(-x_{g_i} x_B, \mu_F)}{f_{q_i}(x_B, \tilde{\mu}_F)} T_R \frac{|x_f(p_\perp, y)|^{n_f} + x_{\bar{q}}^2(p_\perp, y)}{x_{g_i}^2(p_\perp, y)} \\ &\leq \mathcal{N}_{\text{PDF}} T_R \left\{ \frac{1}{\max\{2, a+1\}} \right\} \equiv D_{f q_i \rightarrow f g_i \bar{q}}^{\text{approx}}(p_\perp, y), \end{aligned} \quad (123)$$

where the energy fractions are then given in terms of the evolution variables by

$$x_{f,\bar{q}}(p_\perp, y) = 1 - \frac{p_\perp}{Q} e^{\pm y}, \quad \text{such that} \quad x_{g_i}(p_\perp, y) = -\frac{2p_\perp}{Q} \cosh y. \quad (124)$$

The modulus ensures that the terms in the rightmost numerator of the exact splittings are positive definite. Additionally, the eikonal approximations are displayed, which again overestimate the true form of the splitting functions.

As in the previous cases, the dipole splitting functions are finite, such that the divergences are fully encapsulated in the $1/p_\perp^2$ term. For gluons emitted into the final state, collinear/soft limits ($\hat{t} \rightarrow 0$ or/and $\hat{s} \rightarrow 0$) appear as before, where the (collinear) singularities for gluons are again only fully accounted through the inclusion of the contributions of the neighbouring dipoles (cf. the choice of ξ , $\xi = \xi_A = 0.5$).

If the gluon is radiated into the initial state, the incoming gluon may split collinearly and, therefore, in singular domains w.r.t. both the emitted antiquark ($\hat{t} \rightarrow 0$) and the “other” final-state parton associated to the emission ($\hat{u} \rightarrow 0$), cf. eqs. (100). This is in contrast to the situation of II dipoles where a collinear divergence cannot emerge between the incoming gluon and the “other” parton, since in this case it belongs to the initial state. Turning to the discussion of the soft infrared limit, the gluon g_i itself cannot become soft, since it is coupled to the initial state. Therefore, \hat{t} and \hat{u} cannot vanish at the same time, i.e. the soft limit is kinematically shielded, which is also clear from eqs. (105). In case a soft antiquark is being emitted, a singular effect only occurs once it is also collinear with the splitting gluon such that $\hat{t} \rightarrow 0$ (the associated disappearance of \hat{s} is non-singular).

The colour factors are chosen similarly to the previous cases, with the same reservations concerning the collinear limits. For FI dipoles, not only a final-state gluon emerging from a quark–gluon dipole gives rise to the ambiguities, in this case, also the antiquark emission into the final state induces them on the same level. This is related to the fact that this splitting, as already mentioned, is singular when either the emitted antiquark ($\hat{t} \rightarrow 0$) or the “other” parton ($\hat{u} \rightarrow 0$) in the final state become collinear with the initial-state gluon, cf. eqs. (100). The ambiguity here occurs when this “other” final-state parton is a gluon, apparently resulting in a collinear splitting governed by C_A rather than T_R .

7 The complete shower algorithm

In this section the dipole-shower algorithm is presented, which models the full QCD radiation picture in terms of initial-state, final–initial and final-state colour-dipoles on purely perturbative grounds. This formulation of the shower aims at resumming effects at leading logarithmic accuracy while producing exclusive final states of partons. These are generated in a Markovian

process, iterating individual emissions. In analogy to conventional parton showers, a Sudakov form factor constitutes the central probabilistic quantity that determines the full development of the cascade. This will be discussed first, before the procedure of evaluating the evolution variables that characterize a single emission briefly will be explained. Finally, the showering algorithm will be fixed by specifying its relevant parameters and scale choices.

7.1 The Sudakov form factor

The evolution variables are given by the invariant transverse momentum p_\perp and the invariant rapidity y , defined in eqs. (25) and (26), respectively. Since the dipole splitting functions $D(p_\perp, y)$, cf. eq. (28), are finite throughout, the entire singular structure of each emission cross section in each case is incorporated as a term $1/p_\perp^2$. The concept of “time” therefore is realized through p_\perp , which thus operates as the (leading) variable ordering the emissions within the cascade. Consequently, y is considered as the associated variable. Within the generic framework, cf. sec. 3, all emissions are treated on equal footing, resulting in a competition between different available channels at each evolution step. The Sudakov form factor is obtained from integrating the corresponding differential single-emission cross sections $\frac{d\mathcal{P}}{dp_\perp^2 dy}$ (which are positive definite) in suitable boundaries of p_\perp and y . Summing over all allowed splitting channels $\{\tilde{k}\tilde{\ell} \rightarrow kg\ell\}$ and exponentiating the negative result finally yields the Sudakov form factor:

$$\Delta(p_{\perp,\text{stt}}^2, p_\perp^2) = \exp \left\{ - \int_{p_\perp^2}^{p_{\perp,\text{stt}}^2} \frac{d\tilde{p}_\perp^2}{\tilde{p}_\perp^2} \mathcal{I}(\tilde{p}_\perp^2) \right\}, \quad (125)$$

where

$$\mathcal{I}(p_\perp^2) = \frac{\alpha_s[\mu_R(p_\perp)]}{2\pi} \sum_{\{\tilde{k}\tilde{\ell} \rightarrow kg\ell\}} \int_{y_-(p_\perp, a)}^{y_+(p_\perp, a)} dy D_{\tilde{k}\tilde{\ell} \rightarrow kg\ell}(p_\perp, y). \quad (126)$$

In this form the Sudakov form factor resums the leading logarithms as encoded in the dipole splittings to all orders, and, hence, can be interpreted as a no-branching probability. Accordingly, the two infrared divergent contributions of virtual and unresolvable real emission cancel each other below the infrared cut-off leaving an overall finite result. Thus, $\Delta(p_{\perp,\text{stt}}^2, p_\perp^2)$ quantifies how likely a state consisting of a number of dipoles will not emit any further resolvable parton between the start scale $p_{\perp,\text{stt}}^2$ and a lower (cut-off) scale p_\perp^2 . The quantity μ_R denotes the renormalization scale in energy units for the evaluation of the (running) strong coupling. Typically μ_R is given as a simple function of the evolution variables to include some higher-order virtual contributions beyond the leading-logarithmic approximation [77, 78]. If reduced to the case of FF dipole evolution only, the expression for the Sudakov form factor of course becomes equivalent to eq. (13) of the Lund CDM. Note that in the more general case, the rapidity limits y_\pm also depend on the scaling quantity a , cf. eqs. (67) and (102), i.e. on the choice of the maximal available phase space. Additionally, their actual functional form depends on the particular emission channel. For notational brevity, this has been omitted, but is clear in view of eq. (49), eqs. (73), (80) and (109), (114). The presence of the PDF ratios in the I/FI splitting kernels naturally yields a Sudakov form factor including these ratios. This resembles the typical backward evolution treatment, where the ratio of parton densities ensures that the parton composition of the hadron is properly reflected in each evolution step [9].

Finally, the actual differential probability (the probability density) for some branching to occur at p_\perp^2 then reads

$$\frac{dP}{dp_\perp^2} = \frac{d\Delta(p_{\perp,\text{stt}}^2, p_\perp^2)}{dp_\perp^2} = \frac{\mathcal{I}(p_\perp^2)}{p_\perp^2} \Delta(p_{\perp,\text{stt}}^2, p_\perp^2). \quad (127)$$

Subsequent emissions are ordered in p_\perp , i.e. their start scale $p_{\perp,\text{stt}}^2$ is identical to the p_\perp^2 of the last parton radiation. This generates the Markov chain. Note that this still leaves the initial starting scale – dubbed initializing scale – for the very first emission, $p_{\perp,\text{ini}}^2$, to be selected. The choices made here are detailed in sec. 7.3.

7.2 Generation of the emission's Sudakov variables

In the model a valid pair of evolution variables is generated by exploiting the strict p_\perp ordering, which enables to treat any dipole and each of its emission channels separately. Therefore, for each single channel, a trial (p_\perp^2, y) pair is generated according to its probability density

$$\begin{aligned} \frac{dP_{\tilde{k}\tilde{\ell} \rightarrow kg\ell}}{dp_\perp^2} &= \frac{\alpha_s[\mu_R(p_\perp)]}{2\pi p_\perp^2} \int_{y_-(p_\perp, a)}^{y_+(p_\perp, a)} dy D_{\tilde{k}\tilde{\ell} \rightarrow kg\ell}(p_\perp, y) \\ &\times \exp \left\{ - \int_{p_\perp^2}^{p_{\perp,\text{stt}}^2} \frac{d\tilde{p}_\perp^2}{\tilde{p}_\perp^2} \frac{\alpha_s[\mu_R(\tilde{p}_\perp)]}{2\pi} \int_{y_-(\tilde{p}_\perp, a)}^{y_+(\tilde{p}_\perp, a)} dy D_{\tilde{k}\tilde{\ell} \rightarrow kg\ell}(\tilde{p}_\perp, y) \right\}. \end{aligned} \quad (128)$$

A valid (p_\perp^2, y) pair generated according to the distribution eq. (127) is finally obtained by iterating over all channels picking the one of largest p_\perp^2 from the ensemble of all trial p_\perp^2 's.

The procedure of selecting such a trial (p_\perp^2, y) pair for a single dipole emission channel follows the standard Monte Carlo technique (hit-or-miss method) of the veto algorithm [3] exploiting that, for any given pair, the eikonal approximations gathered throughout secs. 4.2, 5.2 and 6.2 overshoot the respective dipole splitting cross sections.¹⁵ Each of which yields a fully integrable and invertible probability density, for which the (p_\perp^2, y) selection can be solved analytically using two random numbers. The respective simpler density can be easily read off eq. (128) when replacing $\alpha_s[\mu_R]$, y_\pm and $D_{\tilde{k}\tilde{\ell} \rightarrow kg\ell}$ by a sufficiently larger α_s^{max} , loose rapidity bounds Y_\pm (overestimating the actual rapidity interval) and approximate splitting functions $D_{\tilde{k}\tilde{\ell} \rightarrow kg\ell}^{\text{approx}}$, respectively. The correction to the true form of the single-channel density is then achieved by accepting the trial pair with a probability equal to the ratio (correction weight) reading

$$\mathcal{W} = \frac{\alpha_s(\mu_R)}{\alpha_s^{\text{max}}} \frac{D_{\tilde{k}\tilde{\ell} \rightarrow kg\ell}}{D_{\tilde{k}\tilde{\ell} \rightarrow kg\ell}^{\text{approx}}} \frac{\Delta y(p_\perp, a)}{\Delta Y(p_\perp, a)}. \quad (129)$$

However, there are additional kinematical constraints, such as the demand for valid momentum fractions $x_\pm \leq 1$ in II dipole evolution, see sec. 5.1.3; once violated, they translate into rejection of the trial emission, implying the generation of a new trial emission for the considered channel, starting over from the rejected p_\perp value.

¹⁵Both forms are positive definite and describe differential cross sections. Therefore, employing them as kernels in Sudakov exponentials will always yield Sudakov form factors smaller than one, such that these form factors can be interpreted as all-orders expressions in leading logarithmic accuracy for emitting no parton between two evolution scales.

Note that the PDF-ratio overestimations, \mathcal{N}_{PDF} , present in the approximate I/FI splitting functions are taken from a dynamically self-adapting table in order to improve the generation efficiency. The last term of above equation exhibits the correction for the exact rapidity interval, where $\Delta y = y_+ - y_-$ and $\Delta Y = Y_+ - Y_-$.

7.3 Scale choices, starting conditions and iteration principles

Finally, the remaining free scale choices are fixed. This completely defines the (default) cascade-generating algorithm of this shower model.

Renormalization scales:

$$\mu_{\text{R}}^2 \Big|_{\text{FF}} = \frac{p_{\perp}^2}{2} \quad \text{and} \quad \mu_{\text{R}}^2 \Big|_{\text{I/FI}} = 2z(1-z)p_{\perp}^2 = \frac{p_{\perp}^2}{1 + \cosh(2y)} \leq \frac{p_{\perp}^2}{2} \quad (130)$$

are used for the argument of the running strong coupling, where z is defined as a fraction of squared two-particle masses of the partons partaking in the emission:

$$z = \frac{|s_{kg}|}{|s_{kg}| + |s_{g\ell}|} = \frac{1}{1 + e^{2y}}. \quad (131)$$

An offset of $\mathcal{O}(1 \text{ GeV})$ ensures the evolution to proceed well above the Landau pole Λ_{QCD} .

Factorization scales: for a new (trial) emission μ_{F} is calculated according to

$$\mu_{\text{F}}^2 = (4k_{\perp}^2)^{d/2} \tilde{\mu}_{\text{F}}^{2-d}, \quad (132)$$

where $d = 1$ and $d = 2$ are employed for II and FI dipoles, respectively. The modified transverse momentum squared, k_{\perp}^2 , is computed from the emission's p_{\perp}^2 and y and the mass of the parent dipole. Based on eq. (86) k_{\perp}^2 is frame-independently defined as

$$k_{\perp}^2 = \frac{|s_{kg} s_{g\ell}|}{|s_{kg\ell}| + |s_{kg}| + |s_{g\ell}|} = \frac{|M| p_{\perp}^2}{|M| + 2p_{\perp} \cosh y}, \quad (133)$$

and intended to function as a more natural scale for the argument of the parton densities, since it better compares to the lab-frame squared transverse momentum. The respective old factorization scales associated with the state before the emission are encoded in the $\tilde{\mu}_{\text{F}}$ values, whereas, for the very initial case, $\tilde{\mu}_{\text{F,ini}}$ is adopted from the hard process.

Initializing scales: the subsequent cascading off the core process starts at the hardest scale, $p_{\perp}^2 = p_{\perp,\text{ini}}^2$, which can not be set independently of the underlying process. Generally it should guarantee that the shower strictly evolves in the soft and collinear phase-space regions only. Here, the following choices are made for three different scenarios of hard $2 \rightarrow 2$ processes:

- Showering off a single $q\bar{q}$ dipole as in $e^+e^- \rightarrow q\bar{q}$ processes: the start scale is set by the squared mass of the parent dipole, $p_{\perp,\text{ini}}^2 \Big|_{q\bar{q}\text{-prod.}} = \hat{s}_0 = M^2$.
- Showering off a single $\bar{q}_i q'_i$ dipole as in Drell–Yan processes: here, a $p_{\perp,\text{ini}}$ estimate is gained by inverting eq. (133) for $y = 0$, which yields

$$p_{\perp,\text{ini}} \Big|_{\text{DY}} = k_{\perp,\text{max}} \left(\frac{k_{\perp,\text{max}}}{M} + \sqrt{\frac{k_{\perp,\text{max}}^2}{M^2} + 1} \right), \quad (134)$$

and gives $p_{\perp, \text{ini}} \big|_{\text{DY}} = (1 + \sqrt{2})M$, provided that $k_{\perp, \text{max}}^2 = \hat{s}_0 = M^2$. For the same reason as in the previous item, this estimate is found by restricting the true transverse momentum of final-state gluons radiated off $\bar{q}_i q'_i$ dipoles, cf. eq. (86). For vector boson production, in this model, the first emission is matrix-element corrected per construction. Therefore, the restricted scale may be discarded, the shower instead evolve freely with the initializing scale set as largely as kinematically allowed.

- Showering off a multi-dipole state as in pure QCD jet production: recalling the definition $p_{\perp}^2 = |s_{kg} s_{g\ell}| / |s_{kg\ell}|$, all possible combinations for this fraction can be calculated using the strong particles provided by the hard process. The combination yielding the lowest p_{\perp}^2 should represent a sufficient estimate for the initializing scale. Applied to QCD jet production, the minimal numerator is given by $\min\{\hat{u}\hat{t}, \hat{s}\hat{t}, \hat{s}\hat{u}\}$ employing the Mandelstam variables of the $2 \rightarrow 2$ QCD core process. For the denominators, a mean squared mass determined by $\frac{1}{9}(\hat{s} + |\hat{t}| + |\hat{u}|)$ is used replacing the vanishing $|s_{kg\ell}|$. Taken together,

$$p_{\perp, \text{ini}}^2 \big|_{\text{Jets}} = \frac{9 \min\{\hat{u}\hat{t}, \hat{s}\hat{t}, \hat{s}\hat{u}\}}{\hat{s} + |\hat{t}| + |\hat{u}|}. \quad (135)$$

The assignment of large N_C colour flows is straightforward and unique for the first two examples. In the latter case, the most likely flow among the possible ones for a given set of partons will be determined by the actual kinematical configuration of the QCD $2 \rightarrow 2$ core process.

Maximal phase space: for II and FI dipole regimes, the limits on the evolution variables vary with the choices of the \hat{s}_{max} parameters restricting the phase space of a single emission for decreasing \hat{s}_{max} values, cf. eqs. (67) and (102). The default settings impose no extra restrictions, they hence are $\hat{s}_{\text{max}} \big|_{\text{II}} = S$ (see sec. 5.1) and $\hat{s}_{\text{max}} \big|_{\text{FI}} = S$ (see sec. 6.1) and allow full access to the centre-of-mass energy as given by the collider.

Cascading: each chain (colour-singlet), once appeared, is independently evolved, with the only potential exception of recoil transfer from an II splitting. This does not spoil the further evolution of the corrected chain owing to the Lorentz invariance of the shower formulation. Starting off $p_{\perp, \text{ini}}^2$ consecutive emissions are decreasingly ordered in p_{\perp}^2 within a chain. The dipole splitting that generated the largest p_{\perp}^2 in a certain evolution step is finalized in its kinematics, its p_{\perp}^2 is used as the new start scale for the trial emissions of the next round. The procedure continues until the infrared cut-off has been reached.

Cut-off and hadronization aspects: the cut-off is always taken on p_{\perp}^2 , hence denoted by $p_{\perp, \text{cut}}^2$. With a prescription avoiding the Landau pole in α_s , it can, in principle, be chosen arbitrarily small, since then the setting of the renormalization scale is safe and the Sudakov suppression quenches the appearing soft and collinear divergences.

After the cascading is finished, the interface to the hadronization – currently described through phenomenological models only – does not require any special treatment inside the shower. The conversion of the shower partons into primary hadrons proceeds similarly to the case of conventional parton cascades.

8 First results

In this section, the newly developed dipole shower is validated by comparing its predictions of QCD dynamics to data and other Monte Carlo calculations. To this end, the following physics

processes are studied:

- the production of vector bosons and their subsequent hadronic decays in e^+e^- collisions at LEP1 energies,
- the inclusive production of Drell–Yan e^+e^- pairs at Tevatron and future LHC energies, and,
- the inclusive QCD production of jets at Tevatron energies.

The shower model presented here has been implemented into the event generator SHERPA, and supplemented by an interface to the Lund string fragmentation routines of PYTHIA 6.2 [3], which are provided by the SHERPA framework. Cascading starts off the corresponding hard $2 \rightarrow 2$ processes, which are generated inside SHERPA utilizing its facilities of evaluating matrix elements. Only light-quark flavours, i.e. massless quarks, are considered. For the simulation of hadronic collisions, all predictions have been obtained from the CTEQ6L set of PDFs [79]. In accordance with the choice in the PDF, the strong coupling constant has been fixed by $\alpha_s(M_Z) = 0.118$ and its running is taken at the two-loop level. The dipole-shower cut-offs related to final-initial and initial-initial dipole evolution are both set to 1 GeV, i.e. $p_{\perp,\text{cut}}^2|_{\text{FI}} = p_{\perp,\text{cut}}^2|_{\text{II}} = 1 \text{ GeV}^2$. In contrast, $p_{\perp,\text{cut}}^2|_{\text{FF}}$ is tuned by hand together with the Lund string model parameters. The lower panel in each of the plots presented below visualizes the (MC–reference)/reference ratio, where the “reference” (ref) is given by the data as long as they are available. The bright band always illustrates the uncertainty of the respective measurement.

8.1 Hadron production in electron–positron collisions

The testbed to exclusively validate the performance of the sole final-state piece of the dipole-shower model¹⁶ is the process $e^+e^- \rightarrow Z^0/\gamma^* \rightarrow \text{hadrons}$, where the $q\bar{q}$ pair produced in the hard process will initiate the cascade. The QCD Monte Carlo predictions can be compared with large sets of data, which, for example, are available from the LEP1 measurements. The data precisely test the QCD dynamics of hadronic final states produced at the Z^0 pole. The parameters of the shower and the hadronization model were tuned by hand, i.e. the value taken for the strong coupling at M_Z was specified, the FF cut-off $p_{\perp,\text{cut}}^2|_{\text{FF}}$ of the dipole shower was adjusted, and, suitable values for the Lund string model parameters a (PARP(41)), b (PARP(42)) and σ_q (PARP(21)) were found. The method employed for that is sufficient to yield first significant results. However, it can not be compared to the effort of delicate Monte Carlo tuning procedures as presented in [81] and foreseen in [82] in order to automatize the procedure. The “naively” tuned parameters read:

$$\begin{aligned}
 \alpha_s(M_Z) &= 0.1254, \\
 p_{\perp,\text{cut}}^2|_{\text{FF}} &= 0.54 \text{ GeV}^2, \\
 a &= 0.29, \\
 b &= 0.76 \text{ GeV}^{-2}, \\
 \sigma_q &= 0.36 \text{ GeV}.
 \end{aligned}
 \tag{136}$$

Since massive quarks are not handled yet, the dipole shower always started off massless $q\bar{q}$ pairs. At $S = M_Z^2$ a mean parton multiplicity of $\langle \mathcal{N}_{\text{parton}} \rangle = 9.24$ and a mean charged-particle

¹⁶Note that, for pure final-state cascading, the splitting of gluons into quark–antiquark pairs already has been included, and the implementation is nearly identical to the treatment proposed in the Lund CDM.

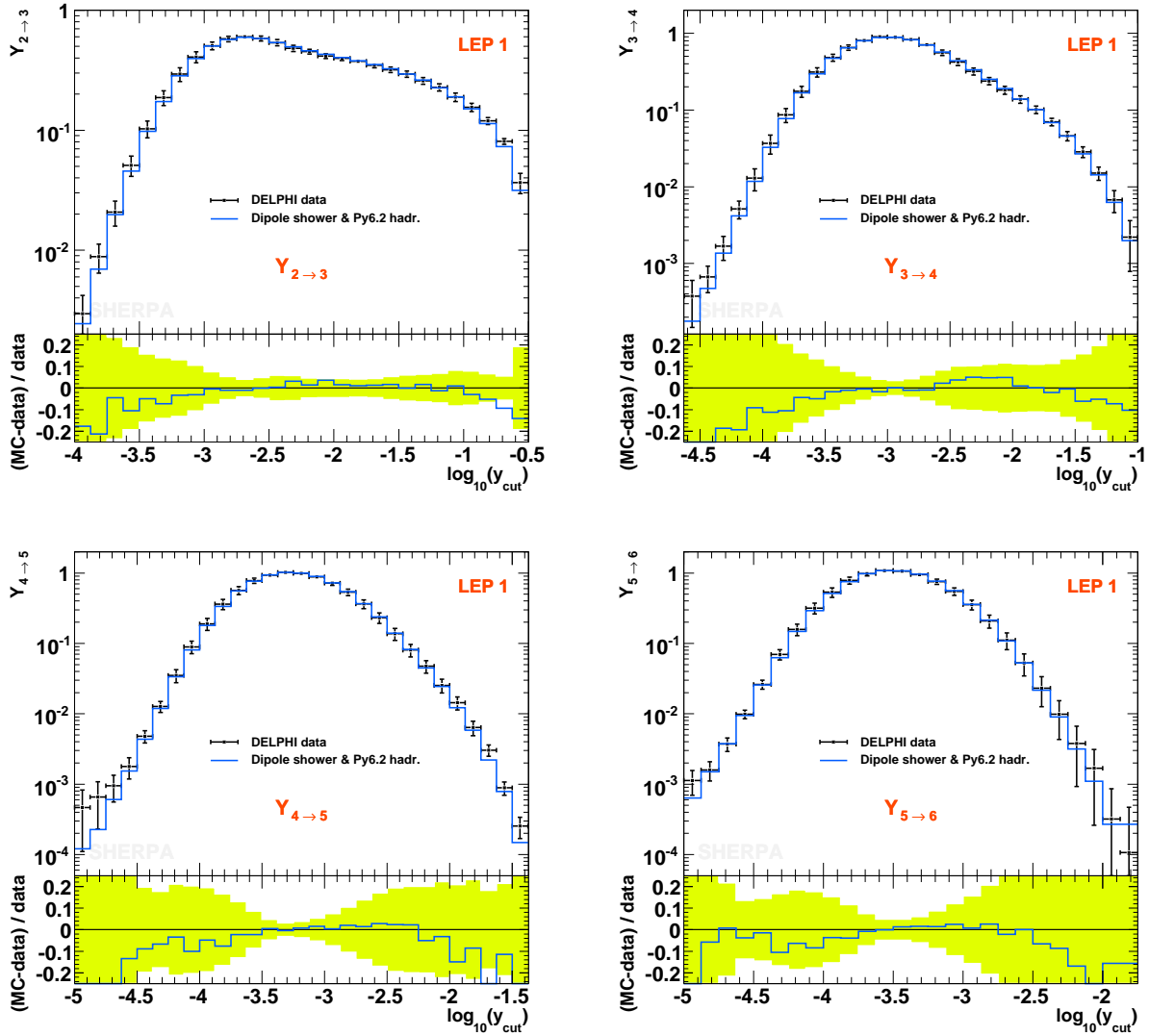


Figure 6: Durham differential jet rates as a function of the jet-resolution parameter y_{cut} ; dipole-shower prediction vs. DELPHI data taken from [80]. Here, the light-coloured band represents the sum of the statistical and systematic errors.

multiplicity of $\langle \mathcal{N}_{\text{ch}} \rangle = 20.47$ are found, where the latter is somewhat below the experimentally detected value of $\langle \mathcal{N}_{\text{ch}} \rangle = 20.92 \pm 0.24$ [22]. Figs. 6 and 7 show a selection of distributions obtained with the dipole shower and compared to DELPHI data taken at $\sqrt{S} = 91.2$ GeV during the LEP1 run. In fig. 6, Durham differential jet rates, $Y_{n \rightarrow n+1}$, are presented up to $Y_{5 \rightarrow 6}$. They disentangle at which $y_{\text{cut}} = 2 \min\{E_i^2, E_j^2\}(1 - \cos \theta_{ij})/S$ values an $n + 1$ jet event is merged into an n jet event according to the Durham jet clustering scheme [83]. The agreement with the data taken by the DELPHI experiment [80] is very good, in particular the description around the peak positions. All predictions tend to be somewhat below the bin means for low and high values of the jet-resolution parameter y_{cut} .

Event shape variables probe the pattern of QCD radiation for both soft and hard emissions arising from the primary $q\bar{q}$ dipole. Therefore, in fig. 7, the shape distributions of 1–thrust,

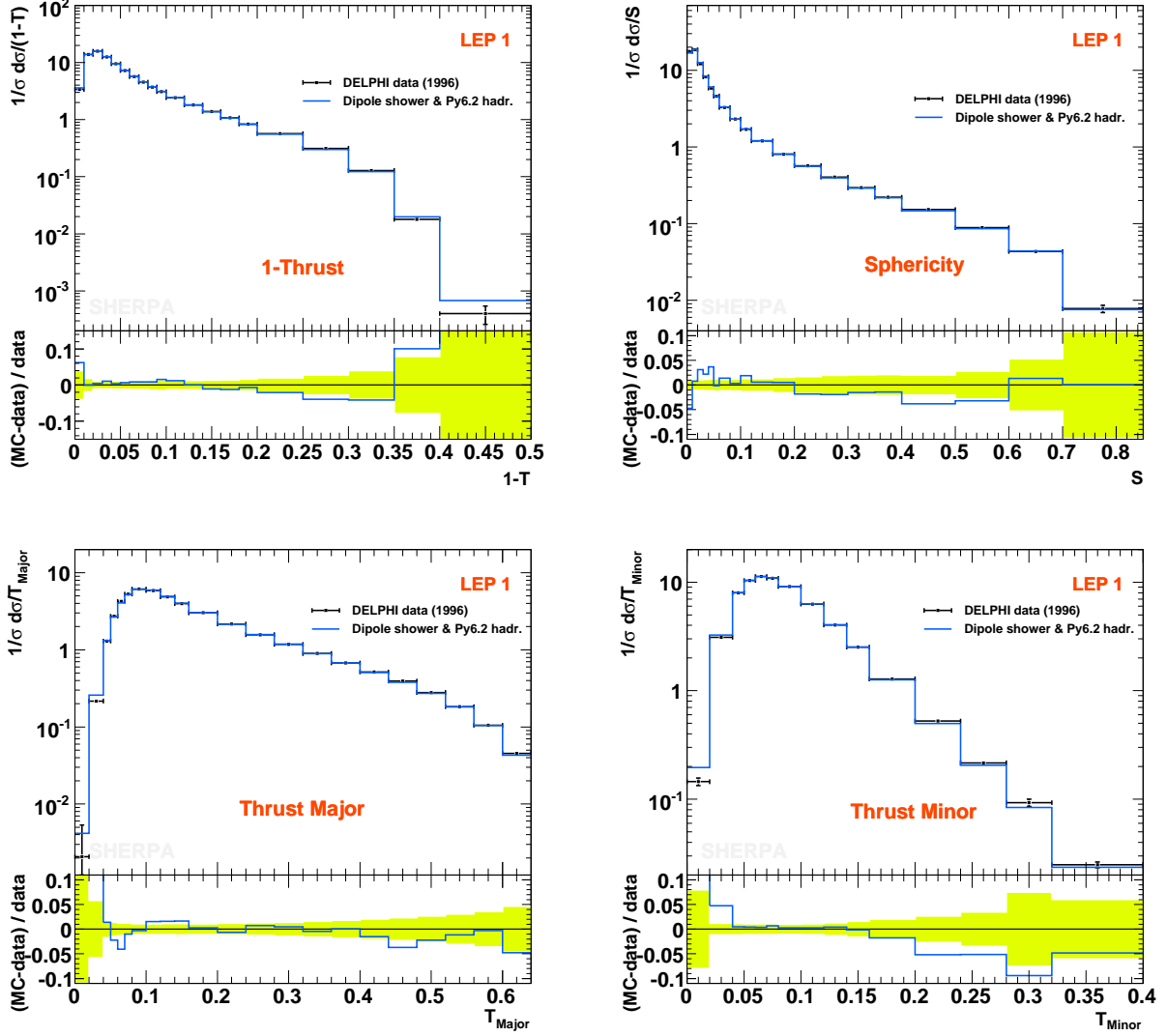


Figure 7: The dipole-shower predictions for the event shapes 1–thrust, sphericity, thrust major and thrust minor vs. DELPHI data [22]. Again, the light-coloured band represents the sum of the statistical and systematic errors.

$1 - T$, thrust major, T_{major} , and thrust minor, T_{minor} are displayed together with the sphericity, S , placed in the top right corner of the figure. The former are all obtained from a linear momentum tensor, whereas the latter stems from a quadratic one, thus, puts more emphasis on high momenta. All dipole-shower results are compared, once again, to DELPHI data [22]. The low-value parts, which are sensitive to soft emissions, are all quite well described, except for larger deviations in thrust major and minor. Differences in these observables also appear, even somewhat larger, for instance for the new shower of HERWIG++ [27] and the new shower presented in [36] based on Catani–Seymour dipole factorization. For a very recent comparison, please cf. [84], where the value of the strong coupling constant has been determined at the Z^0 pole using the results from a first NNLO calculation for $e^+e^- \rightarrow 3$ jets [85]. Although the soft parts of these distributions are all affected by hadronization corrections and their careful

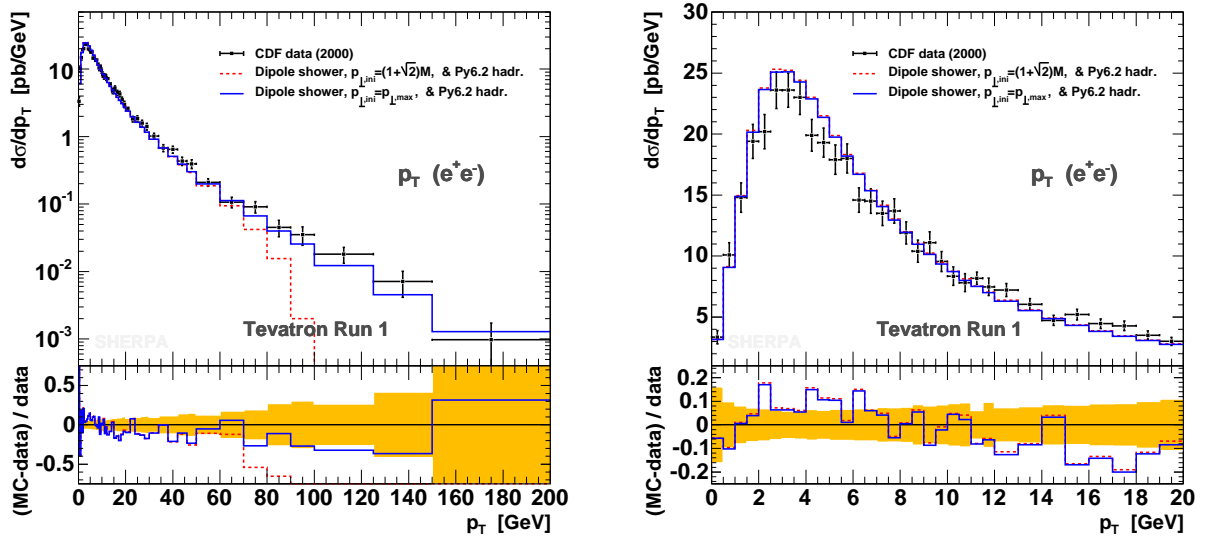


Figure 8: Boson transverse-momentum distribution in $e^+e^- + X$ as predicted by the dipole shower for two different choices concerning the initializing scale. The Monte Carlo calculations are compared with CDF data [86] taken during Run I at the Fermilab Tevatron. The right panel depicts the very soft region of the distribution only.

modelling and tuning, the good behaviour of the dipole shower in describing soft emissions can be seen as a consequence of exponentiating the eikonal rather than the collinear limit of QCD radiation. The predictions for hard emissions agree somewhat worse with the data. The last two bins of the 1–thrust distribution are overestimated signalling a slight excess of spherical events, whereas thrust minor is underestimated for high values.

Taken together, the agreement with data is satisfactory. This allows to conclude that the final-state piece of the dipole shower sufficiently is under good control.

8.2 Inclusive production of Drell–Yan lepton pairs at hadron colliders

In the scope of hadronic collisions, the processes $pp(p\bar{p}) \rightarrow Z^0/\gamma^* \rightarrow e^+e^-$ constitute the simplest and cleanest testbed for the further validation of the dipole shower as they form the initial–initial dipole counterpart of the $q\bar{q}$ timelike evolution.

Tevatron Run I predictions

The transverse-momentum distribution of the lepton pair is heavily influenced by additional QCD radiation arising in both soft and hard phase-space domains. Owing to its clear signal, this spectrum has been measured with high precision by the Tevatron experiments. It is shown in fig. 8 for lepton-pair invariant masses in the range $66 \text{ GeV} < M_{ee} < 116 \text{ GeV}$. Two hadron-level predictions produced by the dipole shower are confronted with data from a CDF measurement at $\sqrt{S} = 1.8 \text{ TeV}$ [86] and normalized to the experimental inclusive cross section. They differ in their choice of the initializing scale, using, first, $p_{\perp,\text{ini}} = (1 + \sqrt{2})M_{ee}$ and, second, $p_{\perp,\text{ini}} = p_{\perp,\text{max}}$ (cf. eqs. (74) and (82)). In the latter case the shower evolves totally unconstrained, exploiting the fact that the first emission is corrected for the true matrix element by construction and may hence appear at a scale exceeding M_{ee}^2 . This in turn sets the highest scale for all consecutive

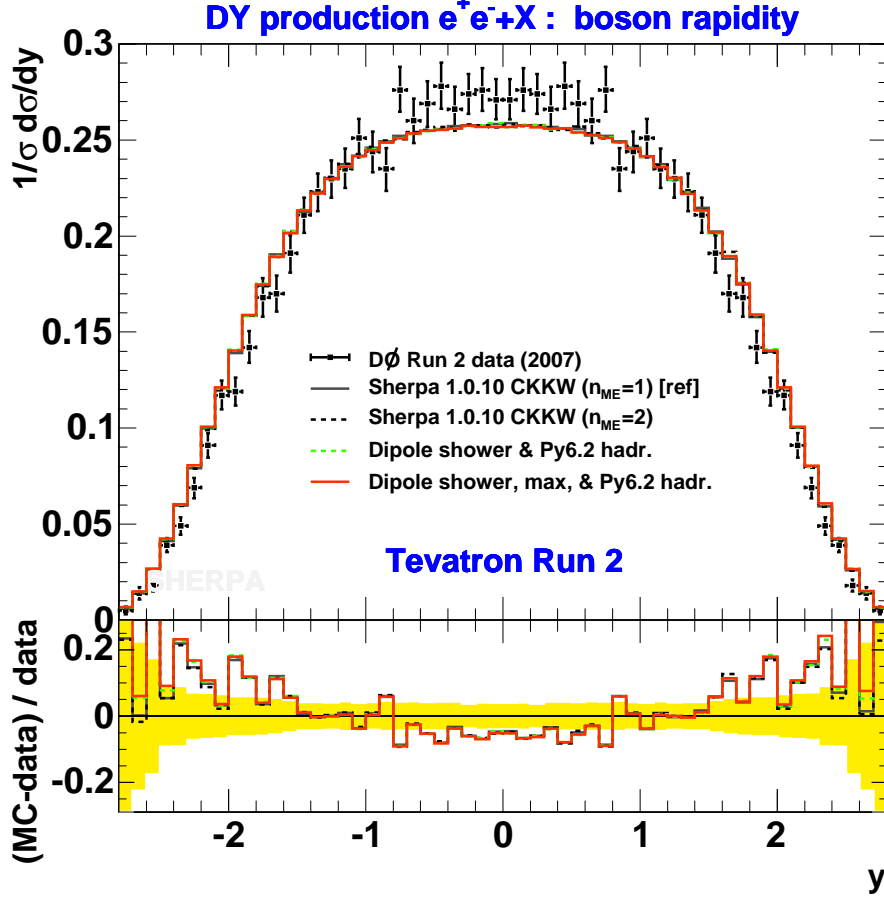


Figure 9: Rapidity spectrum of the vector bosons in inclusive Z^0/γ^* production at Tevatron Run II energies of $\sqrt{S} = 1.96$ TeV as predicted by SHERPA and the dipole shower in comparison to recent $D\bar{O}$ data [87]. The grey solid, the black dashed, the green dashed and the red solid lines give the SHERPA CKKW $n_{ME} = 1$, CKKW $n_{ME} = 2$, the default and the unconstrained dipole-shower predictions, respectively.

emissions. The whole treatment eventually leads to a good agreement with the data for large p_T . In contrast, the dipole shower with restricted initializing scale gradually undershoots data above $p_T = 60$ GeV before it dies off rapidly around $p_T = 80$ GeV.

The figure's right part contains a close-up of the peak region on a linear scale, almost identically predicted by both dipole-shower variants. The turn-on of the distribution is well described. Around the peak, narrower described by the data, a slight excess is found, followed by an underestimation of the data for the region above 12 GeV. The predictions include an additional improvement for very low p_T , namely an intrinsic transverse-momentum smearing, which has been tuned by hand to these low p_T data according to a Gaussian to have a mean(width) of 0.3(0.4) GeV.¹⁷ Without this correction the shower p_T spectra would slightly shift to the left.

¹⁷The assignment of an intrinsic transverse momentum to the hard process is a non-perturbative correction applied after the shower phase, and, therefore, irrelevant for shower kinematics.

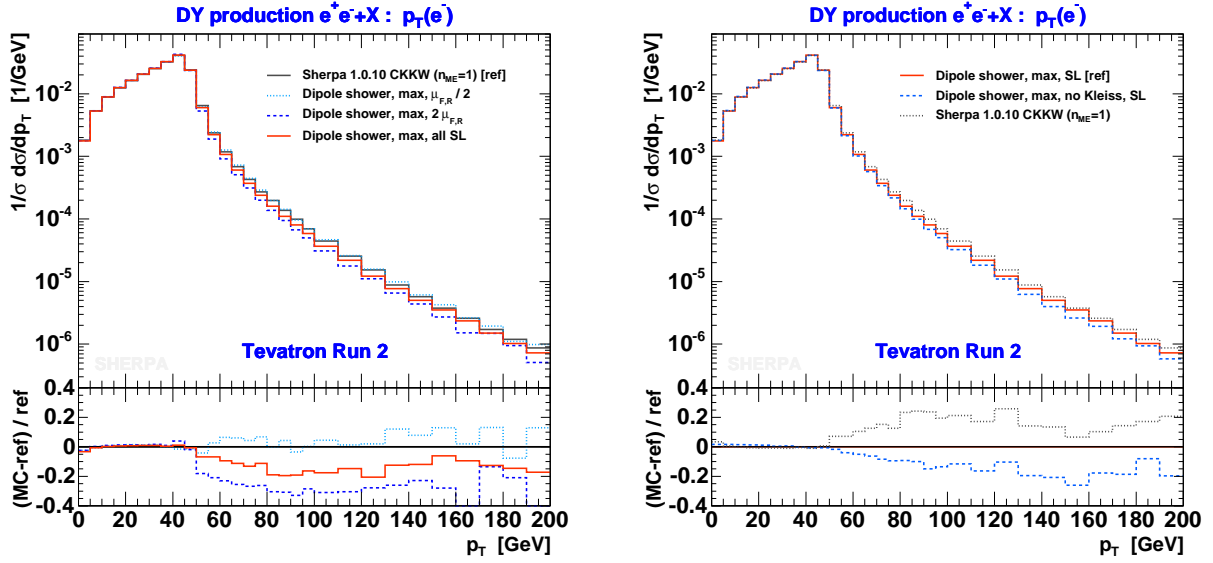


Figure 10: Left panel: impact of standard scale variations on the shower evolution exemplified by means of the $p_{T,e}$ distribution. Here, the blue lines reflect the uncertainty of the prediction from the unconstrained shower, in both panels given by the red solid line. Right panel: impact of the Kleiss correction on the transverse-momentum distribution of the e^- . Here, the blue dashed and the grey dotted lines denote the outcome of the unconstrained dipole shower neglecting Kleiss corrections and of the SHERPA CKKW $n_{ME} = 1$ merging, respectively. Both panels depict shower-level (SL) results (lacking hadronization corrections).

Tevatron Run II predictions

One more validation against data is presented by considering the rapidity distribution of the decaying vector boson, where the Drell–Yan lepton-pair mass has been restricted to the interval $71 \text{ GeV} < M_{ee} < 111 \text{ GeV}$. The QCD NNLO theoretical prediction for this inclusive observable has been calculated in [88] and very good agreement with data from a recent $D\bar{O}$ measurement [87] has been observed over the full rapidity range.

Here, hadron-level predictions are presented that have been obtained from the unconstrained dipole shower – denoted by “Dipole shower, max” in the plots from now – as well as from the $p_{\perp,ini}$ restricted dipole shower, which is taken as the default, since the matrix-element correction of the first emissions does not apply beyond Drell–Yan processes. The comparison also shows SHERPA outcomes resulting from the CKKW merging of parton showers and tree-level matrix elements up to n_{ME} extra partons. This merging method has been validated in many other comparative studies [53, 63, 89, 90] or even to data [91]. Here, two such inclusive samples, for $n_{ME} = 1$ and $n_{ME} = 2$, were generated with SHERPA using its version 1.0.10. All results are displayed in fig. 9 and confronted with the $D\bar{O}$ data [87]. There hardly are any shape differences visible between the various Monte Carlo predictions. This nicely confirms that the II dipole kinematics is eventually well fixed by preserving the rapidity of the final-state particles, cf. sec. 5.1.3. However, compared to data, all Monte Carlo shapes are somewhat wider showing an excess of up to 20% for large rapidities.

A rough estimate for the uncertainty of the shower predictions can be gained from varying the values taken for the μ_F and μ_R scales within the shower algorithm. To this end, their defaults

were multiplied/divided by 2. The μ_F scale enters through the PDF weight, and μ_R as the scale of the running strong coupling in the single-emission probabilities, cf. sec. 7.2. This is exemplified in the left plot of fig. 10 for the $p_{T,e}$ distribution, where the uncertainty band for the unconstrained (intrinsically first-order matrix-element corrected) dipole shower is shown to cover the same-order-of-accuracy prediction stemming from CKKW $Z^0 + 1$ jet merging. Therefore, both descriptions are in good agreement. The right part of fig. 10 is the verification for the importance of the Kleiss corrections for emissions off $\bar{q}'_i q_i$ dipoles. Their application yields a hardening and, therefore, an improvement of the single-lepton $p_{T,e}$ spectrum of about 20%. SHERPA CKKW $n_{ME} = 1$ again serves as a good reference, since it accounts for the full first-order lepton-hadron correlations.

LHC predictions

The correct energy extrapolation of the dipole shower is now verified by comparing various approaches at LHC centre-of-mass energies. Therefore, the unconstrained dipole shower is studied w.r.t. SHERPA's CKKW merging for $n_{ME} = 1, 2, 3$ and SHERPA's pure showering realized by APACIC++ [14, 92], which is a virtuality-ordered parton shower in the traditional sense resumming large logarithms in the collinear rather than the soft limit of QCD radiation.

Most of the observables presented here require the exclusive definition of jets, which has been attained according to the Run II k_T algorithm [93, 94] using the parameter $D = 1$ and an unconstrained η range in order to include forward-jet effects. The jet p_T threshold is given by $p_{T,jet} > 20$ GeV. All distributions are simulated at the hadron level and normalized to unit area, which allows for direct shape comparisons. Many plots show CKKW predictions for $n_{ME} > 1$, which helps estimate the impact of describing the next-to-first extra parton emission by matrix elements as well.

The pseudo-rapidity and p_T distributions of the e^+e^- pairs are shown in fig. 11. They are largely determined by the pattern of QCD emissions, in particular by the hardest one, and measure the recoil of the lepton pair against all other final-state particles. Hence, these inclusive observables are first defined beyond the leading order Drell-Yan pair production process. For the η_{ee} spectrum shown in the left panel, the maxima and the central rapidity region are somewhat more and less pronounced by the dipole shower than by the CKKW predictions, respectively. As it can be seen, the improved description of second-order emissions results in a further enhancement of vector bosons that are central in η space. In contrast, the APACIC++ prediction features a considerably larger dip in the central pseudo-rapidity region as a consequence of lacking sufficiently hard emissions, since this shower's start scale is constrained by the mass of the lepton pair to ensure evolving in the collinear and soft phase-space regions only. The right part of fig. 11 contains the $p_{T,ee}$ distribution on a double-logarithmic scale to provide good insight to both soft and hard p_T domains. In the hard tail the dipole-shower result is 30% below the CKKW reference; the difference in the low p_T part amounts up to 40%, whereas the dipole shower clearly puts emphasis on the soft region and predicts a slightly lower peak position. The agreement is still satisfactory and the deviations can be traced back, for the very soft part, to different parameter settings for the fragmentation of the partons (including intrinsic k_T smearing), for the range $1 \text{ GeV} < p_T < 20 \text{ GeV}$, to different radiation patterns generated by the dipole shower and the vetoed APACIC++ shower used for the CKKW merging, and, for the high p_T tail, to differences in choosing and processing the scales in both approaches. Typically, the inclusion of next-to-one extra parton emissions at the matrix-element level leads to a further increase of the high p_T tail. This is found in fig. 11 where the effects can become as large as 40%.

Fig. 12 presents the jet pseudo-rapidity, η_i , and transverse-momentum, $p_{T,i}$, distributions of the first three jets. These observables directly probe the jet structure of the events. For η_i , the

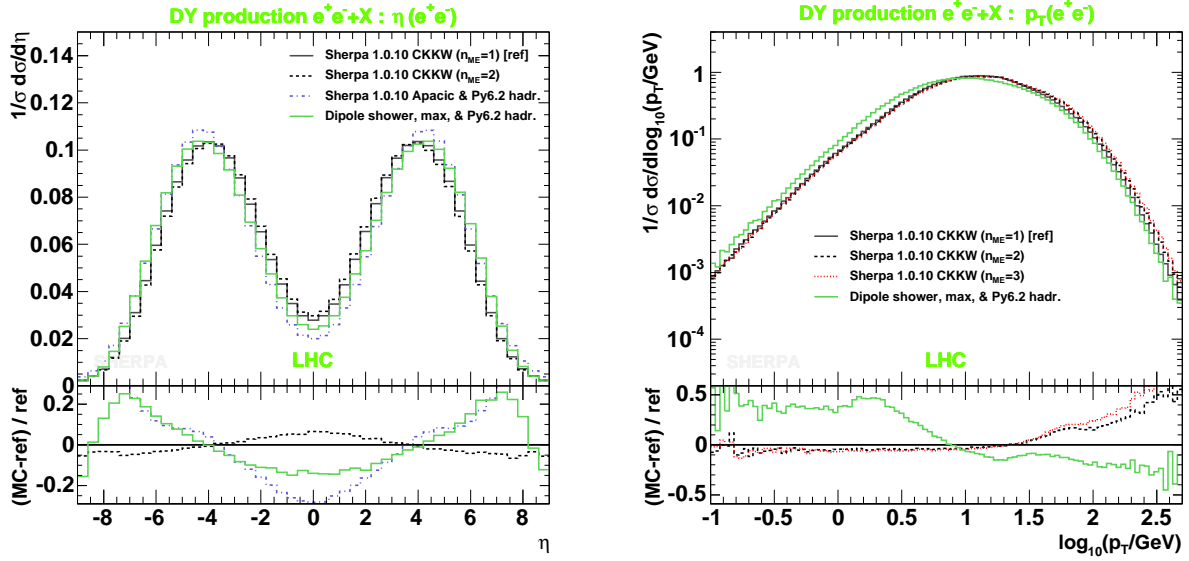


Figure 11: Pseudo-rapidity spectrum (left) and p_T distribution of the lepton pair in inclusive $Z^0/\gamma^* + \text{jets}$ production at the LHC. The comparison is at the hadron level between the unconstrained dipole shower (green solid lines) and various SHERPA results, namely CKKW $n_{\text{ME}} = 1$ (grey solid lines), taken as the reference curve, CKKW $n_{\text{ME}} = 2$ (black dashed lines), CKKW $n_{\text{ME}} = 3$ (red dotted lines) and APACIC++ (blue dot-dashed lines).

dipole-shower predictions are quite similar and in all cases narrower w.r.t. the SHERPA CKKW predictions. For $p_{T,i}$, the predictions of the unconstrained dipole evolution agree quite well with the respective ones of SHERPA CKKW $n_{\text{ME}} = 1$, again on a 20%–40% level, confirming that the scale setting by the first (the unconstrained) emission reasonably constrains the subsequent one. The p_T hardness of the jets predicted by the inclusive two- and three-jet merging is of course out of reach for the dipole shower. Such higher-order corrections can only be included by matrix-element parton-shower merging techniques or a matching with respective NLO calculations. The top left plot in fig. 13 depicts the vector boson rapidity spectrum obtained under the additional requirement that the first and the second jet appear well separated in rapidity according to $y_1 y_2 < -2$. Except for APACIC++ predicting a strong tendency of the boson to accompany one of the jets, all codes give flat spectra for central rapidities, and, remarkably, the dipole-shower result agrees well with that of SHERPA CKKW $n_{\text{ME}} = 2$. A similar pattern is found in the $|\Delta\eta_{ee,1}| = |\eta_{ee} - \eta_1|$ distribution shown in the top right plot of fig. 13. The dipole-shower curve hardly deviates from the CKKW curves, which reliably describe this observable owing to their higher-order contributions. This tellingly highlights the effects of the improvements of the dipole splitting functions beyond the eikonal approximation. In contrast, APACIC++ describes a suppression for low $|\Delta\eta_{ee,1}|$ values.

In contrast to the shape comparisons above, tab. 2 provides some insight concerning inclusive and exclusive jet rates normalized to the total inclusive cross section. The results given by the unconstrained dipole shower are close to those of SHERPA CKKW $n_{\text{ME}} = 1$. Moreover, it is also found that the default dipole shower predicts much more soft jets compared to APACIC++.

The large phase space available for additional QCD radiation at the LHC will lead to the copious production of jets. Here, this testbed provides an excellent means to study the effects of the \hat{s}_{max} reduction (see sec. 7.3). In tab. 2 and the bottom row of fig. 13 various predictions are

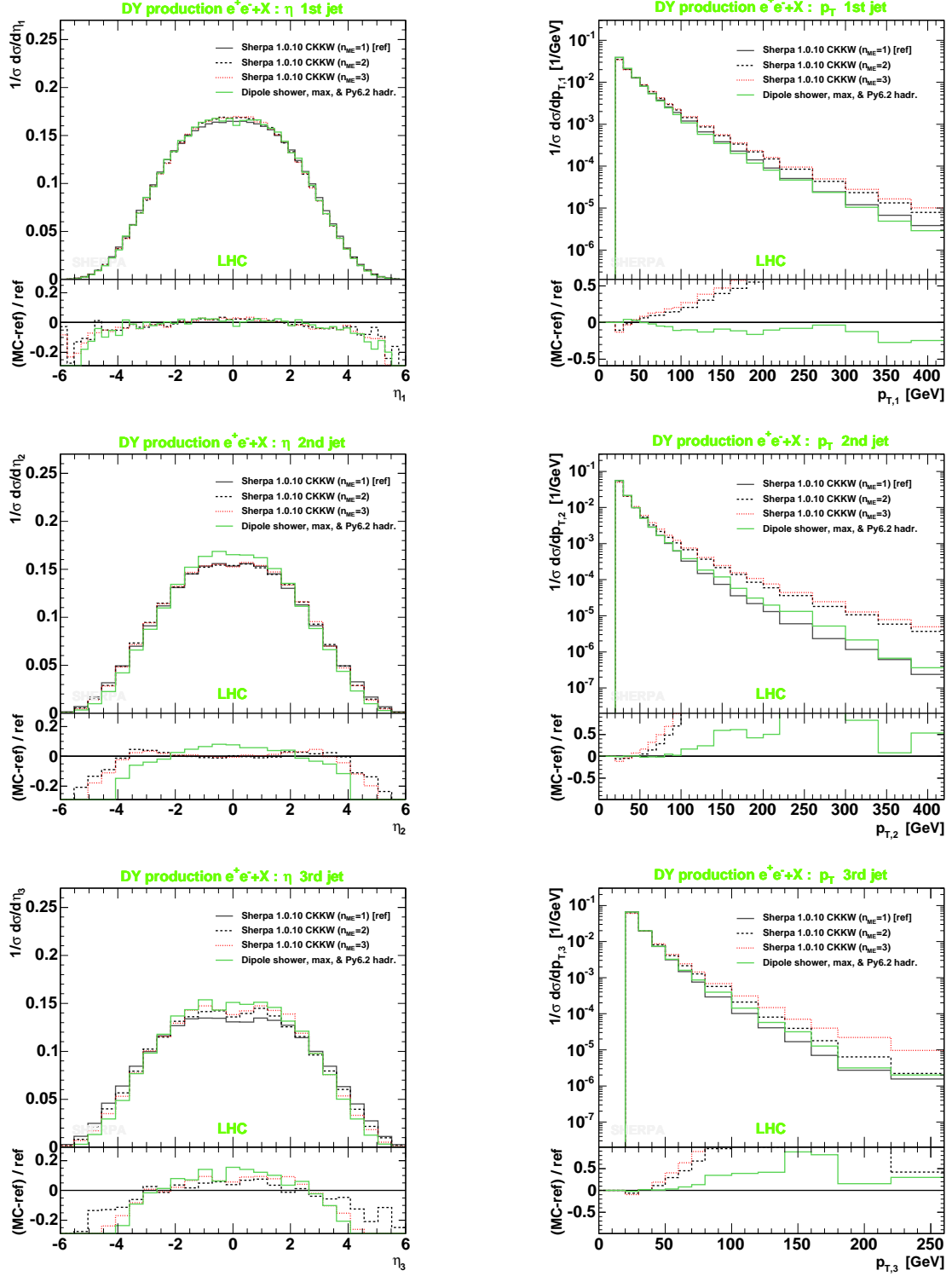


Figure 12: Pseudo-rapidity (left column) and transverse-momentum (right column) distributions of the first three jets in inclusive lepton-pair production simulated for LHC energies. Dipole-shower results are shown in comparison to those obtained by the CKKW method of SHERPA. Labelling is as in fig. 11.

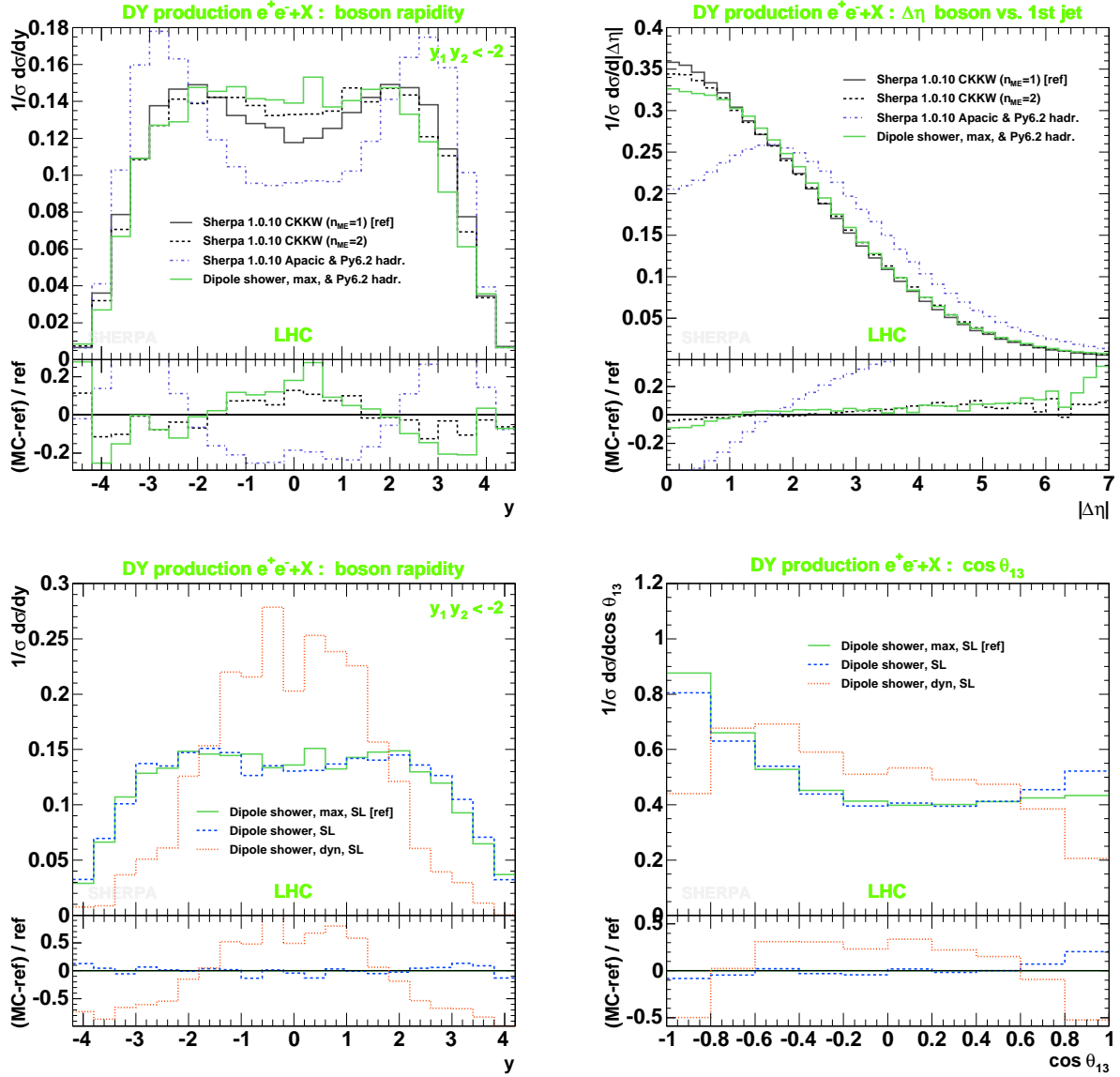


Figure 13: The rapidity of the lepton pair for the first two jets satisfying $y_1 y_2 < -2$ (top left) and the modulus of the pseudo-rapidity difference between the vector boson and the leading jet (top right). Both of which is simulated for inclusive Drell–Yan e^+e^- production at the LHC. The dipole-shower outcome is compared to those received from various SHERPA runs. Labelling is as introduced in fig. 11.

The bottom plots exemplify the impact of the choice of \hat{s}_{max} on the y_{ee} for $y_1 y_2 < -2$ and $\cos \theta_{13}$ distributions as predicted by the unconstrained (solid green curves), the default (dashed blue curves) and the dipole shower where \hat{s}_{max} is set dynamically (dotted red curves). The cosine of the angle between the first and the third jet, $\cos \theta_{13}$, is determined in the rest frame of the first-plus-second jet system.

Monte Carlo	$\frac{\sigma_{\geq 1\text{jet}}}{\sigma_{\text{tot}}}$	$\frac{\sigma_{\geq 2\text{jet}}}{\sigma_{\text{tot}}}$	$\frac{\sigma_{\geq 3\text{jet}}}{\sigma_{\text{tot}}}$	$\frac{\sigma_{=1\text{jet}}}{\sigma_{\text{tot}}}$	$\frac{\sigma_{(y_1 y_2 < -2)}}{\sigma_{\text{tot}}}$
CKKW $n_{\text{ME}} = 1$	0.304	0.082	0.017	0.222	0.016
CKKW $n_{\text{ME}} = 2$	0.340	0.108	0.025	0.231	0.017
CKKW $n_{\text{ME}} = 3$	0.348	0.119	0.034	0.229	0.018
APACIC++	0.232	0.048	0.007	0.157	0.010
Dipole shower, max	0.290	0.084	0.023	0.207	0.012
Dipole shower, max (SL)	0.296	0.087	0.024	0.210	0.013
Dipole shower (SL)	0.267	0.068	0.016	0.199	0.011
Dipole shower, dyn (SL)	0.244	0.052	0.009	0.193	0.0003

Table 2: Cross section ratios as obtained from the various Monte Carlo approaches for inclusive and exclusive (hadron- and shower-level “SL”) jet rates at LHC energies. Jets are defined according to the Run II k_T algorithm [93, 94] and required to have $p_{T,\text{jet}} > 20$ GeV.

confronted with each other, namely those of the unconstrained dipole shower, the default shower where $p_{\perp,\text{ini}}^2 = (1 + \sqrt{2})^2 M_{ee}^2$ and the dipole shower denoted by “dyn” where additionally \hat{s}_{max} is set dynamically according to $p_{\perp,\text{max}}^2 = p_{\perp,\text{ini}}^2 = (1 + \sqrt{2})^2 M_{ee}^2$ (cf. e.g. eqs. (74) and (82) in secs. 5.1.1 and 5.1.2, respectively). The default shower loses hard emissions, such that the ratios of tab. 2 are somewhat smaller w.r.t. those of the unconstrained shower. For the “dyn” variant, the normalized cross sections decrease further, however, dramatically fall if a rapidity separation for the first two jets is required and imposed by $y_1 y_2 < -2$. Furthermore, while the spectra presented at the bottom of fig. 13 show only mild differences between the unconstrained and the default shower, the predictions of the “dyn” shower deviate considerably: the y_{ee} spectrum for $y_1 y_2 < -2$ is far too peaked in the central y region, which also contradicts the performance of the CKKW references shown in the top left corner of the same figure. And, in the $\cos \theta_{13}$ distribution of fig. 13 the third jet is significantly less collinear w.r.t. the first and second jet, where the angle θ_{13} between the first and third jet is taken in the rest frame of the combined first and second jet. Hence, in all examples, the \hat{s}_{max} reduction manifests in a suppression of forward and larger separated emissions (jets), which can be understood, since, firstly, the $p_{\perp,\text{max}}^2$ act as kinematic upper bounds to all start scales $p_{\perp,\text{stt}}^2$, in particular initializing scales $p_{\perp,\text{ini}}^2$. Secondly, for reduced \hat{s}_{max} , the generation of large $|y|$ is suppressed for a single emission, eventually avoiding the production of sets of two-parton invariant masses, $|s_{kg}| = |M| p_{\perp} e^{-y}$ and $|s_{gl}| = |M| p_{\perp} e^{+y}$, where one of them is very small and the other very large. Taken these findings together – also recalling the good agreement with the CKKW results – it is evident that using $\hat{s}_{\text{max}}|_{\Pi} = S$ and $\hat{s}_{\text{max}}|_{\text{FI}} = S$ is a good choice.

8.3 Inclusive jet production at hadron colliders

The copious QCD production of jets is a typical and large phenomenon at hadron colliders, however, from a theoretical point of view, the task of calculating and/or simulating these processes at higher orders in the strong coupling is more complicated and rather involved. Clearly, QCD

jet production severely tests the entire shower algorithm and goes beyond the tasks handled by the dipole shower so far. There are several reasons for this: the primary state is now given as a multi-dipole configuration formed by the $2 \rightarrow 2$ hard QCD processes according to their (large N_C) colour connections, including those that link initial- and final-state partons. Possibly, all dipoles form only one colour singlet or even a “gluonic ring”. Matrix-element corrections for the first extra emission in jet production are absent in the dipole splitting functions; this in turn requires to carefully constrain the initializing scale, such that the shower evolution is guaranteed to proceed in the soft and collinear limits of QCD emission only.

To validate the dipole shower the observables listed below have been considered in more detail.

Dijet azimuthal decorrelations at Tevatron Run II energies

The dijet-decorrelation observable measured in the transverse plane between the two hardest jets, $\Delta\phi_{\text{dijet}} = |\phi_1 - \phi_2|$, provides good insight to the occurrence of additional soft and hard radiation. There is no necessity to reconstruct further jets. The clear full-correlation signature given by $\Delta\phi_{\text{dijet}} = \pi$ washes out in the presence of extra emissions. Since, the strength of the decorrelation rises in dependence on their hardness, the dijet decorrelation can be used to verify any candidate choice of setting the initializing scale.¹⁸

The observable was subject of a recent measurement by DØ at Tevatron Run II with the data taken in different $p_{T,1} = p_{T,\text{max}}$ windows of the leading jet [95]. The details of the analysis are:

- Reconstruct cone jets for $R = 0.7$,
- require $p_{T,2} > 40$ GeV, and,
- require central jet rapidities, $|y_{1,2}| < 0.5$.

Fig. 14 shows the data overlaid with predictions for various choices of the initializing scale: besides the default given in eq. (135), two alternatives have been implemented, namely a geometric mean reading

$$p_{\perp,\text{ini}}^2 \Big|_{\text{Jets}} = 3 \mu_{\text{QCD}}^2 = 3 \frac{2 \hat{s} \hat{t} \hat{u}}{\hat{s}^2 + \hat{t}^2 + \hat{u}^2}, \quad (137)$$

and a more enhanced scale defined as

$$p_{\perp,\text{ini}}^2 \Big|_{\text{Jets}} = (1 + \sqrt{2})^2 \frac{\hat{u} \hat{t}}{\hat{s}}, \quad (138)$$

using the Mandelstam variables of the core process. The scale denoted by “II sc.” is taken according to the latter equation, eq. (138); this one denoted by “QCD sc.” corresponds to eq. (137), and that marked as “low default sc.” follows from dividing eq. (135) by a factor of 3. Obviously, the dipole shower initiated through the low default scale does not account for enough hard emissions and overshoots for soft ones. The other predictions are quite similar, with the “II sc.” and “QCD sc.” variants giving slightly harder and softer results w.r.t. the default case, respectively. The default performs best and will therefore be employed in all what follows. Its predictions still tend to undershoot the data around $\Delta\phi_{\text{dijet}} = 2.8$ in all $p_{T,\text{max}}$ windows of the leading jet, however, keeping in mind that some gluon splitting processes have not been fully taken into account yet, the agreement is satisfactory giving evidence that also other model-intrinsic scales, such as $\tilde{\mu}_F$, μ_F and μ_R , have been chosen reasonably.

¹⁸Showers preferably should predict the distribution for small decreases of $\Delta\phi_{\text{dijet}} = \pi$, the tail may be corrected by the inclusion of matrix elements beyond order α_s^2 .

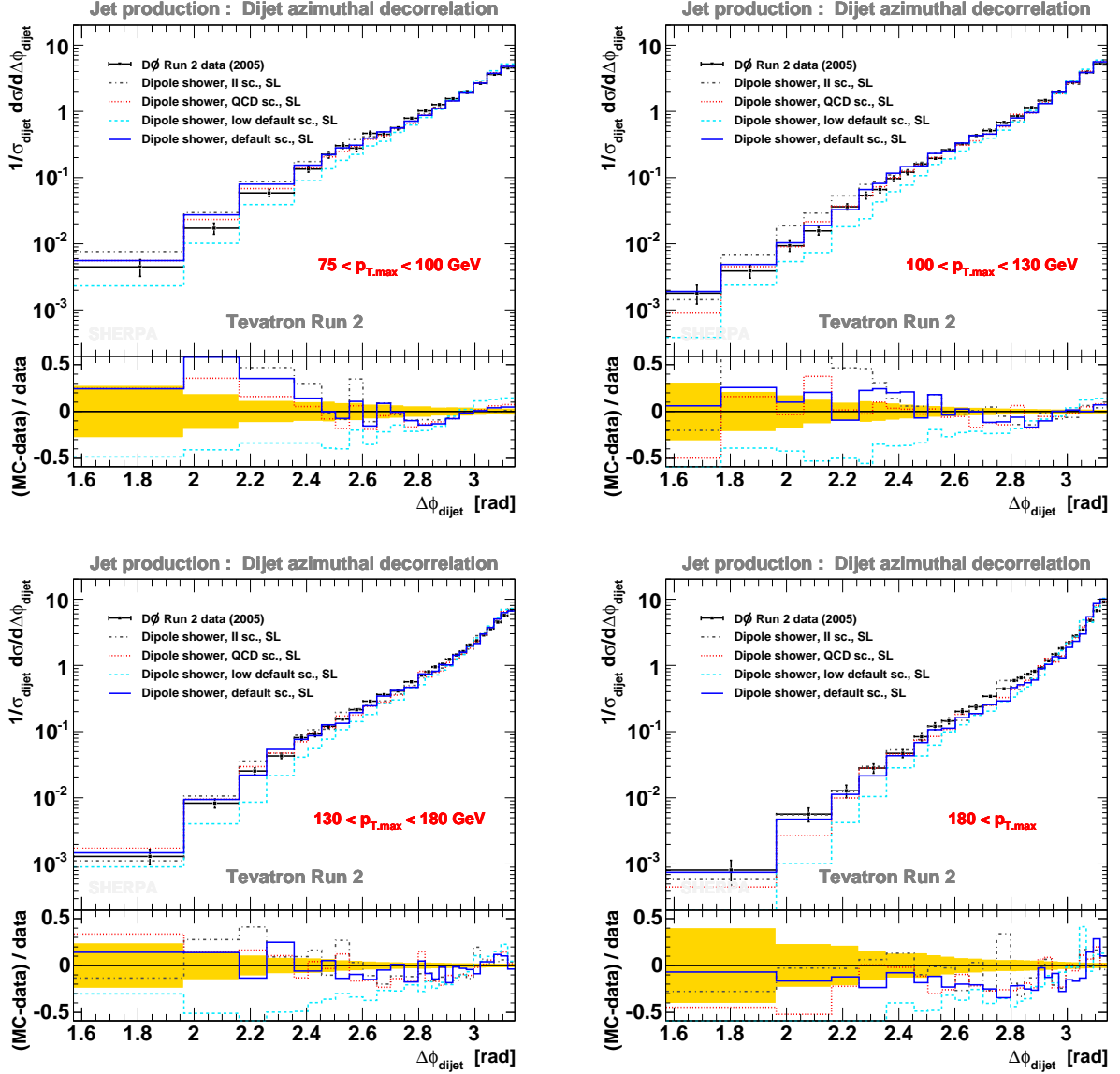


Figure 14: The dijet azimuthal decorrelations in different $p_{T,\text{max}}$ ranges. Dipole-shower results for different choices of the initializing scale are overlaid by data taken by DØ during Tevatron Run II [95].

Dijet mass spectrum at Tevatron Run II energies

With the $p_{\perp,\text{ini}}$ finding in hand, the dipole-shower prediction for the dijet mass spectrum is confronted with data measured during Run I by the DØ collaboration [96]. The analysis requires:

- the reconstruction of jets using a cone algorithm with $R = 0.7$,
- jet transverse energies above 30 GeV, and,
- the dijet candidates to satisfy $|\eta_{1,2}| < 1.0$.

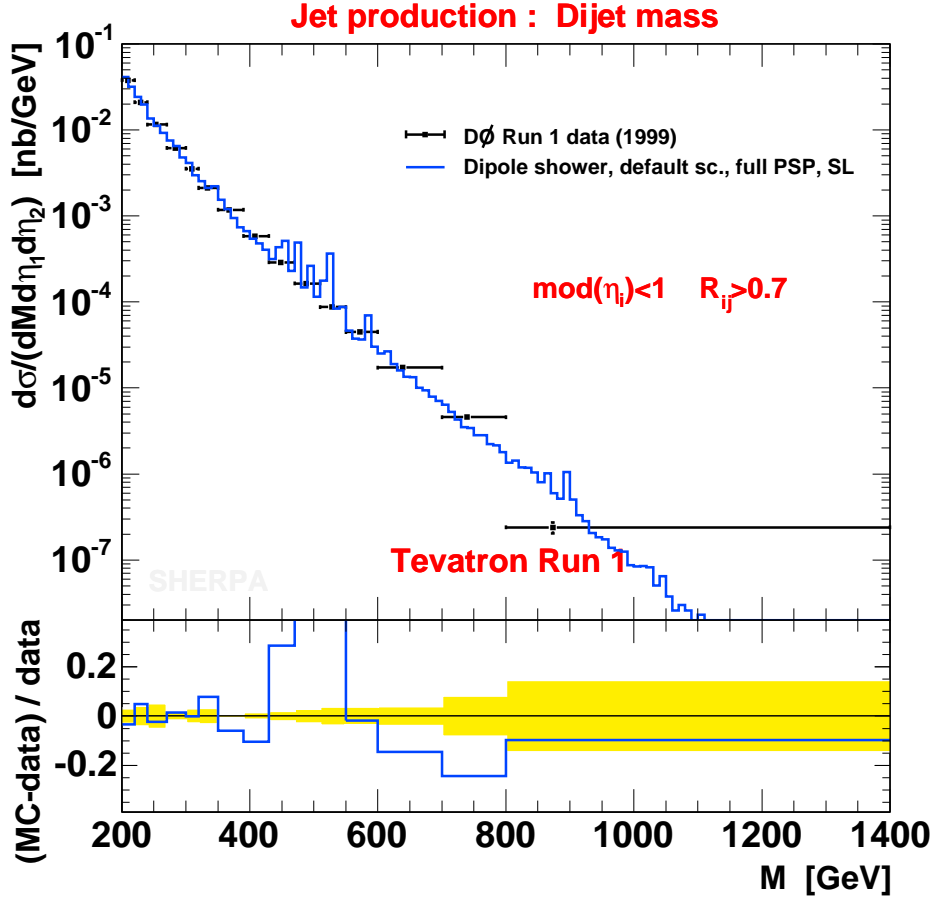


Figure 15: The dijet mass spectrum as measured by DØ during Tevatron Run I [96] compared with the prediction of the dipole shower initialized at scales according to eq. (135) and for no phase-space restriction, i.e. using the default \hat{s}_{max} settings.

As it can be read off fig. 15, the comparison versus data with the dipole-shower results being normalized to the cross section observed in the experiment shows encouraging agreement.

Test of colour coherence at Tevatron Run I energies

An interesting measurement and analysis was carried out by the CDF collaboration during Tevatron Run I, searching for evidence for colour coherence in $p\bar{p}$ collisions at $\sqrt{S} = 1.8$ TeV [97]. Discriminatory observables were found for three-jet events featuring a hard leading jet and a rather soft third jet. They were shown to be sensitive to the correct treatment of QCD colour coherence in parton shower simulations. Here, similarly to the treatment in [36], this CDF analysis is used to test whether the proposed dipole shower is capable of describing the colour-coherence effects seen in the data.¹⁹ The requirements of the CDF study read:

¹⁹Evolving in terms of colour dipoles is said to automatically account for soft colour coherence owing to the eikonal structure of the dipole splitting cross sections, however, the colour factor ambiguities for quark-gluon dipoles (discussed in sec. 4.2 ff) require more serious investigation in this direction. The comparison with the CDF data is just a first step.

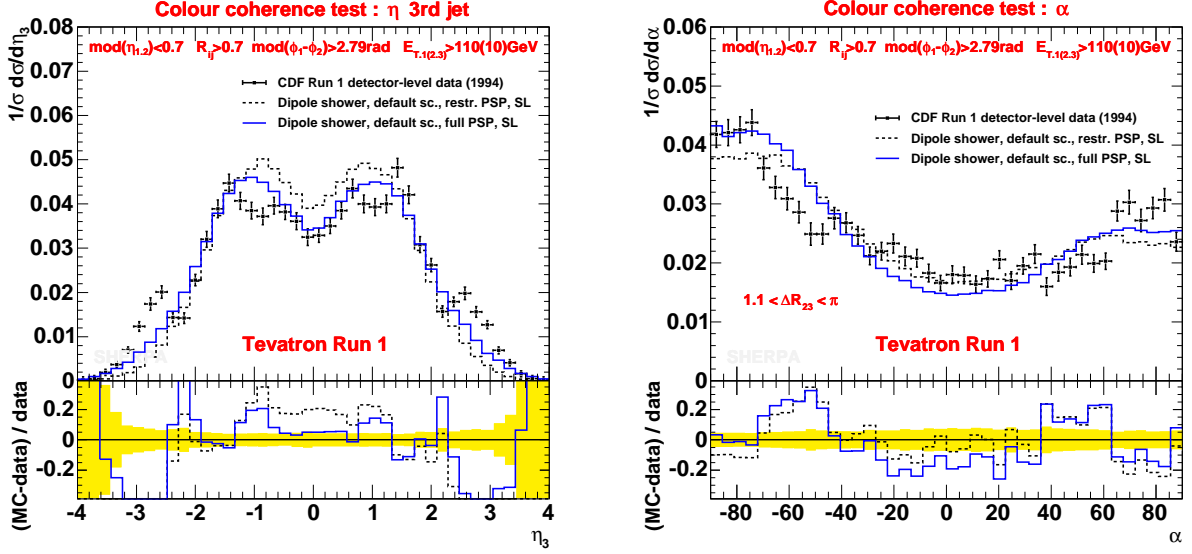


Figure 16: Colour-coherence tests in inclusive three-jet production at Tevatron Run I energies according to a CDF study presented in [97]: (left panel) pseudo-rapidity distribution of the third jet and (right panel) the angle α (defined in the text). Experimental errors are statistical only and the histograms are normalized to their respective binwidth. For the latter three observables, dipole-shower (shower-level) predictions under full (blue solid lines) and restricted (black dashed lines) emission phase space are shown in comparison with the (detector-level) data of the CDF measurement [97].

- Jets are defined through a cone algorithm, using $R = 0.7$,
- the two leading jets are constrained to $|\eta_{1,2}| < 0.7$,
- they have to be oriented back-to-back within 20 degrees, i.e. $|\phi_1 - \phi_2| > 2.79$,
- jet E_T thresholds have to be respected for the first jet and all next-to-first jets of 110 GeV and 10 GeV, respectively, and,
- for the α angle only, a cut on $\Delta R_{23} = \sqrt{(\eta_2 - \eta_3)^2 + (\phi_2 - \phi_3)^2}$ has to be imposed, namely $1.1 < \Delta R_{23} < \pi$.
- The angle α is defined through

$$\tan \alpha = \frac{\text{sign}(\eta_2)(\eta_3 - \eta_2)}{|\phi_3 - \phi_2|}. \quad (139)$$

In fig. 16 the comparison between detector-level data and dipole-shower predictions obtained at the shower level is shown for the η_3 and angle α distributions. As pointed out in [97], these two observables receive small detector corrections only, which is not the case for the ΔR_{23} separation of the second and third hardest jet in (η, ϕ) space. The latter is known to be strongly affected by detector effects, therefore, not considered here.²⁰ If colour-coherence effects are modelled correctly, η_3 should arise broader and feature a significant dip for central values. The α spectrum

²⁰For the same reason, in the study of [36] ΔR_{23} has not been taken into account either.

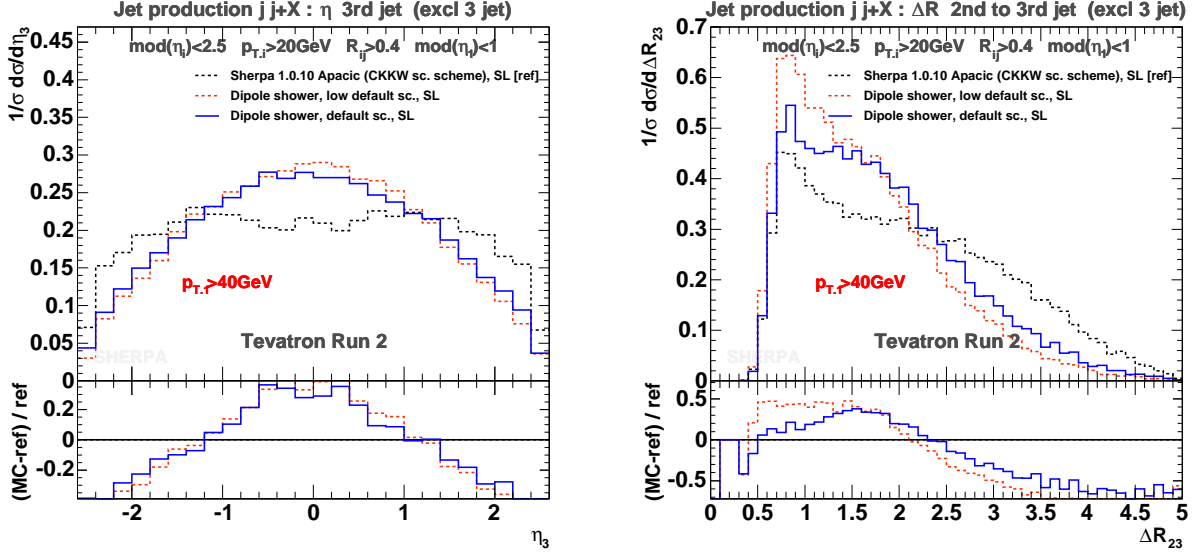


Figure 17: Pseudo-rapidity distribution of the third jet and spatial separation between the second and third jet in exclusive three-jet final states simulated for Tevatron Run II energies. The plots are obtained requiring a larger jet p_T threshold for the hardest jet to pass. The SHERPA shower prediction generated by APACIC++ in CKKW scale-scheme mode (black dashed curves) is compared to the dipole-shower predictions, namely for default (blue solid curves) and lowered initializing scales (red dashed curves).

should be minimal for small $|\alpha|$ followed by a clear rise towards larger positive angles. As can be seen in fig. 16, the dipole shower predicts these characteristics, providing fairly good evidence that colour-coherence effects are reasonably modelled. The agreement with data deteriorates once the prediction is taken from a dipole shower where the \hat{s}_{\max} setting has been (considerably) reduced. This again emphasizes that the natural choice is to assign the full phase space to single emissions by using the default \hat{s}_{\max} settings.

Exclusive three-jet final-state challenge

Recent CDF measurements have found an excess in data of exclusive three-jet events with small ΔR_{23} , which is not described by available tools, such as PYTHIA (Tune A) [98, 99]. In a first qualitative study the potential of the new dipole shower to predict ΔR_{23} differently w.r.t. traditional leading-log showers is estimated. Therefore, the following analysis has been applied:

- Require jet reconstruction according to the cone jet algorithm, use $R = 0.4$,
- use general cuts on jets of $p_{T,i} > 20$ GeV and $|\eta_i| < 2.5$,
- additionally, use $|\eta_1| < 1.0$ for the hardest jet, and,
- consider the trigger-jet effect, i.e. demand $p_{T,1} > 40$ GeV.

The results are presented in fig. 17 and show the pseudo-rapidity spectrum of the third jet together with the ΔR_{23} distribution mentioned before. Concerning the former, the dipole-shower variants are found to generate steeper spectra, while inspecting the latter, the shower starting

from the lower initializing scale prefers populating the region of small jet separations the most. The APACIC++ prediction rises towards smaller separations as well but stays below the dipole shower curves and features a broader tail. Additionally, by relaxing the $p_{T,1} > 40$ requirement, treating all jets likewise, the higher $p_{T,1}$ threshold was identified as a major source in projecting out the peak for low ΔR_{23} . The different behaviour of the dipole and parton shower eventually can be seen as a consequence of generating the full radiation pattern differently. For example, recalling that the p_{\perp}^2 definition includes a product of two-parton squared masses $s_{12}s_{23}$, a small s_{12} with a potentially small angle between parton 1 and 2 can still be compensated by a large s_{23} giving the same p_{\perp}^2 . In a $1 \rightarrow 2$ splitting usually there is no such freedom of compensating a small s_{12} , it might be rather cut away by the parton-shower cut-off. In conclusion, the tendency of the dipole shower to enhance the production of spatially less separated jets should be studied in more detail and more realistically including underlying event simulation etc. and, possibly, a direct comparison to data.

9 Conclusions

In this publication, the colour-dipole shower approach based on the Lund Colour Dipole Model [8, 16] has been extended. In this model, the description of sequences of QCD emissions is formulated in an expansion around their soft limit. In the context of hadronic collisions, a novel, perturbative description of initial-state showering based on the emission properties of colour dipoles has been developed, which is in clear contrast to the corresponding Lund ansatz. In summary, initial-state radiation is treated directly and not redefined by final-state radiation arising from final-state dipoles that contain extended colour sources, which, therefore, are subject of a semi-classically motivated suppression of high p_{\perp} emissions. In contrast, in the new model the hadron remnants are completely kept outside the evolution. The fully perturbative treatment led to the introduction of new dipole types, which contain incoming partons.

The description of gluon emissions off colour dipoles has been generalized to account for all kinematic regions appearing in hadronic collisions. It centers around a Lorentz invariant generalization of the definition of the dipole evolution variables. Splitting functions have been derived for the new dipole types. Together with the well-known radiation pattern of pure final-state colour dipoles, their utilization in a complete shower algorithm has been presented to describe soft and collinear multiple parton emission. The feasibility of the approach has been shown through its successful application to electron-positron annihilation into hadrons, inclusive Drell-Yan pair production and inclusive QCD jet production at hadron colliders. All comparisons deliver encouraging results in good agreement with other models and with experimental data. It is worth to mention that the feature of generating broader pseudo-rapidity spectra – often mentioned in connection with colour-dipole evolution according to ARIADNE – has not been confirmed by the new model. Moreover, for the first time, results have been presented for the inclusive production of jets in hadronic collisions that have been obtained from a shower based on the colour-dipole approach. First evidences could be given that the model correctly accounts for colour-coherence effects.

Taken together, an appealing picture of dipole cascading has been achieved. Future work will concern the full incorporation of gluon splittings in the initial and final state, and, the generalization to finite quark masses. In addition, a merging with multi-leg tree-level matrix elements for additional QCD radiation will be addressed, and, a matching with full NLO QCD calculations shall be studied.

Acknowledgements

The authors would like to thank Mike Seymour and Steffen Schumann for fruitful discussions, and are also thankful to the other members of the SHERPA team for supporting this work.

J. W. thanks the CERN theory division for great hospitality during his Marie Curie fellowship period, where parts of this work have been accomplished. Furthermore, J. W. acknowledges financial support by the Marie Curie Fellowship program for Early Stage Research Training.

The authors also acknowledge financial support by MCnet (contract number MRTN-CT-2006-035606) and by BMBF.

References

- [1] T. Sjöstrand *Comput. Phys. Commun.* **82** (1994) 74–90.
- [2] T. Sjöstrand *et. al. Comput. Phys. Commun.* **135** (2001) 238–259 [[hep-ph/0010017](#)].
- [3] T. Sjöstrand, L. Lönnblad and S. Mrenna [hep-ph/0108264](#).
- [4] T. Sjöstrand, L. Lönnblad, S. Mrenna and P. Skands [hep-ph/0308153](#).
- [5] T. Sjöstrand, S. Mrenna and P. Skands *JHEP* **05** (2006) 026 [[hep-ph/0603175](#)].
- [6] G. Corcella *et. al. JHEP* **01** (2001) 010.
- [7] G. Corcella *et. al.* [hep-ph/0210213](#).
- [8] L. Lönnblad *Comput. Phys. Commun.* **71** (1992) 15–31.
- [9] T. Sjöstrand *Phys. Lett.* **B157** (1985) 321.
- [10] M. Bengtsson, T. Sjöstrand and M. van Zijl *Z. Phys.* **C32** (1986) 67.
- [11] H.-U. Bengtsson and T. Sjöstrand *Comput. Phys. Commun.* **46** (1987) 43.
- [12] G. Marchesini and B. R. Webber *Nucl. Phys.* **B310** (1988) 461.
- [13] T. Gleisberg, S. Höche, F. Krauss, A. Schälicke, S. Schumann and J. Winter *JHEP* **0402** (2004) 056 [[hep-ph/0311263](#)].
- [14] F. Krauss, A. Schälicke and G. Soff *Comput. Phys. Commun.* **174** (2006) 876–902 [[hep-ph/0503087](#)].
- [15] G. Gustafson *Phys. Lett.* **B175** (1986) 453.
- [16] G. Gustafson and U. Pettersson *Nucl. Phys.* **B306** (1988) 746.
- [17] B. Andersson, G. Gustafson and L. Lönnblad *Nucl. Phys.* **B339** (1990) 393–406.
- [18] R. K. Ellis, W. J. Stirling and B. R. Webber *Camb. Monogr. Part. Phys. Nucl. Phys. Cosmol.* **8** (1996) 1–435.

- [19] M. Weierstall, “Anpassung und Test von Fragmentierungsmodellen mit präzisen Ereignisform- und Einteilchenverteilungen unter besonderer Berücksichtigung von identifizierten Teilchenspektren.” PhD thesis, Fachbereich Physik, Bergische Universität Wuppertal, 1995.
- [20] M. Siebel, J. Drees, K. Hamacher and F. Mandl *Nucl. Phys. Proc. Suppl.* **152** (2006) 7–10.
- [21] **OPAL** Collaboration, M. Z. Akrawy *et. al.* *Z. Phys.* **C47** (1990) 505–522.
- [22] **DELPHI** Collaboration, P. Abreu *et. al.* *Z. Phys.* **C73** (1996) 11–60.
- [23] I. G. Knowles *et. al.* [hep-ph/9601212](#).
- [24] B. Andersson, G. Gustafson, L. Lönnblad and U. Pettersson *Z. Phys.* **C43** (1989) 625.
- [25] N. Magnussen *et. al.* In *Hamburg 1991, Proceedings, Physics at HERA, vol. 3* 1167–1219. (see HIGH ENERGY PHYSICS INDEX 30 (1992) No. 12988).
- [26] A. Banfi, G. Corcella and M. Dasgupta *JHEP* **03** (2007) 050 [[hep-ph/0612282](#)].
- [27] S. Gieseke, A. Ribon, M. H. Seymour, P. Stephens and B. Webber *JHEP* **02** (2004) 005 [[hep-ph/0311208](#)].
- [28] S. Gieseke *et. al.* [hep-ph/0609306](#).
- [29] L. Lönnblad. Prepared for 14th International Workshop on Deep Inelastic Scattering (DIS 2006), Tsukuba, Japan, 20–24 Apr 2006.
- [30] T. Sjöstrand, S. Mrenna and P. Skands [arXiv:0710.3820](#) [[hep-ph](#)].
- [31] T. Sjöstrand and P. Z. Skands *Eur. Phys. J.* **C39** (2005) 129–154 [[hep-ph/0408302](#)].
- [32] S. Gieseke, P. Stephens and B. Webber *JHEP* **12** (2003) 045 [[hep-ph/0310083](#)].
- [33] Z. Nagy and D. E. Soper *JHEP* **10** (2005) 024 [[hep-ph/0503053](#)].
- [34] Z. Nagy and D. E. Soper [hep-ph/0601021](#).
- [35] M. Dinsdale, M. Ternick and S. Weinzierl *Phys. Rev.* **D76** (2007) 094003 [[arXiv:0709.1026](#) [[hep-ph](#)]].
- [36] S. Schumann and F. Krauss [arXiv:0709.1027](#) [[hep-ph](#)].
- [37] W. T. Giele, D. A. Kosower and P. Z. Skands [arXiv:0707.3652](#) [[hep-ph](#)].
- [38] S. Catani and M. H. Seymour *Nucl. Phys.* **B485** (1997) 291–419 [[hep-ph/9605323](#)].
- [39] S. Catani, S. Dittmaier, M. H. Seymour and Z. Trocsanyi *Nucl. Phys.* **B627** (2002) 189–265 [[hep-ph/0201036](#)].
- [40] D. A. Kosower *Phys. Rev.* **D57** (1998) 5410–5416 [[hep-ph/9710213](#)].
- [41] A. Gehrmann-De Ridder, T. Gehrmann and E. W. N. Glover *JHEP* **09** (2005) 056 [[hep-ph/0505111](#)].
- [42] S. Frixione and B. R. Webber *JHEP* **06** (2002) 029 [[hep-ph/0204244](#)].

- [43] S. Frixione, P. Nason and B. R. Webber *JHEP* **08** (2003) 007 [[hep-ph/0305252](#)].
- [44] P. Nason. Prepared for 14th International Workshop on Deep Inelastic Scattering (DIS 2006), Tsukuba, Japan, 20-24 Apr 2006.
- [45] S. Frixione, P. Nason and C. Oleari *JHEP* **11** (2007) 070 [[arXiv:0709.2092](#) [[hep-ph](#)]].
- [46] S. Frixione and B. R. Webber [hep-ph/0612272](#).
- [47] S. Frixione, Z. Kunszt and A. Signer *Nucl. Phys.* **B467** (1996) 399–442 [[hep-ph/9512328](#)].
- [48] S. Catani, F. Krauss, R. Kuhn and B. R. Webber *JHEP* **0111** (2001) 063–084 [[hep-ph/0109231](#)].
- [49] F. Krauss *JHEP* **0208** (2002) 015–031 [[hep-ph/0205283](#)].
- [50] L. Lönnblad *JHEP* **05** (2002) 046.
- [51] M. L. Mangano, M. Moretti and R. Pittau *Nucl. Phys.* **B632** (2002) 343–362 [[hep-ph/0108069](#)].
- [52] M. L. Mangano, M. Moretti, F. Piccinini and M. Treccani *JHEP* **01** (2007) 013 [[hep-ph/0611129](#)].
- [53] F. Krauss, A. Schälicke, S. Schumann and G. Soff *Phys. Rev.* **D70** (2004) 114009 [[hep-ph/0409106](#)].
- [54] A. Schälicke and F. Krauss *JHEP* **07** (2005) 018 [[hep-ph/0503281](#)].
- [55] N. Lavesson and L. Lönnblad *JHEP* **07** (2005) 054 [[hep-ph/0503293](#)].
- [56] S. Mrenna and P. Richardson *JHEP* **05** (2004) 040 [[hep-ph/0312274](#)].
- [57] M. L. Mangano, M. Moretti, F. Piccinini, R. Pittau and A. D. Polosa *JHEP* **07** (2003) 001 [[hep-ph/0206293](#)].
- [58] T. Stelzer and W. F. Long *Comput. Phys. Commun.* **81** (1994) 357–371 [[hep-ph/9401258](#)].
- [59] F. Maltoni and T. Stelzer *JHEP* **02** (2003) 027 [[hep-ph/0208156](#)].
- [60] J. Alwall *et. al.* [arXiv:0706.2334](#) [[hep-ph](#)].
- [61] A. Kanaki and C. G. Papadopoulos *Comput. Phys. Commun.* **132** (2000) 306–315 [[hep-ph/0002082](#)].
- [62] C. G. Papadopoulos and M. Worek *Eur. Phys. J.* **C50** (2007) 843–856 [[hep-ph/0512150](#)].
- [63] J. Alwall *et. al.* [arXiv:0706.2569](#) [[hep-ph](#)].
- [64] E. Fermi *Z. Phys.* **29** (1924) 315–327.
- [65] C. F. von Weizsacker *Z. Phys.* **88** (1934) 612–625.
- [66] E. J. Williams *Phys. Rev.* **45** (1934) 729–730.
- [67] B. Andersson *Camb. Monogr. Part. Phys. Nucl. Phys. Cosmol.* **7** (1997) 1–471.

- [68] J. M. Campbell, M. A. Cullen and E. W. N. Glover *Eur. Phys. J.* **C9** (1999) 245–265 [[hep-ph/9809429](#)].
- [69] B. Andersson and L. Lönnblad. DESY-92-098.
- [70] L. Lönnblad *Z. Phys.* **C65** (1995) 285–292.
- [71] L. Lönnblad *Nucl. Phys.* **B458** (1996) 215–230 [[hep-ph/9508261](#)].
- [72] U. Pettersson. LU-TP-88-5.
- [73] A. Daleo, T. Gehrmann and D. Maitre *JHEP* **04** (2007) 016 [[hep-ph/0612257](#)].
- [74] R. Kleiss *Phys. Lett.* **B180** (1986) 400.
- [75] M. H. Seymour *Nucl. Phys.* **B436** (1995) 443–460 [[hep-ph/9410244](#)].
- [76] R. D. Field. Redwood City, USA: Addison-Wesley (1989) 366 p. (Frontiers in physics, 77).
- [77] D. Amati, A. Bassetto, M. Ciafaloni, G. Marchesini and G. Veneziano *Nucl. Phys.* **B173** (1980) 429.
- [78] G. Curci, W. Furmanski and R. Petronzio *Nucl. Phys.* **B175** (1980) 27.
- [79] J. Pumplin *et. al.* *JHEP* **07** (2002) 012 [[hep-ph/0201195](#)].
- [80] H. Hoeth, “Messung der Vierjet-Winkelverteilungen und Bestimmung der QCD Farbfaktoren mit Hilfe des APACIC++ Generators.” Diploma thesis, Fachbereich Physik, Bergische Universität Wuppertal, 2003.
- [81] K. Hamacher and M. Weierstall [hep-ex/9511011](#).
- [82] A. Buckley [arXiv:0708.2655](#) [[hep-ph](#)].
- [83] S. Catani, Y. L. Dokshitzer, M. Olsson, G. Turnock and B. R. Webber *Phys. Lett.* **B 269** (1991) 432.
- [84] G. Dissertori *et. al.* [arXiv:0712.0327](#) [[hep-ph](#)].
- [85] A. Gehrmann-De Ridder, T. Gehrmann, E. W. N. Glover and G. Heinrich [arXiv:0711.4711](#) [[hep-ph](#)].
- [86] **CDF** Collaboration, A. A. Affolder *et. al.* *Phys. Rev. Lett.* **84** (2000) 845–850 [[hep-ex/0001021](#)].
- [87] **D0** Collaboration, V. M. Abazov *et. al.* *Phys. Rev.* **D76** (2007) 012003 [[hep-ex/0702025](#)].
- [88] C. Anastasiou, L. J. Dixon, K. Melnikov and F. Petriello *Phys. Rev.* **D69** (2004) 094008 [[hep-ph/0312266](#)].
- [89] F. Krauss, A. Schälicke, S. Schumann and G. Soff *Phys. Rev.* **D72** (2005) 054017 [[hep-ph/0503280](#)].
- [90] T. Gleisberg, F. Krauss, A. Schälicke, S. Schumann and J. Winter *Phys. Rev.* **D72** (2005) 034028 [[hep-ph/0504032](#)].
- [91] **D0** Collaboration, H. Nilsen **D0 note 5066-CONF**.

- [92] R. Kuhn, F. Krauss, B. Ivanyi and G. Soff *Comput. Phys. Commun.* **134** (2001) 223–266 [hep-ph/0004270].
- [93] S. Catani, Y. L. Dokshitzer and B. R. Webber *Nucl. Phys.* **B 406** (1993) 187.
- [94] G. C. Blazey *et. al.* hep-ex/0005012.
- [95] **D0** Collaboration, V. M. Abazov *et. al. Phys. Rev. Lett.* **94** (2005) 221801 [hep-ex/0409040].
- [96] **D0** Collaboration, B. Abbott *et. al. Phys. Rev. Lett.* **82** (1999) 2457–2462 [hep-ex/9807014].
- [97] **CDF** Collaboration, F. Abe *et. al. Phys. Rev.* **D50** (1994) 5562–5579.
- [98] R. D. Field and B. Knuteson. Private communication, 2007.
- [99] **CDF** Collaboration, G. Choudalakis arXiv:0710.2372 [hep-ex].